

A Precise Measurement of  
the Stark Shift in the Indium  
 $5P_{1/2} \rightarrow 6S_{1/2}$  410 nm Transition

by  
Nathan A. Schine

Professor Protik K. Majumder, Advisor

A thesis submitted in partial fulfillment  
of the requirements for the  
Degree of Bachelor of Arts with Honors  
in Physics

WILLIAMS COLLEGE  
Williamstown, Massachusetts  
May 20, 2013



## Abstract

We have completed a measurement of the Stark shift within the 410 nm  $5P_{1/2} \rightarrow 6S_{1/2}$  E1 transition in  $^{115}\text{In}$ . Our final measurement of the Stark shift constant,  $k_S = -122.92(33) \frac{\text{kHz}}{(\text{kV}/\text{cm})^2}$ , has a statistical uncertainty of 0.04% and total uncertainty of 0.27%. This provides a value for the polarizability difference,  $\Delta\alpha_0$ , between the two states of  $1000.2 \pm 2.7 \text{ a}_0^2$ . This result is in excellent agreement with a recent theoretical *ab initio* calculation and is a factor of 29 more precise than previous measurements. This measurement also results in a model dependent determination of the lifetimes of the  $6P_{1/2;3/2}$  states. We find  $\tau_{6P_{1/2}} = 63.77(50) \text{ ns}$ , and  $\tau_{6P_{3/2}} = 58.17(45) \text{ ns}$ . These results are also in excellent agreement with another theoretical calculation and are an order of magnitude more precise than previous measurements. The Stark shift measurement was performed using FM spectroscopy on laser light produced by a GaN diode laser that interacted transversely with an indium atomic beam of optical depth  $\sim 10^{-3}$ . Fabry-Pérot interferometry and saturated absorption spectroscopy provided frequency linearization and calibration, respectively. Four separate fitting programs were used to confirm the Stark shift extraction from the approximately 6000 individual measurements, and many sources of systematic error were explored and quantified.



## Acknowledgments

First of all, I would like to thank my advisor, Professor Tiku Majumder, for his warm and insightful guidance over these last two years. I am incredibly grateful for the time, attention, and advice he has given me. I would also like to thank Dr. Gambhir Ranjit for the great help he provided throughout this experiment. I also greatly appreciate the strong foundation built by previous thesis students Anders Schneider and Antonio Lorenzo, as well as the presence and camaraderie of David Kealhofer in the lab.

I would like to thank Michael Taylor for his support and expertise in the many machining projects undertaken for this work along with Larry George for his work and aid in addressing electronics challenges. I also wish to thank Professor Jones for his comments and suggestions on my written work.

I wish to thank the professors and students of the physics department for the wonderful community of support in the physics major. Also, my thanks go out to my non-physics friends, through the Williams College Jewish Association and otherwise. More than anything, these personal interactions have defined my experience at Williams.

I thank my wonderful fiancée, Rachel Hagler, for her constant love, understanding, and support through the long hours of work necessary to complete this thesis. Finally, I thank my family for their love, their encouragement, and for enabling me to come to Williams.



# Executive Summary

This thesis describes the completion of a new, high-precision measurement of the Stark shift in the  $5P_{1/2} \rightarrow 6S_{1/2}$  transition in indium. This results in new values for the polarizability difference between these two states as well as the lifetimes of the two  $6P$  states in indium. All three of these results are one to two orders of magnitude more precise than previous measurements, and they agree excellently with recent *ab initio* atomic theory calculations of these quantities.

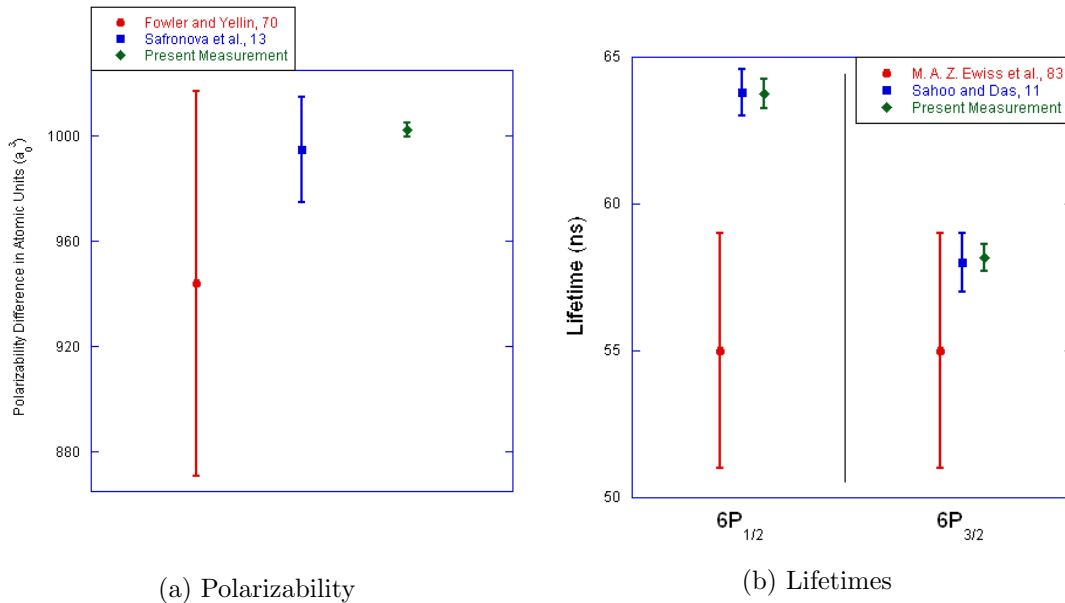


Figure 1: A comparison of results for the polarizability and lifetimes determined in the present work. In each plot, our experimental results are at the right, the most recent theory is in the middle, and the previous experiment is on the left.

In the Majumder lab, we perform high-precision measurements of atomic observables in trivalent atomic systems (Group IIIA). These measurements are stringent tests of the state-of-the-art atomic theory of the valence  $P$  electron in these systems. This atomic theory has relevance in certain experiments that test the Standard Model and that search for physics beyond the Standard Model. In particular, improving the precision of the atomic theory results in more precise determinations of various constants of fundamental physics, e.g.  $\sin \theta_w$ . By confirming to high precision

the accuracy of a new generation of *ab initio* wavefunction calculations, approaching an order of magnitude more precise than previous attempts, experimental determinations in atomic systems of constants of relevance in fundamental physics have been made correspondingly more precise. We have worked closely with an atomic theory group run by Marianna Safronova at the University of Delaware to determine which measurements of atomic observables would be most useful in pushing atomic theory further. In parallel with the completion of our present experiment, Safronova, *et al.* published the most precise theory of the atomic polarizability of indium to date, in agreement with our measurement. This close interplay between theory and experiment has paid off in establishing the relevance, context, and theoretical confirmation of our work.

The Stark shift is the change in the frequency of an atomic transition due to the presence of an electric field. Second order perturbation theory tells us that a static electric field causes a quadratic shift to the energy levels of an atom, generally causing a greater shift in higher energy states. We measure this shift by repeatedly scanning a laser across the atomic transition while alternating between a strong electric field and no electric field in the interaction region; the electric field is created by a polished stainless steel high voltage plate 1 cm separated from a ground plate. To reduce the Doppler width of the absorption profile, we perform this spectroscopy in a collimated indium atomic beam. This beam is produced in a home-built oven that heats  $\sim 100$  grams of indium pellets to  $900^\circ\text{C}$  in a molybdenum crucible. Both the source and the interaction regions are contained in a vacuum system that maintains pressures below  $10^{-6}$  Torr. Because of the low optical depths associated with the atomic beam, we utilize frequency modulation spectroscopy, which provides a high quality, zero background signal. For experimental reasons discussed in detail in Chapter 5, we implement the FM spectroscopy in the unusual high modulation depth limit. In standard FM spectroscopy, one demodulates at the modulation frequency; however, in addition to this, we also utilized demodulation at twice the modulation frequency. The former has been explored in the high modulation depth limit, but very little has been published in this limit with demodulation at twice the modulation frequency, so we derive the relevant line shapes herein. Major projects the author led or contributed to during the completion of this experiment include building the source oven, repair, extension, and operation of the vacuum system, rebuilding the high voltage system, stabilizing a Littrow-configured diode laser and implementing the optical setup, performing theoretical derivations of line shapes and polarizabilities, and completing numerous computer programming projects using LABVIEW, Mathematica, and Matlab as described below.

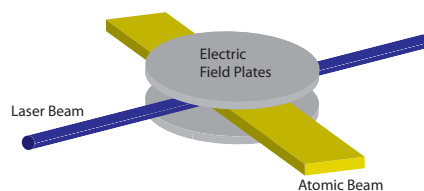


Figure 2: The geometry of the interaction region. The direction of propagation of the laser, the direction of the atoms' motion, and the direction of the electric field are all mutually orthogonal.

A LABVIEW program directs laser scans, high voltage alternation, and data recording. During each laser scan, we record three signals simultaneously: the FM signal for the Stark shift measurement, a Fabry-Pérot transmission signal for frequency linearization, and a saturated absorption signal for a frequency reference. We took data from a total of 12,000 usable 2 s individual scans in a variety of experimental configurations. Several independent Matlab programs fit these data to appropriate approximate and analytic forms and then performed the necessary manipulations to extract 6,000 Stark shift measurements. This large set of data, represented in Fig. 3, results in a mean value for the Stark shift constant of  $k_S = -122.92 \frac{\text{kHz}}{(\text{kV/cm})^2}$  with a very low, 0.04% statistical uncertainty.

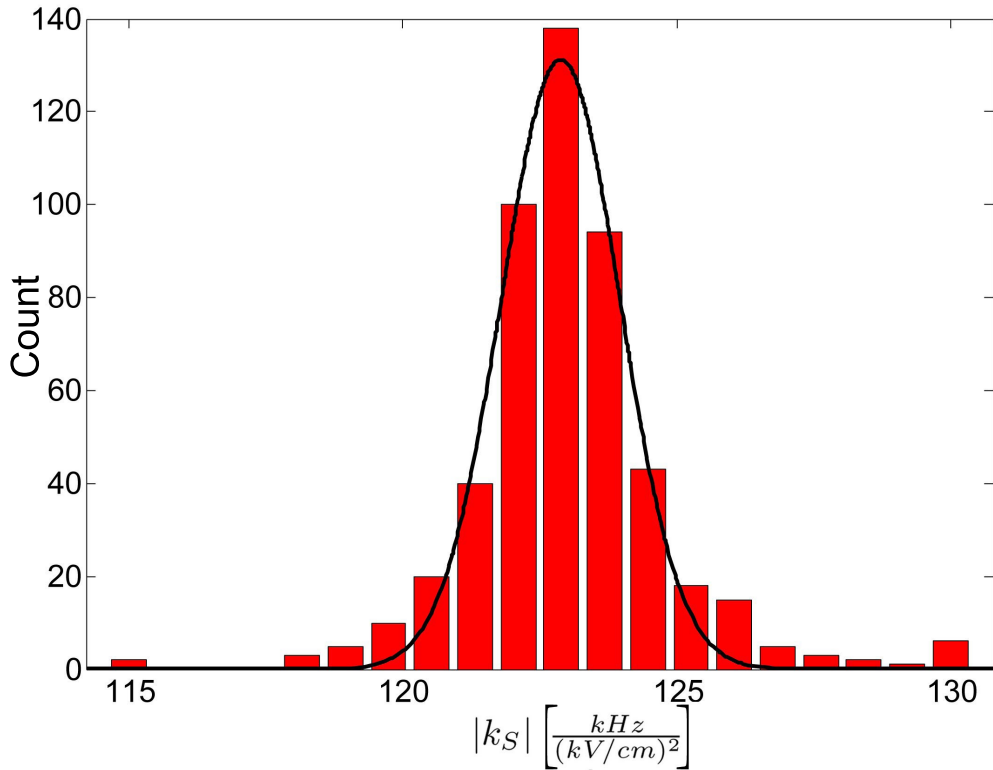


Figure 3: A histogram of all data collected. Each point herein represents the average of 25 individual measurements of the Stark shift constant.

In precision measurements, the statistical uncertainty rarely accounts for the actual experimental precision. The great variety of experimental conditions under which data was taken allows for the exploration of many potential sources of systematic error. We explored twelve experimental parameters as potential sources for systematic error, looking for a dependence of the measured Stark shift on these variables. We searched for potential correlations within the data, and ran more sophisticated statistical analyses as well. We found two small dependences as well as excessive,

non-statistical scatter in a third. Surprisingly, these small systematic uncertainties were similar in magnitude or smaller than the uncertainty arising from the high voltage plate separation precision at the 0.1% level. Combining all sources of error, we arrived at a final 0.27% uncertainty, providing our final value for the polarizability difference between the  $6S_{1/2}$  and  $5P_{1/2}$  states in indium of  $\Delta\alpha_0 = 1000.2(2.7)$  a.u.

State-of-the-art atomic theory further demonstrates that the two  $6S - 6P$  matrix elements greatly dominate *both* sums. Using our high precision measurement of the polarizability difference and the best theoretical values for the remainder of the infinite sums, we arrive at a model dependent measurement of the  $6S - 6P$  matrix elements. These in turn provide the lifetimes of the  $6P_{1/2}$  and  $6P_{3/2}$  states in indium:  $\tau_{6P_{1/2}} = 63.77(50)$  ns and  $\tau_{6P_{3/2}} = 58.17(45)$  ns.

These results have recently been published: G. Ranjit, N. A. Schine, A. T. Lorenzo, A. E. Schneider, and P. K. Majumder, Phys. Rev. A **87**, 032506 (2013). The author made significant contributions at all stages of the writing and publishing process, and has presented this work numerous times, including at a recent meeting of the APS New England section.

# Contents

Abstract . . . . .	iii
Acknowledgments . . . . .	v
Executive Summary . . . . .	vii
<b>1 Introduction</b>	<b>1</b>
1.1 The Standard Model . . . . .	1
1.1.1 Tests by Heavy Atoms . . . . .	2
1.1.2 Beyond the Standard Model . . . . .	3
1.2 Present Work . . . . .	4
1.2.1 The Stark Shift . . . . .	5
1.2.2 Lifetimes . . . . .	7
1.3 Outline of the Thesis . . . . .	9
<b>2 Atomic Absorption</b>	<b>11</b>
2.1 Fundamental Line Shape . . . . .	11
2.2 Lineshapes of Direct Absorption . . . . .	12
2.2.1 The Complex Index of Refraction . . . . .	12
2.2.2 Homogeneous and Inhomogeneous Broadening: The Voigt Profile	13
<b>3 FM Spectroscopy and Line Shapes</b>	<b>19</b>
3.1 Single Tone Modulation . . . . .	19
3.2 1f Demodulation . . . . .	22
3.3 2f Demodulation . . . . .	24
3.4 Complications to the Observed FM Lineshape . . . . .	25
<b>4 Experimental Apparatus</b>	<b>29</b>
4.1 Atomic Beam Apparatus . . . . .	29
4.1.1 Atomic Beam Source . . . . .	29
4.1.2 Collimation and Interaction . . . . .	30
4.2 Optical System . . . . .	33
4.2.1 Diode Laser . . . . .	34
4.2.2 Laser Control and Frequency Monitoring . . . . .	34
4.2.3 FM Implementation and Prerecording Signal Analysis . . . . .	36
4.3 Data Acquisition . . . . .	36
4.3.1 Summary of Collected Data . . . . .	37

<b>5</b>	<b>Data Analysis</b>	<b>39</b>
5.1	Data Fitting . . . . .	39
5.1.1	Frequency Linearization and Calibration . . . . .	39
5.1.2	Fitting Program Details . . . . .	40
5.1.3	Approximation Methods . . . . .	43
5.2	Extraction of $k_S$ . . . . .	46
5.3	Investigation of Systematic Errors . . . . .	49
5.3.1	Binary Variables and Correlation Plots . . . . .	49
5.3.2	Continuous Correlations . . . . .	51
5.3.3	Final Uncertainties and Results . . . . .	53
<b>6</b>	<b>Ongoing and Future Work</b>	<b>55</b>
6.1	Thallium Lifetimes . . . . .	55
6.2	Two Step Excitation: the $6P_{3/2}$ Polarizability . . . . .	55
6.2.1	Two Tone Modulation . . . . .	57
6.2.2	Rough Estimate of Magnitude . . . . .	60
6.2.3	Tensor Polarizability . . . . .	62
6.2.4	P-D Linestrengths . . . . .	63
6.3	Further Options in Thallium . . . . .	64
6.3.1	Probing the 1283 nm ‘Forbidden’ $6P_{1/2} \rightarrow 6P_{3/2}$ M1/E2 Transition . . . . .	64
<b>A</b>	<b>Atomic Units</b>	<b>66</b>
<b>B</b>	<b>Other Broadening Mechanisms</b>	<b>69</b>
<b>C</b>	<b>Frequency Modulated Fabry-Pérot</b>	<b>73</b>
<b>D</b>	<b>FM Signal Derivation</b>	<b>79</b>
D.1	1f Signal . . . . .	79
D.2	2f Signal . . . . .	81
<b>E</b>	<b>Non-Ideal Modulation</b>	<b>85</b>
<b>F</b>	<b>Saturated Absorption Theory</b>	<b>89</b>

# List of Figures

1	Comparison of Results . . . . .	vii
2	The Interaction Region . . . . .	viii
3	Histogram of Data . . . . .	ix
1.1	Indium and Thallium Energy Level Diagram . . . . .	3
1.2	Polarizability Difference Comparison . . . . .	8
1.3	6P Lifetime Comparisons . . . . .	9
2.1	Comparison of Absorption and Dispersion . . . . .	14
3.1	A Fabry-Pérot Scan . . . . .	20
3.2	FM Laser Frequency Spectrum . . . . .	21
3.3	Low $\beta$ FM Signal Simulation . . . . .	23
3.4	1f FM Signals . . . . .	24
3.5	2f FM Signals . . . . .	25
3.6	Difference in First Order Sidebands: No Resolved RAM . . . . .	26
4.1	Diagram of Vacuum System . . . . .	30
4.2	Oven and Crucible . . . . .	31
4.3	HV Circuit Diagram . . . . .	32
4.4	Experimental Setup . . . . .	33
4.6	Data Acquisition Diagram . . . . .	36
4.5	Simultaneous Signals . . . . .	37
5.1	Linearization Procedure . . . . .	41
5.2	Saturated Absorption Fit . . . . .	42
5.3	Polynomial Fitting for Shift Extraction . . . . .	43
5.4	Overlap Method Histograms . . . . .	44
5.5	Linear Approximation for Shift Extraction . . . . .	45
5.6	Sample Signals with Lorentzian Fitting for Shift Extraction . . . . .	46
5.7	One Day of Data: Linear Extraction of $ k_S $ . . . . .	47
5.8	Histogram of All Data . . . . .	48
5.9	Comparison of Binary Systematic Variations . . . . .	50
5.10	A Model of Experimental Correlation . . . . .	51
5.11	A Correlation Plot . . . . .	52
5.12	Two Continuous Correlations . . . . .	53

6.1	Stark Shifted Energy Level Diagram . . . . .	56
6.2	Spectra of Regular and Two-Tone FM . . . . .	58
6.3	Second Step Stark Shift Experimental Setup . . . . .	59
6.4	Simulated Two Tone Demodulated Signal . . . . .	59
6.5	Indium Energy Level Diagram . . . . .	60
6.6	Forbidden Transition Diagram . . . . .	65
B.1	Power Broadened Resonance Profile . . . . .	71
C.1	Fabry-Pérot Cavity Schematic . . . . .	74
E.1	Bessel Functions . . . . .	85
E.2	Zeroth Order Peak Heights: Unmodulated Power Through EOM . . .	86
E.3	Frequency Components vs. Modulation Depth . . . . .	87
E.4	Difference in First Order Sidebands: No Resolved RAM . . . . .	88
F.1	Saturated Absorption Line Shape . . . . .	90
F.2	Oven Diagram . . . . .	90
F.3	Saturated Absorption System Setup . . . . .	91
F.4	Misalignment Diagram . . . . .	92

# List of Tables

2.1	Sources of Broadening . . . . .	14
5.1	Potential Variables for Systematic Errors . . . . .	49
5.2	Sources of Experimental Uncertainty . . . . .	54
6.1	Rough Estimation of Polarizabilities . . . . .	61
6.2	Published Theoretical Polarizabilities . . . . .	64
A.1	Quantities Taken to Unity in Atomic Units . . . . .	66
A.2	Units of Other Dimensions . . . . .	66
A.3	Convenient Physical Quantities in Atomic Units . . . . .	67
A.4	Useful Conversions in Atomic Units . . . . .	67



# Chapter 1

## Introduction

In the Majumder lab, we study the atomic properties of Group IIIA atoms, atoms which have become increasingly important in tests of the Standard Model and possible extensions to it. Measurements such as ours challenge the current atomic theory towards more precise predictions of atomic properties. This interplay between experiment and theory has formed the basis of highly productive advances in current knowledge, and it is towards this end that we present this present work.

### 1.1 The Standard Model

The Standard Model describes the interaction of elementary particles to great precision. It combines the theory of the electroweak interaction, which is itself the combined description of electromagnetic and weak forces, with quantum chromodynamics, the current description of the strong interaction. For the last forty years, the Standard Model has been repeatedly confirmed in high-energy particle collider experiments, yet is known nevertheless to be incomplete.<sup>1</sup> Atoms provide an altogether different system in which to investigate the Standard Model, being both very low energy and relatively easy to control. Multiple experiments in atomic systems [1–4] have helped determine parameters in the Standard Model to precision comparable to that provided by high-energy particle accelerator experiments. Beyond confirmations of the Standard Model, atomic systems have become essential in certain descriptions of physics beyond the Standard Model, such as in permanent electron electric-dipole-moment (EDM) searches. Beyond the more obvious interest in understanding atomic properties, the relevance of detailed descriptions of atomic systems to fundamental physics is well established.

The experiments mentioned above are useful because they extract measurements of some atomic observable that depend on the fundamental interaction of interest. This observable,  $\epsilon_w$ , (e.g. an optical rotation induced by the weak interaction), may

---

<sup>1</sup>A complete theory must needs include gravity, as well as explain unpredicted observed phenomena such as the neutrino mass, the  $t\bar{t}$  forward-backward asymmetry from the Tevatron, and the excessive decay rate from the process  $B \rightarrow D^* \tau \nu$  from BaBar.

be written as,

$$\epsilon_w = Q_w C(Z). \quad (1.1)$$

$Q_w$  represents the effects of the fundamental interaction and, once determined, provides a value for one or a collection of parameters in the theory of that interaction (such as the weak mixing angle  $\sin^2 \theta_W$  for [1]).  $C(Z)$  quantifies the dependence of the effect on the details of the atomic system, since the same interaction becomes manifest to differing degrees depending on the atom of choice. Nevertheless, the uncertainty in  $Q_w$ , which corresponds to uncertainty in the parameters of the fundamental theory, arises from the combined uncertainties from the experimental measurement of  $\epsilon_w$  and the theoretical understanding of  $C(Z)$ .

### 1.1.1 Tests by Heavy Atoms

Observables such as  $\epsilon_w$  depend on the overlap of the electron and nuclear wavefunctions; for this reason,  $C(Z)$  is represented as a function dependent on the atomic number  $Z$ . It has been shown that, for observables like  $\epsilon_w$ ,  $C(z)$  scales very rapidly with atomic number, that is,  $C(Z) \propto Z^3$  [5]. Therefore, the most precise atomic physics extractions of parameters in the Standard Model come through experiments on heavy atomic systems such as thallium. Unfortunately, precise calculations of  $C(Z)$  also require detailed knowledge of the electronic structure of these many-electron systems.<sup>2</sup> This has spurred atomic theory groups such as Safronova, *et al.* to generate and implement approximation methods to make solutions of the Schrödinger equation accessible. Such *ab initio* wavefunction calculations also predict many other atomic observables, such as transition amplitudes, hyperfine splittings, isotope shifts, and state polarizabilities. It is the project of the Majumder lab to measure to very high precision these additional observables in the relevant elements. These measurements become benchmark tests of the atomic theory that are essential for the calculation of  $C(Z)$ .

### Indium and Thallium

Both indium and thallium have three valence electrons: two  $s$  electrons and one  $p$  electron. This similarity results in very similar atomic structure (see Fig. 1.1), which means that the approximation methods for the calculation of electron wavefunctions are likewise similar. Therefore, measurements in indium have great relevance for testing not just the theory of indium but also the theories of thallium and gallium. The Majumder lab has completed many of the relevant measurements of atomic observables in thallium and is moving towards measurements in indium where less high-precision work has been focused. Indium also has the great advantage (which my fiancée surely appreciates) over thallium of not being highly poisonous.

---

<sup>2</sup>Appendix A of [6] explains the application of  $C(Z)$  to [1], in which  $C(Z)$  depends explicitly on electric dipole matrix elements. Thus, uncertainty in the electric dipole matrix elements contributes directly to the uncertainty in the experimental determination of  $\sin^2 \theta_W$ .

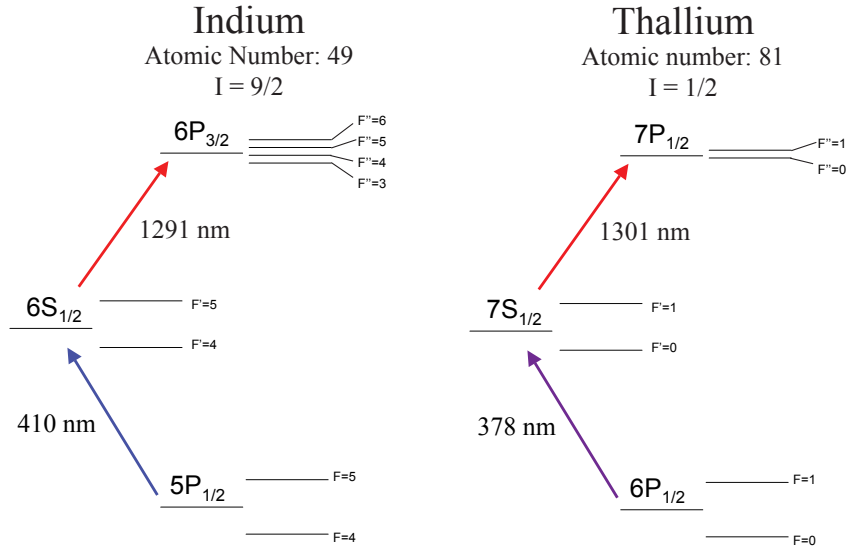


Figure 1.1: A partial energy level diagram of the valence electron in indium and thallium. Similar atomic structure results in similar transition energies.

### 1.1.2 Beyond the Standard Model

#### Permanent Electron EDM

Many searches for physics beyond the Standard Model look for deviations from theory within manifestations of time-reversal ( $T$ ) symmetry violation, which, via the  $CPT$  theorem, implies  $CP$  violation as well.  $CP$  violation has currently only been measured in decays of neutral Kaons and  $B_d^0$ -Mesons [7, 8]. The Standard Model incorporates these occurrences of  $CP$  violation through the Kobayashi-Maskawa mechanism; however, it is believed that this mechanism is an incomplete description of  $CP$  violation. Furthermore, it has been shown that the KM mechanism predicts a negligibly tiny permanent electric dipole moment (EDM) of the electron, and that several current theories that extend the Standard Model, including multiple multi-Higgs models and certain supersymmetric models, do predict a sizable permanent electron EDM nearly within reach of current experimental sensitivity [9–11]. Thus, a measurement of the electron EDM would provide good evidence for new physics beyond the Standard Model and is feasible if these models are correct. Current upper limits on the electron EDM are provided by [12] in mercury and more precisely by [11] in thallium.

Given the recent success of [13] in laser cooling an indium atomic beam, Sahoo, Pandey, and Das have proposed a search for a permanent EDM using atomic indium [14]. Indium is particularly relevant for this search since the EDM enhancement factor for indium – the conversion ratio between the detectable atomic EDM and the fundamental electron EDM (Eq. (5) in [14]) – has been calculated to unusually high precision, and, more importantly, shown to be large. The enhancement factor depends explicitly on the reduced E1 matrix elements of indium, and the most precise calcu-

lations of these matrix elements come from Safronova *et al.* [15]. The present work provides a benchmark test of Safronova’s atomic theory, thus offering confirmation of the high precision of the EDM enhancement factor calculations in indium.

### Tests of the Time Variation of $\alpha$

Some models of the early universe posit that the fundamental constants of physics had values different than they have now [16]. This becomes manifest in a shifted value of the fine structure constant ( $\alpha = \frac{e^2}{(4\pi\epsilon_0)\hbar c} = \frac{e^2 c \mu_0}{2\hbar}$ ), which in turn results in altered magnitudes of fine structure splittings. Since the ratio of fine structure splittings to an optical transition frequency is proportional to  $\alpha^2 Z^2$ , precise measurements of the spectra of distant quasars can search for a different value of the fine structure constant [17–19]. While the postulated change in  $\alpha$  is relatively large over cosmological time scales, the fifteen digits of precision possible in metrology and precision spectroscopy have prompted many groups to search for a time dependence of  $\alpha$  in atomic transitions over human timescales. Table III in [16] provides a summary of all constraints on  $\alpha$  up through 2003.<sup>3</sup> Work has continued in this field over the last decade, particularly in calculating which atomic transitions depend most strongly on  $\alpha$  [19–23]. While many of these transitions are in transition metal ions that have little in common with the trivalent atoms studied in the Majumder lab, some ions with transition frequencies that depend particularly strongly on  $\alpha$  are, in fact, indium-like ions. Thus, high-precision work like ours in this atomic system has relevance for future high precision spectroscopy and atomic theory in such indium-like systems.

Both of these realms of research into physics beyond the Standard Model are currently looking for a ‘zeroth-order’ detection of any effect. However, detailed knowledge of the atomic theory of indium and other Group-III elements is important for knowing that the effect of interest is predicted to be large in these systems, and, if the effect is detected, this knowledge is essential for a ‘first-order’ comparison of the magnitude of the effect with the theory.

## 1.2 Present Work

It has become increasingly relevant to understand the precise valence electronic wavefunctions in indium. Herein we describe the theory and procedures used to measure observables necessary to test the state-of-the-art atomic theory. In particular, we probe the 410 nm  $5P_{1/2} \rightarrow 6S_{1/2}$  transition in indium (see Fig. 1.1). By measuring the Stark shift therein, we extract the polarizability difference between the levels of the transition as well as lifetimes of the  $6P$  states of indium. The new measurements described in this work agree with state-of-the-art atomic theory.

---

<sup>3</sup>None of which are particularly convincing. Unfortunately, there is not a more recent compendium of constraints.

### 1.2.1 The Stark Shift

An external electric field causes a perturbation of the Hamiltonian of an atom's electrons that results in an energy shift of each energy level. Before diving into the second order perturbation theory, it is worth having an intuitive sense of this effect. The external electric field creates mixing between otherwise separate energy levels (the basis of orthogonal energy eigenstates corresponding to the familiar energy level structure become 'rotated' so that energy eigenstates have components in several energy levels). The 'virtual transitions' caused by the external field in turn cause energy level repulsion, in which energy levels shift away from nearby levels by an amount inversely proportional to their energy separation. Higher energy levels of the valence electron are closer together, so we expect the Stark shift to shift energy levels lower, shifting the higher energy states more than lower energy states.

There are two types of Stark shifts, AC and DC. AC Stark effects are typically associated with intense laser light, where AC refers to the oscillation of the electric field of the laser, and the magnitude of the effect depends on the detuning of the laser from atomic absorption lines. DC Stark effects occur due to a static, DC electric field, such as that produced between two charged capacitor plates. In order to measure the effect of DC electric fields, we generate 10-20 kV/cm fields, where, for comparison, the dielectric breakdown of air is approximately 30 kV/cm [24]. Now to the quantum mechanics.

We consider an atom subject to an external DC electric field of magnitude  $E$ , where the field direction defines the positive  $z$  direction. The Hamiltonian for the valence electron becomes

$$H = H_0 + eEz. \quad (1.2)$$

First order perturbation theory tells us that, to first order in  $E$ , the electric field has no effect on the energy level structure of the valence electron.<sup>4</sup>

$$\begin{aligned} \Delta\mathcal{E}^{(1)}(\xi) &= eE \langle \psi_\xi^{(0)} | z | \psi_\xi^{(0)} \rangle \\ &\propto eE \int_{-\infty}^{\infty} |\psi_\xi^{(0)}|^2 z dz \\ &= 0. \end{aligned} \quad (1.3)$$

We use  $\mathcal{E}_\xi$  to denote the energy of level  $\xi$  to avoid confusion with the electric field  $E$ , and the superscript denotes the order of perturbation considered. Second order perturbation theory does provide a useful result. Starting with

$$\Delta\mathcal{E}^{(2)}(\xi) = \sum_{k \neq \xi} \frac{|\langle \psi_k^{(0)} | eEz | \psi_\xi^{(0)} \rangle|^2}{\mathcal{E}^{(0)}(k) - \mathcal{E}^{(0)}(\xi)}, \quad (1.4)$$

---

<sup>4</sup>*Degenerate* perturbation theory can give rise to a linear Stark effect, as in the famous  $n = 2$  states in hydrogen. However, even the hyperfine splittings in indium are tens of gigahertz, so none of the relevant states are degenerate.

we can factor out  $E^2$  and recast the matrix elements  $\langle \psi_k^{(0)} | ez | \psi_\xi^{(0)} \rangle$  as elements of the reduced electric-dipole (E1) matrix [25, 26]. This leaves us with

$$\Delta\mathcal{E}^{(2)}(\xi) = \frac{-1}{3(2j_\xi + 1)} E^2 \sum_{k \neq \xi} \frac{\langle k || D || \xi \rangle^2}{\mathcal{E}^{(0)}(k) - \mathcal{E}^{(0)}(\xi)} \quad (1.5)$$

$$= -\frac{1}{2} \alpha_0(\xi) E^2, \quad (1.6)$$

where  $\alpha_0(\xi)$  is the scalar polarizability of the state  $\xi$  of the valence electron in  $^{155}\text{In}$ . In general, the polarizability of atoms does depend on the polarization of the resonant light, a dependence which is expressed in an additional tensor polarizability. However, the tensor polarizability is zero for  $j = 1/2$  states. Since we are studying the 410 nm  $5P_{1/2} \rightarrow 6S_{1/2}$  transition, we need therefore only consider the scalar polarizability. Nevertheless,  $\alpha_0(\xi)$  is the state dependent coefficient between the energy shift and the electric field squared, subsuming the angular pre-factor and radial sums into one coefficient;

$$\alpha_0(\xi) = \frac{2}{3(2j_\xi + 1)} \sum_{k \neq \xi} \frac{\langle k || D || \xi \rangle^2}{\mathcal{E}^{(0)}(k) - \mathcal{E}^{(0)}(\xi)}. \quad (1.7)$$

The polarizability of a particular state may be directly measured experimentally as in [27]; however, it is much easier to measure the energy difference between two states, e.g. by driving a transition with a laser. An applied electric field causes both states in the transition to shift to lower energies, but by differing amounts. This results in a frequency shift for the transition corresponding to the difference in the energy shifts of each state. For our transition, we can now write the observed frequency Stark shift as

$$\Delta\nu_S = -\frac{1}{2h} [\alpha_0(6S_{1/2}) - \alpha_0(5P_{1/2})] E^2 \quad (1.8)$$

$$= k_S E^2. \quad (1.9)$$

In our atomic beam apparatus, we can measure  $k_S$  directly in units of  $\frac{\text{kHz}}{(\text{kV/cm})^2}$ . This immediately translates into a value equal to the difference between two infinite sums of reduced electric dipole matrix elements weighted by their frequency difference from the considered state. Since it is the stated project of many atomic theorists to calculate *ab initio* these matrix elements, measuring the Stark shift provides a stringent test of atomic theory.

We perform this measurement by detecting the transmission of the laser after crossing transversely through our atomic beam. We find that, as expected, the transmission profile shifts by 10-50 MHz towards lower frequencies depending on the field (10-20 kV/cm) applied. The two primary challenges, then, are

1. creating and understanding line shapes that have a high signal to noise ratio and are resolved on the MHz level, and

2. precisely extracting the characteristic frequency of the transmission signal so that the Stark shift may be revealed.

Given the low density of atoms in the atomic beam, the direct transmission signal has a terrible signal to noise ratio; indeed, absorption of the light is not even detected. We overcome this through the use of high sensitivity frequency modulation spectroscopy. In order to resolve shifts only several MHz in magnitude, we must precisely control the laser frequency as well as understand all sources of line shape broadening and then work to minimize or eliminate them. Only then will the spectral features be sufficiently sharply defined that a shift in frequency may be precisely measured. Finally, we must develop sophisticated frequency scale linearization and calibration techniques as well as methods for the reliable extraction of a frequency reference from the transmission signal.

The final result of our work is the determination of  $k_S = -122.92(33) \frac{\text{kHz}}{(\text{kV/cm})^2}$ , corresponding to a difference in polarizability between the  $6S_{1/2}$  and  $5P_{1/2}$  states in  $^{115}\text{In}$  of

$$\Delta\alpha_0 = 1000.2(2.7) \text{ a.u.} \quad (1.10)$$

This is a factor of 29 more precise than, although in agreement with, an earlier measurement by Fowler and Yellin:  $\Delta\alpha_0 = 944(73)$  a.u. [28]. Furthermore, this result is in excellent agreement with a new *ab initio* theory calculation by Safronova, *et al.* of  $\Delta\alpha_0 = 995(20)$  a.u. (see Fig. 1.2) [29].

Note that these values are given in atomic units to follow the standard of the literature. For a review of this system of natural units, please see Appendix A.

### 1.2.2 Lifetimes

Beyond an experimental test of theoretically predicted polarizabilities, it can be shown that our result, combined with new theoretical understanding of the reduced dipole matrix elements, may be used to extract a model dependent experimental value for the  $6P_{1/2}$  and  $6P_{3/2}$  excited state lifetimes [29, 30]. While  $\Delta\alpha_0$  is, in principle, the balance between infinite sums, as shown in Eq. (1.7), Safronova has shown that the  $6S_{1/2} - 6P_{1/2;3/2}$  terms in the  $6S_{1/2}$  polarizability sum comprise about 94% of all contributions in *both* the  $6S_{1/2}$  and  $5P_{1/2}$  polarizability sums [29]. As in [30], the expression for the polarizability difference between the  $6S_{1/2}$  and  $5P_{1/2}$  states may be rewritten to express this imbalance in terms.

$$\Delta\alpha_0 = B \cdot S + C, \quad (1.11)$$

where  $S$  is the E1 line strength,  $S \equiv \langle 6P_{1/2} || D || 6S_{1/2} \rangle^2$ , and

$$B = \frac{1}{3} \left( \frac{1}{\mathcal{E}_{6P_{1/2}} - \mathcal{E}_{6S_{1/2}}} + \frac{R^2}{\mathcal{E}_{6P_{3/2}} - \mathcal{E}_{6S_{1/2}}} \right) \quad (1.12)$$

where  $R$  is the ratio of the reduced E1 matrix elements,  $R = \frac{\langle 6P_{3/2} || D || 6S_{1/2} \rangle}{\langle 6P_{1/2} || D || 6S_{1/2} \rangle}$ , and  $C$  is the sum of the remaining terms. Safronova has calculated in [29] the following

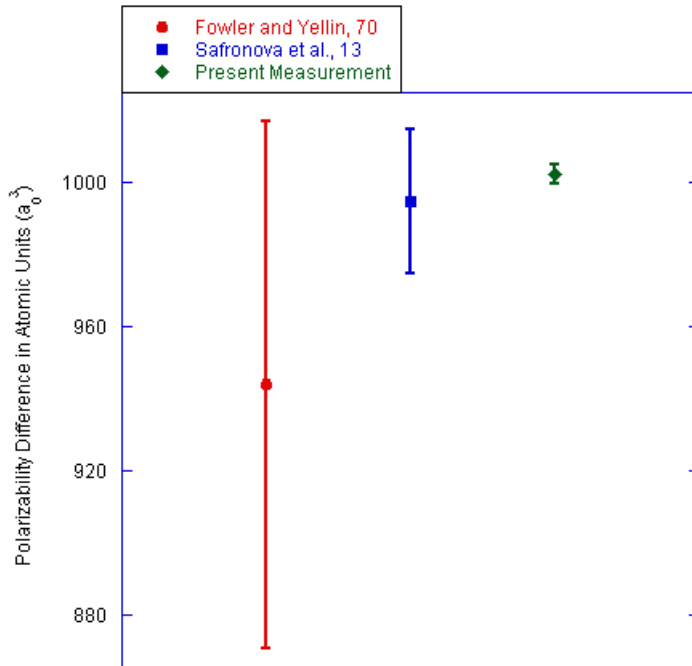


Figure 1.2: A comparison of values for the polarizability difference between the  $6S_{1/2}$  and  $5P_{1/2}$  states in indium. On the left is the previous experimental measurement, in the middle is the recent theoretical result, and on the right is our present measurement.

values:  $R^2 = 1.949(2)$  a.u. and  $C = -60(8)$  a.u. Since we, in the Majumder lab, have experimentally measured  $\Delta\alpha_0$ , we can use these theoretical calculations to compute the E1 line strength  $S$ . As in [31], we can relate the line strength to the decay rate needing only the well known energy splitting between the states:

$$A_{ab} = \frac{2.02614 \times 10^{18}}{\lambda^3} \frac{S_{ab}}{(2j_a + 1)} \text{s}^{-1}, \quad (1.13)$$

where the line strength  $S_{ab}$  is in atomic units and the transition wavelength  $\lambda$  is in Ångströms. Since from each of these states, there is only one decay channel, the lifetime  $\tau_a$  is simply the inverse of  $A_{ab}$ . Propagating all uncertainties through, we find that the final uncertainties for the lifetimes are dominated by the theoretical uncertainty in  $C$ . We infer the following values for lifetimes of the  $6P_{1/2}$  and  $6P_{3/2}$  states in indium:

$$\tau_{6P_{1/2}} = 63.77(50) \text{ ns} \quad (1.14)$$

$$\tau_{6P_{3/2}} = 58.17(45) \text{ ns}. \quad (1.15)$$

With uncertainties below 1%, an order of magnitude more precise than prior pulsed laser spectroscopy measurements [32], our measurement is in excellent agreement with recent independent theoretical predictions (see Fig. 1.3) [31].

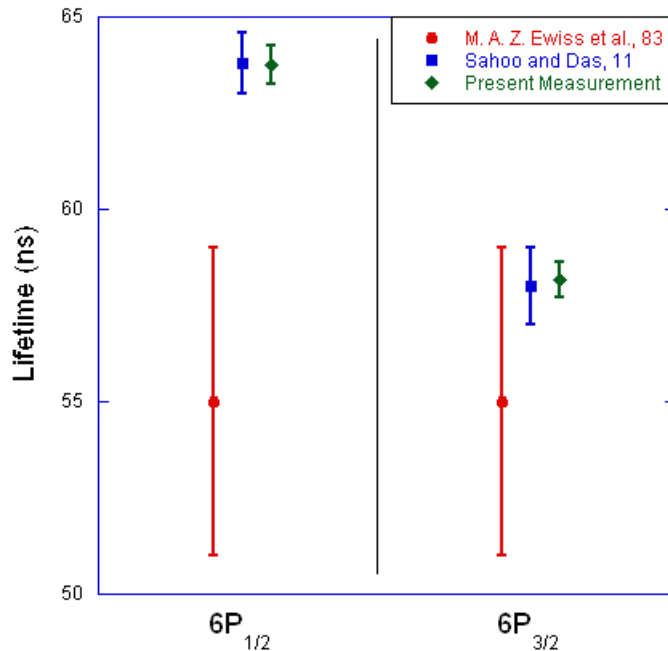


Figure 1.3: A comparison of values for the lifetimes of the  $6P_{1/2}$  and  $6P_{3/2}$  states in indium.

### 1.3 Outline of the Thesis

The following chapters present a detailed analysis of the underlying theory, methods, and apparatuses used in obtaining our measured Stark shift. Chapter 2 develops the background theory of atomic absorption profiles, and chapter 3 presents frequency modulation spectroscopy along with the analytic form of FM line shapes. Chapter 4 introduces the experimental apparatus, concluding with a summary of the data collected with our equipment. Chapter 5 begins with a discussion of the structure of the data fitting program and moves into an analysis of the  $k_S$  extraction and the systematic error investigation. At this point, we have concluded the present work, having arrived at our final results as quoted in Eqs. (1.10) and (1.15) and represented in Figs. 1.2 and 1.3. Chapter 6 outlines future work to be accomplished, focusing specifically on the addition of a 1291 nm IR laser to probe and measure the Stark shift in the  $6S_{1/2} \rightarrow 6P_{3/2}$  transition.



# Chapter 2

## Atomic Absorption

The source of most of our collective knowledge about atoms and molecules is spectroscopy, the study of the interaction of atoms with light. Electrons may be excited from one energy level to another by absorbing a photon of energy equal to the difference between levels, and when the electrons relax to lower energy states, they likewise emit photons. In our experiment, measurement of the atoms' fluorescence turns out to be unfeasible, but we can detect the absorption through small changes in laser transmission. By manipulating and studying the frequency dependent response of lasers to a sample of atoms, we can study the properties of electrons, atomic nuclei, and even the fundamental physics of the Standard Model. Anyone attempting to use this powerful method of investigation must first understand the theoretical basis of spectroscopic line shapes.

### 2.1 Fundamental Line Shape

An atom has a probability of absorbing light that is near one out of a set of specific 'resonant' frequencies corresponding to energy differences between energy levels in the atom. If we send light waves with a frequency  $\omega$  that is near a resonant frequency  $\omega_0$  a distance  $dz$  through a sample of atoms, the intensity of the wave will decrease by

$$dI = -A(\omega)I dz \quad (2.1)$$

where  $A(\omega)$  quantifies the atoms' absorption of the light at frequency  $\omega$ . It is clear that  $A(\omega)$  must be proportional to the density of atoms,  $n$ , and each atom's quantum mechanical absorption cross section,  $\sigma(\omega)$ , which may be written as an overall cross section  $\sigma_0$  times a normalized frequency dependent probability function,  $P(\omega)$ . Thus  $A(\omega) = n\sigma_0 P(\omega)$ . Integration yields the resultant intensity as a function of both frequency  $\omega$  and the length of interaction,  $z$ .

$$I(\omega, z) = I_0 e^{-\alpha_0 P(\omega)} \quad (2.2)$$

where  $\alpha_0 = n\sigma_0$ , a unitless measure of attenuation, is called the optical depth. At sufficiently high optical depths, for our experiment  $\alpha_0 \gtrsim 0.05$ , direct measurement

of transmitted light will provide a detectable atomic absorption dip. In 2002, thesis student Charles Doret completed a measurement of the Stark shift in thallium that used such measurements of direct absorption where  $\alpha_{0,Tl} \approx 0.5$ . However, since indium has a vapor pressure roughly three orders of magnitude smaller than thallium for a given temperature, our maximum achievable optical depth for indium is in the realm of  $10^{-4}$ . We have addressed this problem by building a new, hotter atomic beam source oven, which heats the indium to  $\sim 900^\circ C$ ,  $150^\circ C$  hotter than the thallium oven. This has increased our optical depth by an order of magnitude; however, detecting laser attenuations of order  $10^{-3}$  is still impractical. It is better to use a more sophisticated approach.

We could attempt to look for fluorescence. Any electron excited to the  $6S_{1/2}$  state will decay within several lifetimes,  $\tau_{6S} \approx 7$  ns [33]. It will fall either to the  $5P_{1/2}$  level by emitting a 410 nm photon or the  $5P_{3/2}$  level by emitting a 451 nm photon. Thus the sample will fluoresce at both 410 nm and 451 nm, approximately halving either fluorescence signal. More critically, the geometrical configuration of the interaction of the atomic beam and the laser between large capacitor plates results in a narrow solid angle available for light collection. Therefore, fluorescence detection is not realistic, and so we must measure absorption of the laser light by the atoms. Since direct absorption does not yield a strong signal, we employ frequency modulation spectroscopy. At this point, it behooves us to review the theory of direct absorption line shapes before proceeding to the theory of frequency modulated line shapes, as the former will be critically important during any discussion of the latter.

## 2.2 Lineshapes of Direct Absorption

Here we will derive the absorption and dispersion of a laser beam passing through a sample of atoms. We begin by modeling the atoms as a material with a complex index of refraction.

### 2.2.1 The Complex Index of Refraction

A sample of atoms both attenuates and shifts the phase of light that is passing through it. Both of these effects depend on the frequency of the laser. In order to quantify these effects, we model this interaction as a plane wave electromagnetic wave with the complex electric field  $\tilde{E} = E_0 e^{i(\omega t - kz)} \hat{s}$  (with  $\hat{s} \cdot \hat{z} = 0$ ) incident upon a medium with a complex index of refraction,

$$n(\omega) = n' - i\kappa. \quad (2.3)$$

Following [34], who considers the resonant transition as a damped oscillator driven by the electric field of the laser, we rewrite the right hand side of Eq. (2.3) as

$$n(\omega) = 1 + \frac{C}{(\omega - \omega_0) + i\Gamma/2} \quad (2.4)$$

where  $C$  is a constant expressing the combined effects of the quantum mechanical transition probability, the number of atoms, etc.,  $\Gamma$  is a damping constant, and  $\omega_0$  is the frequency of the atomic resonance. Assuming the medium has only a scalar polarizability, when the plane wave of the laser passes through the medium, the wave vector changes:  $k(n) = k_0 n$  where  $k_0 = \frac{\omega_0}{c}$ . Thus, after passing through a distance  $z$  of the material, the electric field is

$$\begin{aligned}\tilde{E}' &= E_0 e^{i(\omega t - k_0 n z)} \hat{s} \\ &= E_0 e^{-k_0 \kappa z} e^{i(\omega t - k_0 n' z)} \hat{s}\end{aligned}\quad (2.5)$$

We can now define a complex transmission function  $\tilde{T}(\omega)$  such that  $\tilde{E}' = \tilde{T}(\omega) \tilde{E}$ .

$$\tilde{T}(\omega) = e^{-\delta(\omega) - i\phi(\omega)} \quad (2.6)$$

$$= e^{-k_0 \kappa z - i(n' - 1)k_0 z} \quad (2.7)$$

Plugging in with Eq. (2.4) yields the absorption  $\delta(\omega)$  and the dispersion  $\phi(\omega)$ .

$$\delta(\omega) = \kappa k_0 z = \frac{\alpha'_0}{2} \frac{\Gamma/2}{(\omega_0 - \omega)^2 + \Gamma^2/4} = \frac{\alpha_0}{2} \frac{\Gamma^2/4}{(\omega_0 - \omega)^2 + \Gamma^2/4} \quad (2.8)$$

$$\phi(\omega) = (n' - 1)k_0 z = \frac{\alpha'_0}{2} \frac{\omega_0 - \omega}{(\omega_0 - \omega)^2 + \Gamma^2/4} = \frac{\alpha_0}{2} \frac{\Gamma/2(\omega_0 - \omega)}{(\omega_0 - \omega)^2 + \Gamma^2/4} \quad (2.9)$$

where  $\alpha'_0/2 = Ck_0 z$  and  $\alpha_0/2 = 2Ck_0 z/\Gamma$  as required by the normalization of  $\delta$  (see Fig. 2.1). The intensity of the laser after passing through the medium is therefore

$$I \propto \tilde{E}' \tilde{E}'^* = I_0 e^{-2\delta(\omega)} = I_0 e^{-\alpha_0 \frac{\Gamma^2/4}{(\omega_0 - \omega)^2 + \Gamma^2/4}} \quad (2.10)$$

## 2.2.2 Homogeneous and Inhomogeneous Broadening: The Voigt Profile

For small optical depths, the absorption signal derived above is a narrow Lorentzian dip of width  $\Gamma$  about the resonant frequency  $\omega_0$ . In practice, though, experimentalists commonly observe absorption dips tens or even hundreds of times broader than this implies. In other words, atoms must be interacting and absorbing light at frequencies much further from resonance than section 2.2.1 predicts. In order to understand experimentally observed line shapes, it is critical to examine all potential mechanisms for line shape broadening. Throughout this analysis, we will assume the following representative operating conditions: vapor cell and atomic beam temperatures of 800°C, laser power of 1 mW, and laser cross section of 1 mm<sup>2</sup>. We intentionally varied these experimental parameters, so the absolute size of the following broadening effects varied; however, this is sufficient for revealing relative magnitudes and the general scales of these effects. Table 2.1 offers a concise quantified comparison of the various

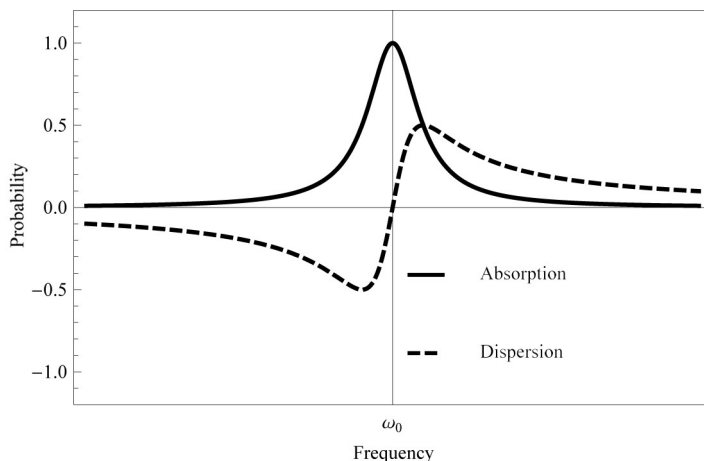


Figure 2.1: Absorption and dispersion through a sample of atoms near a resonance. Note that the relative amplitudes are fixed and are generally (for us) small, i.e.  $\delta, \phi \ll 1$

Broadening Mechanism	FWHM	
	Vapor Cell	Atomic Beam
Natural Width	21 MHz	21 MHz
Doppler Broadening	1.4 GHz	70 MHz
Laser Line-width	2 MHz	2 MHz
Pressure Broadening	10 kHz	0 kHz
Power Broadening	200 kHz	10 kHz
Transit-Time Broadening	480 kHz	550 kHz
<i>Voigt Convolution Total</i>	1.4 GHz	83 MHz

Table 2.1: A comparison of potential sources of broadening for the  $5P_{1/2} \rightarrow 6S_{1/2}$  transition in indium at representative experimental conditions.

sources of broadening in terms of the additional full width at half maximum (FWHM) of the absorption profile.

The mechanisms of line broadening break down into two classes: homogeneous and inhomogeneous, where all but Doppler broadening fall into the first category. Homogeneous mechanisms affect all atoms equally, whereas inhomogeneous mechanisms partition and operate on classes of atoms differentially based on some metric. As will be discussed below, the Doppler effect places atoms into “longitudinal velocity classes,” within which the effect is uniform but between which the effect varies. These sources of broadening do not all take the same analytic form, but we quantify their width as the FWHM of the profile.

### Natural Width

Even under ideal experimental conditions, the absorption profile of a laser through a cloud of atoms is not a delta function, i.e.  $\Gamma$  is nonzero. This is because of an intrinsic quantum mechanical effect, the so-called natural width, which arises because of the finite lifetime,  $\tau_j$ , of any excited state. Heisenberg tells us that  $\Delta E \Delta t \leq \hbar$ . Since the time spent in the excited state is uncertain with  $\Delta t \simeq \tau_j$ , the energy  $E_{ij}$  that drives the transition from state  $i$  to state  $j$  is uncertain with  $\Delta E_{ij} \simeq \frac{\hbar}{\tau_j}$ . Therefore, the resonant laser frequency,  $\omega_0 = \frac{\omega_j - \omega_i}{\hbar}$ , has uncertainty  $\Delta\omega_{ij}$ , so any laser frequency  $\omega_0 - \Delta\omega_{ij}/2 < \omega < \omega_0 + \Delta\omega_{ij}/2$  can interact with the atoms. Thus, the natural linewidth  $\Gamma_{ij}$  is given by

$$\Gamma_{ij} = \frac{\Delta\omega_{ij}}{2\pi} = \frac{\Delta E_{ij}}{2\pi\hbar} = \frac{1}{2\pi\tau_j} \quad (2.11)$$

For the  $6S_{1/2}$  excited state in indium, the lifetime is  $\tau_{6S_{1/2}} \approx 7$  ns, [33] so the natural width of the  $5P_{1/2} \rightarrow 6S_{1/2}$  resonance is  $\Gamma_{nat} = \frac{1}{2\pi\tau_{6S_{1/2}}} \approx 21$  MHz.

### Doppler Broadening

Random thermal motion of atoms within a sample causes many atoms to move with a velocity component that is parallel to the direction of propagation of light. In the rest frame of the light source, the light has frequency  $\omega$ , while in the frame of an atom that is moving towards (positive longitudinal velocity,  $v_l$ ) the source of light, the light has frequency  $\omega'$  which is greater than  $\omega$  by the amount

$$\omega' - \omega = \omega \frac{v_l}{c} \quad (2.12)$$

This shift in frequency is the Doppler shift, made famous by passing ambulances and television weathermen. It means that even when the laser is significantly off resonance, say by a frequency shift  $\delta$ , such that no absorption should be predicted, any atoms that are moving with a longitudinal velocity

$$v_l = -\frac{c\delta}{\omega_0} \quad (2.13)$$

will see light at the resonance frequency  $\omega_0$  and so will absorb the light. Note that the negative sign ensures that the Doppler shift acts in the direction opposite the frequency offset  $\delta$ . Following [35], Maxwell and Boltzmann tell us the fraction of atoms in a gas that have a velocity (in a particular direction) between  $v$  and  $v + dv$ ,

$$f(v)dv = \sqrt{\frac{m}{2\pi kT}} e^{-\frac{mv^2}{2kT}} \quad (2.14)$$

where  $m$  is the mass of the atoms, in our case  $m = 115 \text{ a.m.u.} \cdot 1.661 \times 10^{-27} \frac{\text{kg}}{\text{a.m.u.}}$ ,  $k$  is Boltzmann's constant, and  $T$  is the temperature of the gas of atoms in Kelvin.

Using the relation given by (2.13), the absorption has a Gaussian line shape with a FWHM,  $\Delta$ , of

$$\Delta = \frac{\omega_0}{c} \sqrt{8 \log(2) \frac{kT}{m}}. \quad (2.15)$$

The full absorption profile is

$$\sigma^D(\omega) = \frac{c}{\omega_0} \sqrt{\frac{m}{2\pi kT}} e^{-\frac{m c^2}{2kT} \left(\frac{\omega - \omega_0}{\omega_0}\right)^2} = \frac{1}{\Delta \sqrt{2\pi \log 2}} e^{-\frac{(\omega - \omega_0)^2 4 \log 2}{\Delta^2}}, \quad (2.16)$$

where, in both equations,  $\log(a)$  denotes the natural logarithm of  $a$ . In a hot vapor cell with a temperature of 800°C, this results in a width of 1.4 GHz. Therefore, in a vapor cell under typical operating conditions, the Doppler broadening dominates all other sources of broadening by two orders of magnitude. In our atomic beam, due to our extensive efforts to collimate the beam, the angular spread of the atoms' velocities has been reduced by a factor of at least twenty. This results in a theoretical Doppler width for our absorption signal in the atomic beam of no more than 70 MHz. In actuality, we achieved a narrower Doppler width through the use of additional collimating features. Our parallel slit crucible faceplate and additional collimating masks reduced the Doppler width further to  $\sim 50$  MHz.

It is worth noting at this point that the Doppler effect partitions the atoms into velocity classes and causes a frequency shift dependent on that class. Thus, the Doppler shift is inhomogeneous, unlike the homogeneous natural line width, which is intrinsic to and equal for all atoms considered.

## Other Broadening Mechanisms

The two sources of line broadening mentioned so far turn out to be the dominant sources of broadening. There are various other potential sources of homogeneous broadening, namely laser line width, pressure, transit-time, and power broadening; however, these all turn out to be negligible. We displace their discussion here to Appendix B in favor of citing their values in Table 2.1. It turns out that all of these additional sources of broadening affect all atoms equally; that is, they are homogeneous mechanisms.

## Convolutions of Broadening Mechanisms: The Voigt Profile

At this point, we have reviewed all major contributions to the absorption line width. It now remains to show how these various contributions are to be combined.

In section 2.2.1, we characterized the attenuation of light by atoms by using the complex index of refraction, and found that atomic absorption is proportional to the imaginary part of  $n$ , a Lorentzian profile of width  $\Gamma$  which we take to be the natural line width. However, we observe the total absorption of many atoms, so the absorption at any particular laser frequency,  $\omega$ , is due to any atoms that have any part of their

Lorentzian absorption profile (Doppler) shifted onto resonance. To describe this effect, we must use a convolution integral.

$$n(\omega) \propto \frac{1}{(\omega - \omega_0) + i\Gamma/2} \rightarrow n(\omega) \propto \frac{1}{\Delta\sqrt{\pi}} \int_{-\infty}^{\infty} \frac{e^{-(\omega' - \omega_0)^2/\Delta^2}}{(\omega - \omega') + i\Gamma/2} d\omega' \quad (2.17)$$

Or in terms of the absorption,

$$\delta(\omega) = \frac{\alpha_0}{2} \frac{\Gamma^2/4}{(\omega_0 - \omega)^2 + \Gamma^2/4} \rightarrow \delta(\omega) = \int_{-\infty}^{\infty} \frac{\alpha_0}{2} \frac{\Gamma^2/4}{(\omega - \omega')^2 + \Gamma^2/4} e^{-\frac{(\omega_0 - \omega')^2}{\Delta^2} \log 2} d\omega'. \quad (2.18)$$

If instead of considering the combined effect of Doppler broadening on the natural line width, we wished to consider the convolution of two homogeneous mechanisms, we would have a convolution between two Lorentzian absorption profiles, of width  $\Gamma_1$  and  $\Gamma_2$ . It is easy to show that the combined absorption profile is also a Lorentzian of width  $\Gamma = \Gamma_1 + \Gamma_2$  [36]. Therefore, we can simply add all of the homogeneous line widths together, so

$$\Gamma = \Gamma_{nat} + \Gamma_l + \Gamma_p + \Gamma_t + \Gamma_{P.B.} \quad (2.19)$$

This combined Lorentzian of width  $\Gamma$ , then, is convoluted with the Gaussian of width  $\Delta$  to obtain our final line shape.

The convolution of a Lorentzian and a Gaussian in Eq. (2.18) is called a Voigt profile. It is a non-analytic function that turns out to be quite computationally expensive to evaluate. Rather than performing brute force numerical integrals whenever the need to evaluate a Voigt profile arises (it happens more frequently than you might imagine!), we will spend some effort here to arrive at a method of approximating the Voigt profile that is considerably more efficient.

Before embarking on this project, though, we will pause for a moment to reflect upon the total line width in the vapor cell and atomic beam. The 1.4 GHz Doppler width in the vapor cell completely dominates all other sources of broadening to such an extent that the other sources of broadening do not have a significant effect. In other words, to a good approximation, the atoms in the vapor cell have a negligible natural line width. In the atomic beam, however, the 70 MHz Doppler width and 23 MHz combined Lorentzian width are combined into an 83 MHz wide Voigt profile.<sup>1</sup>

Given the difficulty of quickly evaluating the Voigt profile, as in [1], we exploit the subtle relations between the Voigt index of refraction, Eq. (2.17), and the complex error function as given by [37]. The result is that if we let

$$z(\omega) \equiv \frac{\Gamma}{\Delta} - i \frac{\omega - \omega_0}{\Delta} \quad (2.20)$$

$$w(z) \equiv e^{-z^2(\omega)} \operatorname{erfc}(-iz(\omega)), \quad (2.21)$$

where  $\operatorname{erfc}(z) = 1 - \operatorname{erf}(z)$ , then the Voigt absorption and dispersion are easily defined as the real and imaginary part of  $w$ , respectively.

$$\delta(\omega) = \Re\{w[z(\omega)]\} \quad (2.22)$$

---

<sup>1</sup>Recall that these widths are all full-widths at half-maximum.

$$\phi(\omega) = \Im\{w[z(\omega)]\} \quad (2.23)$$

Now the difficulty of calculating the Voigt profile has been reduced to the difficulty of evaluating the complex error function, a function that is much better understood due to its numerous applications. The complex error function is still a non-analytic function and still relatively slow to evaluate, so from here we use the Chiarella-Reichel algorithm. As explained in [1, 38], a great deal of mathematics involving the theorem of residues takes us from Eqs. (2.22) and (2.23) to

$$\delta(z(\omega)) + i\phi(z(\omega)) \approx \frac{ha}{z(\omega)} + \frac{\sqrt{\pi} 2a e^{z^2(\omega)}}{1 - e^{2\pi z(\omega)/h}} + \frac{2haz(\omega)}{\sqrt{\pi}} \sum_{n=1}^N \frac{e^{-n^2 h^2}}{n^2 h^2 + z^2(\omega)} \quad (2.24)$$

where  $h$  and  $N$  are arbitrary parameters that must be adjusted to optimize the convergence of the series to the Voigt profile. We find that choosing  $h = 0.8$  and  $N = 100$  provides sufficiently fast yet reliable convergence. While this certainly looks messier than Eqs. (2.22) and (2.23), this expression gives both the absorption and dispersion of the Voigt profile in terms of only elementary functions.

# Chapter 3

## FM Spectroscopy and Line Shapes

Frequency modulation spectroscopy is a well-established method of signal detection when high sensitivity and signal-to-noise ratio are required [39–41]. We modulate the laser frequency so that the transmitted laser intensity varies at the modulation frequency. Then, frequency sensitive detection via an RF lock-in amplifier (SRS-SR844) picks out only that portion of the transmitted signal that varies at the modulation frequency. All un-modulated light is not modulated and so is rejected by the frequency-sensitive filtering. This removes the background offset. Since it is easier to resolve a small signal  $\epsilon$  from 0 than it is to resolve  $1 - \epsilon$  from 1, this is very beneficial. Also, since most noise is low frequency, the vast majority of noise oscillates away from the reference frequency of the lock-in amplifier, and so most noise is removed from the signal. With a narrow bandwidth amplifier, we can detect small but very well resolved signals even though the density of atoms in our atomic beam is too low to see any direct absorption.

### 3.1 Single Tone Modulation

While there are many methods of FM modulation, we have employed single-tone modulation using an electro-optic modulator (EOM, New Focus 4001) and a radio frequency (RF) lock-in amplifier. Without FM modulation, the electric field of the laser at a particular point is modeled by

$$\tilde{E}(t) = E_0 e^{i(\omega_c t + \phi)} \quad (3.1)$$

where  $\omega_c$  is the carrier frequency of the laser, which, for an optical transition like ours, is in the tens of terahertz range. The addition of frequency modulation with an EOM changes the phase from a constant,  $\phi$ , to a function oscillating at the modulation frequency, which for us is in the RF range,  $\omega_m = 100$  MHz. This changes the electric field to

$$\tilde{E}(t) = E_0 e^{i(\omega_c t + \beta \sin(\omega_m t))} \quad (3.2)$$

where  $\beta$  is the modulation depth, which characterizes the strength of modulation.<sup>1</sup> At this point, either divine inspiration or previous experience with FM spectroscopy motivates the use of the Jacobi-Anger relationship, which re-expresses Eq. (3.2) as the much more informative sum of frequency sidebands at integer multiples of the modulation frequency away from the carrier frequency. As it turns out, the amplitude of each side band is given by various Bessel functions, which are otherwise related to solutions of differential equations in cylindrically symmetric regions.

$$\begin{aligned}\tilde{E}(t) &= E_0 e^{i\omega_c t} \sum_{n=-\infty}^{\infty} J_n(\beta) e^{in\omega_m t} \\ &= E_0 \sum_{n=-\infty}^{\infty} J_n(\beta) e^{i(\omega_c + n\omega_m)t}\end{aligned}\quad (3.3)$$

See Fig. 3.2 for a spectrum of a frequency modulated laser. Since our modulation frequency is  $\omega_m = 100$  MHz, the laser spectrum has a series of peaks each offset by an integer multiple of 100 MHz from the carrier frequency. Given the great importance of the Fabry-Pérot signal to our signal analysis, we address the effect of a frequency modulated laser incident on a Fabry-Pérot interferometer. While unsurprising, it is shown in Appendix C that the output of a Fabry-Pérot interferometer is simply a sum of Airy functions centered at each frequency component of the laser with amplitudes given by the power at the respective frequencies. Therefore, given the high finesse of our optical cavity, the Fabry-Pérot effectively provides a frequency spectrum.

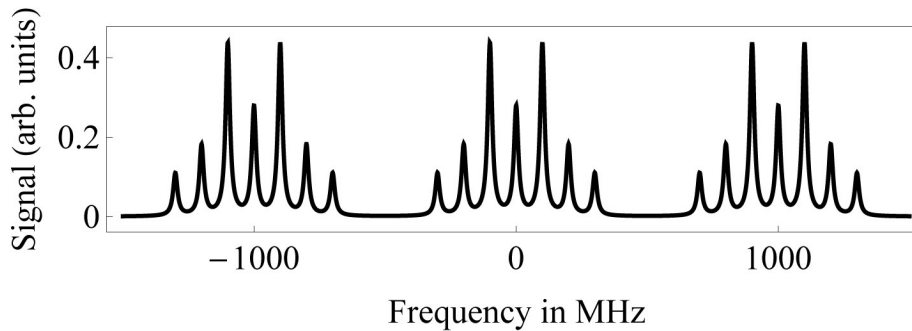


Figure 3.1: A simulated Fabry-Pérot scan of a 100 MHz frequency modulated laser. Our Fabry-Pérot has a free spectral range of 1 GHz. Each set of seven peaks corresponds to a longitudinal mode of the cavity.

Now, we send the frequency modulated laser through a sample of atoms. The electric field picks up the frequency dependent transmission function,  $T(\omega)$ . The

<sup>1</sup>Technically, this is phase modulation. True *frequency* modulation would be  $\tilde{E}(t) = E_0 e^{i((\omega_c + \beta_f \cos(\omega_m t))t + \phi)}$ , but as is shown in [42], this is equivalent to Eq. (3.2) up to a constant, and thus irrelevant, phase offset. Phase modulation and true frequency modulation are therefore equivalent, and are both referred to as FM modulation.

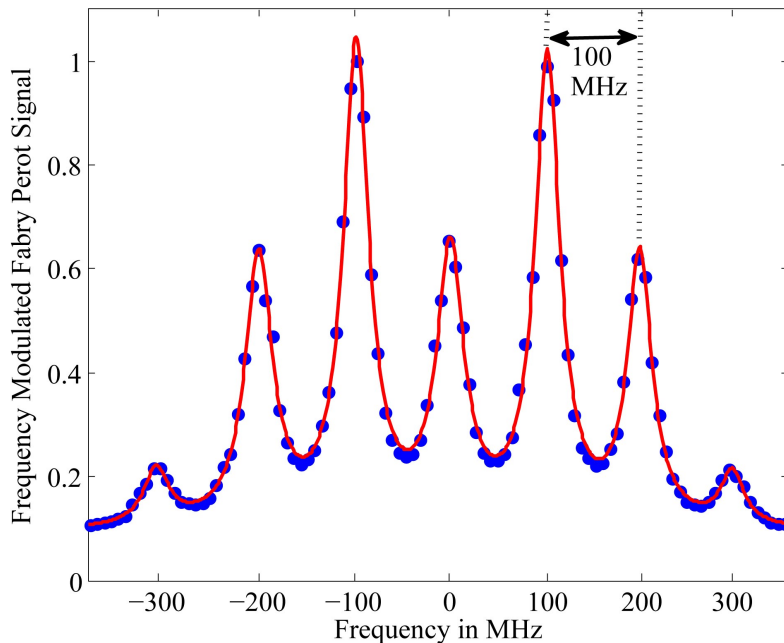


Figure 3.2: A experimental Fabry-Pérot transmission spectrum of an  $\omega_m = 100$  MHz frequency modulated laser at moderate modulation depth ( $\beta \simeq 2$ ). The unmodulated laser spectrum is just the central peak at 0 MHz. This spectrum was obtained by scanning the laser over a single longitudinal mode of the Fabry-Pérot.

electric field after the interaction is therefore

$$\tilde{E}(t) = E_0 \sum_{n=-\infty}^{\infty} J_n(\beta) T(\omega_c + n\omega_m) e^{i(\omega_c + n\omega_m)t}. \quad (3.4)$$

If we define the following shorthands,

$$J_n \equiv J_n(\beta), \quad T_n \equiv e^{-\delta_n - i\phi_n} \approx 1 - \delta_n - i\phi_n, \quad \delta_n \equiv \delta(\omega_c + n\omega_m), \quad \text{and} \quad \phi_n \equiv \phi(\omega_c + n\omega_m),$$

the electric field of the laser after interacting with atoms is

$$E_T(t) = E_0 e^{i\omega_c t} \sum_{n=-\infty}^{\infty} J_n T_n e^{in\omega_m t}. \quad (3.5)$$

An appropriate photodiode for FM spectroscopy measures the time averaged intensity of light,  $I(t) = \langle E^*(t)E(t) \rangle_\tau$  where the averaging time  $\tau$  is short enough that  $1/\tau \gg \omega_m$ . Thus we use a high-speed photodetector (New Focus Model 1601 High-Speed Photoreciever) that has a bandwidth of 1 GHz. Thus we consider

$$|\tilde{E}_T(t)|^2 = E_0^2 \left( \sum_{n=-\infty}^{\infty} J_n T_n e^{in\omega_m t} \right) \cdot \left( \sum_{l=-\infty}^{\infty} J_l T_l^* e^{-il\omega_m t} \right). \quad (3.6)$$

This product of sums leaves us with a DC term, and terms that oscillate in time at multiples of the modulation frequency  $\omega_m$ . We obtain DC terms if  $l = n$ . In that case

$$\begin{aligned} |\tilde{E}_T(t)|_{DC}^2 &= E_0^2 \sum_{n=-\infty}^{\infty} J_n^2 T_n^* T_n \\ &= E_0^2 \sum_{n=-\infty}^{\infty} J_n^2 e^{-2\delta_n} = E_0^2 \sum_{n=-\infty}^{\infty} J_n^2 (1 - 2\delta_n) \end{aligned} \quad (3.7)$$

This shows that DC absorption is unresolvable above background given our signal to noise ratio since  $\delta_n \sim 10^{-3}$ . Therefore we will look at the oscillating terms.

## 3.2 1f Demodulation

The low modulation depth limit has been explored in many articles and reference works; indeed, the 1f demodulation with  $\beta \ll 1$  is the canonical example of FM spectroscopy. In this limit, the infinite sum in the electric field is replaced by the central carrier plus the two first order sidebands:

$$\tilde{E}_T(t) = E_0 [J_0 T_0 e^{i\omega_c t} + J_1 T_1 e^{i(\omega_c + \omega_m)t} - J_1 T_{-1} e^{i(\omega_c - \omega_m)t}] \quad (3.8)$$

By taking  $I \propto E^* E$  and selecting terms that oscillate at  $\omega_m$ , we isolate the demodulated FM signal,

$$I_{demod} = I_0 J_0 J_1 e^{-2\delta_0} [(\delta_{-1} - \delta_1) \cos(\theta_d) - (\phi_1 + \phi_{-1} - 2\phi_0) \sin(\theta_d)]. \quad (3.9)$$

Appendix A of Antonio Lorenzo's thesis [43] works through the algebra of this calculation. We wish to move on, though, to the moderate and high modulation depth regime, as that is where the present experiment resides. Starting with the full transmitted electric field given in Eq. (3.5), in Appendix D we follow [39] to reproduce his result for the portion of FM transmission signal that oscillates at  $1\omega_m$ . This gives us the following for the 1f demodulated signal:

$$\begin{aligned} I_{demod}^{1f}(t) = I_0 e^{-2\delta_0} \sum_{n=0}^{\infty} J_n J_{n+1} \left[ (\delta_{-n} - \delta_n + \delta_{-n-1} - \delta_{n+1}) \cos(\theta_d) + \dots \right. \\ \left. (\phi_{n+1} - \phi_n + \phi_{-n-1} - \phi_{-n}) \sin(\theta_d) \right], \end{aligned} \quad (3.10)$$

where  $\delta_n$  and  $\phi_n$  are the absorptive and dispersive Voigt profiles corresponding to the  $n^{th}$  sideband as produced in Eq. (2.24) and  $\theta_d$  is the demodulation phase angle. We present a few example FM line shapes below (Fig. 3.4). While the complexity of the FM line shape can vary quite a bit, depending primarily on the modulation depth  $\beta$  and the demodulation phase  $\theta_d$ , we successfully fit to the full analytic functional

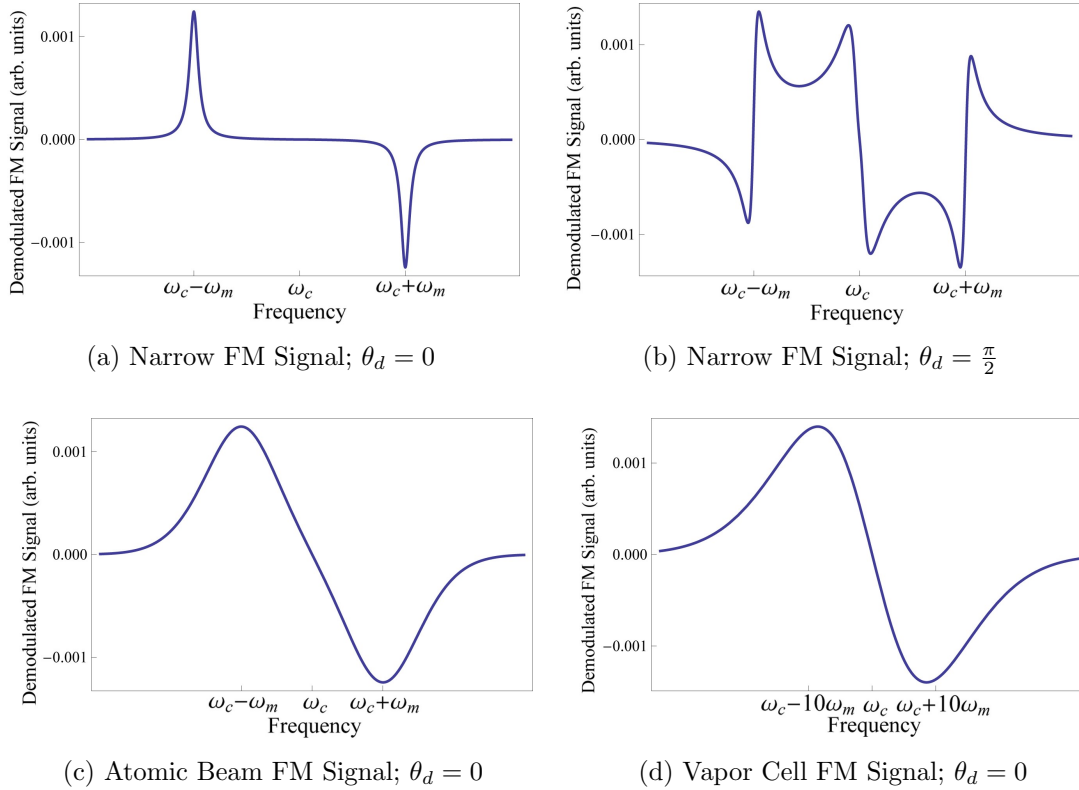


Figure 3.3: A simulation of the demodulated FM signal in the low modulation depth limit. The absorption profile in (a) and (b) is a narrow Lorentzian (with corresponding dispersion profile) as described in 2.2.1. Voigt profiles with realistic atomic beam (c) and vapor cell (d) component widths are used. Note the factor of ten difference in horizontal scales between (c) and (d). The peak and trough are not exactly at  $\omega_c \pm \omega_m$  even in the atomic beam, so the signal is not self-calibrating. Also, note the large linear region between the peak and trough for sufficiently wide absorption widths.

form as given by Eq: (3.10). As a qualitative rule of thumb, the 1f FM signal is the sum of alternating-signed resonance peaks at each of the frequencies of the laser except the carrier. As seen in Fig. 5.4, if the absorption width is much narrower than the modulation frequency ( $\Gamma \ll \omega_m$ ), then each frequency component of the laser independently ‘sees’ the resonance as the laser is scanned, so the absorption signal is a sequence of individual peaks and troughs. If the absorption width is much broader than the modulation frequency ( $\Gamma \gg \omega_m$ ), then all frequency components ‘see’ the absorption simultaneously. This washes out the complex structure of the transmitted signal, so that the demodulated signal looks like a wide dispersion profile. The present experiment lies between these two regimes ( $\Gamma \approx \omega_m$ ), in which the component features overlap to create a complex transmitted signal that must be treated in its full analytic form.

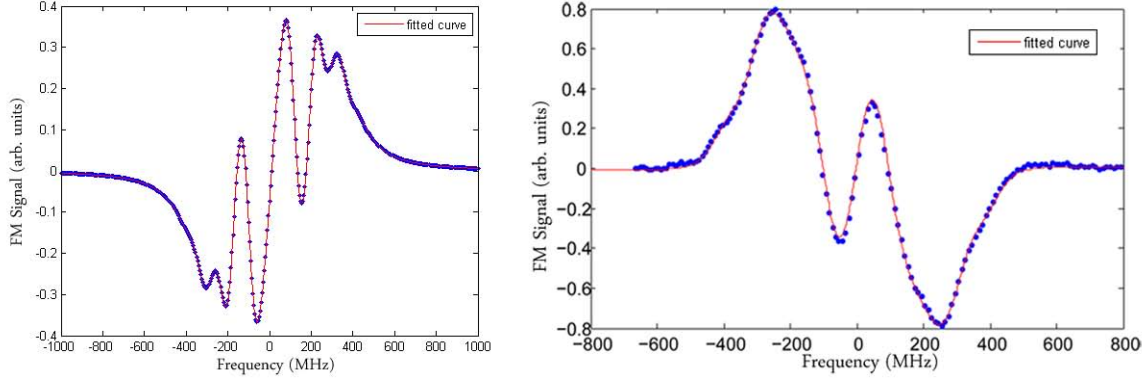


Figure 3.4: Two representative 1f FM signals. The points represent data taken, and the curve is the result of a non-linear least-squares fit to that data using Eq. (3.10)

### 3.3 2f Demodulation

1f demodulation is the standard form used in FM spectroscopy. However, it is also valuable to look at the signal demodulated at *twice* the reference frequency. It is easy to implement demodulation at  $2\omega_m$ , since our lock-in amplifier simply includes this as a feature, and the very distinct line shape features of the 2f signal serve as a powerful systematic error check. 2f FM spectroscopy is not nearly as frequently implemented as 1f spectroscopy, so the resulting demodulated line shape is not found in the literature except in the low modulation depth limit. Since we are certainly far from this limit ( $\beta \sim 2$ ), it is necessary to derive the analytic form of the demodulated signal ourselves.

We recall Eq. (3.6) which told us that the intensity of the laser field after passing through the atoms is a product of two infinite sums, a product which contains components that oscillate with angular frequency  $n\omega_m$ ;  $n = 0, 1, 2, \dots$ . In the previous section, we considered what the output of a lock-in amplifier would be if it took the modulation frequency as its reference frequency. We now consider the form of the output of the lock-in amplifier which takes twice the modulation frequency as its reference. Thus, we consider terms that oscillate at  $2\omega_m$  in Eq. (3.6). For the more algebraically masochistic among you, the full derivation is available in Appendix D. Otherwise, we quote the result.

$$\begin{aligned}
 I_{demod}^{2f} = I_0 & \left[ \left( -J_1^2(1 + 2\delta_0 - \delta_1 - \delta_{-1}) + \dots \right. \right. \\
 & \left. \left. \sum_{n=0}^{\infty} J_n J_{n+2} (2 + 4\delta_0 - \delta_n - \delta_{-n} - \delta_{n+2} - \delta_{-n-2}) \right) \cos(\theta_d) + \dots \right. \\
 & \left. \left( -J_1^2(\phi_1 - \phi_{-1}) + \sum_{n=0}^{\infty} J_n J_{n+2} (\phi_{-n} - \phi_n + \phi_{n+2} - \phi_{-n-2}) \right) \sin(\theta_d) \right] \quad (3.11)
 \end{aligned}$$

This result is quite similar, at least in feel, to the 1f result. From the signs of the component profiles for  $\theta_d = 0$ , it is evident that the signal is symmetric about the line center. Below, we have included two 2f FM signals fit with the full analytic profile as derived above.

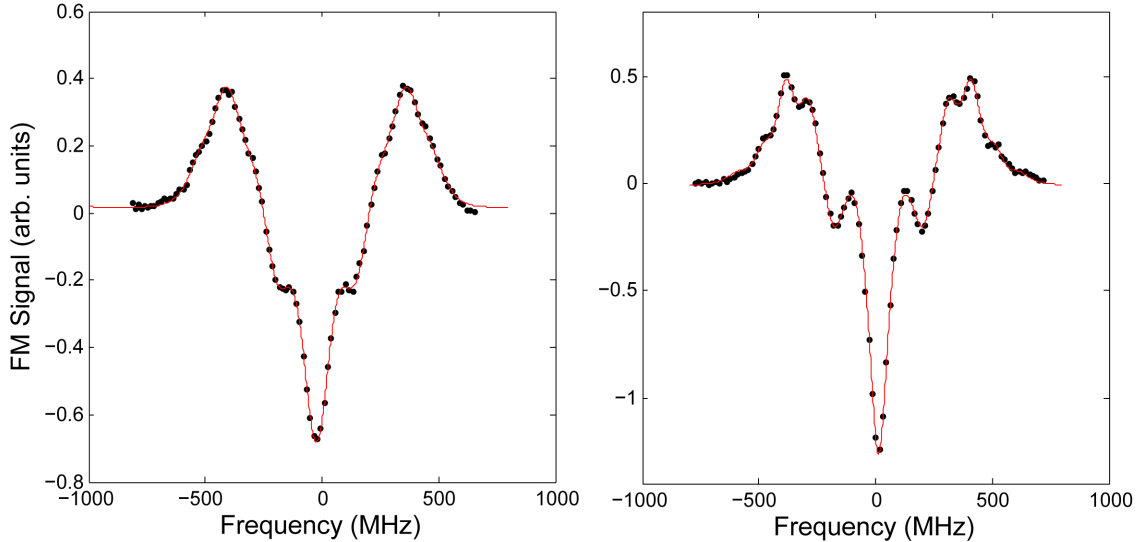


Figure 3.5: Two representative 2f FM signals fit using the full analytic form given by Eq. (3.11).

We have now presented the full analytic form of the FM signals that we recorded and from which we extracted our Stark shift measurements. At this point, it is worth recalling that each  $\delta$  and  $\phi$  are themselves Voigt absorption and dispersion profiles. In order to fit these line shapes analytically, we must implement a non-linear least-squares algorithm which calculates these line shapes throughout a sizable region of parameter space and which subsequently minimizes the  $\chi^2$  figure of merit. Therefore, we are calculating *many* Voigt profiles, justifying our efforts in implementing the Chiarella-Reichel algorithm (see Eq. 2.24).

### 3.4 Complications to the Observed FM Lineshape

Despite the general robustness of frequency modulation spectroscopy, there are several potential routes for error or noise to enter the system. For instance, noise in the input current of the laser causes noise in both the intensity and frequency of the laser. Since substantially none of this noise will lie within the high-frequency narrow bandwidth of the RF lock-in referenced to  $\omega_m$  or  $2\omega_m$ , the amplitude noise will be filtered out effectively. Low frequency instability in the laser frequency, however, can propagate through. Our commercial laser diode controllers effectively eliminate this potential source of instability. Several other mechanisms also remain by which our signal could be other than predicted by Eq. (3.10) or Eq. (3.11).

### Residual Amplitude Modulation

All phase modulators such as our EOM cause some residual amplitude modulation at  $\omega_m$  in addition to their primary frequency modulation. The AM adds additional positive frequency sidebands at  $\omega_c \pm \omega_m$ . Since the FM has a positive frequency sideband at  $\omega_c + \omega_m$  and a negative frequency sideband at  $\omega_c - \omega_m$ , a small additional AM causes an imbalance in the magnitude of the two first order sidebands. This results in a non-ideal FM signal in that certain component profiles have altered amplitudes. More importantly, though, the AM modulation is directly proportional to the input laser power. Therefore, while laser power noise is filtered out of the ideal FM signal, it may become manifest as noise in the additional AM component [41]. This is but another reason why very stable laser diode controllers are a requirement for our experiment. Due to the high quality of our EOM and laser diode controller, we do not resolve any residual amplitude modulation (see Fig. 3.6).

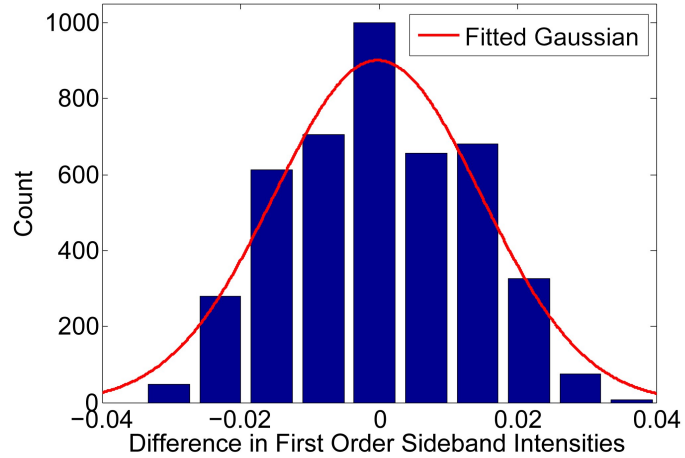


Figure 3.6: A histogram of the moving difference between the first order sidebands. The average value for the difference is  $-0.00001(1320)$ .

### Incomplete Modulation by the EOM

While we model the laser field after being frequency modulated by the EOM as Eq. (3.3), this is an idealization. We find deviations from the ideal laser spectrum through our Fabry-Pérot scans. We expect the peak height of the  $n^{\text{th}}$  sideband in the laser spectrum to be proportional to  $n^{\text{th}}$  Bessel function squared of the modulation depth. In particular, this means that each frequency component should go to zero for a particular modulation depth. However, as we scan the input RF power of the EOM and thus scan the modulation depth of the frequency modulation, we do not extinguish the principle carrier frequency. We explored models and causes of this deviation from ideal modulation; a discussion of this may be found in Appendix E. Our analysis is consistent with two possible causes: either our EOM is leaving approximately 2% of the laser power unmodulated, or there is a spatially dependent modulation in which the modulation depth depends on the path of the laser through the electro-optic crystal. The former does not cause a problem in the Stark shift measurement, as it changes the amplitudes of the components of the FM signal in a non-frequency dependent way. The latter is more problematic and is discussed presently.

### **Spatially Dependent Modulation**

If we do have a spatially dependent modulation depth, we have a further risk for noise to enter our signal. We can characterize the effective modulation depth of the transmitted FM laser field as the result of the integration of the spatially dependent modulation strength of the EOM times the spatially dependent power profile of the laser beam. The trouble arises because the alignment of the laser does vary slightly as the laser is scanned due to the change in the angle of the diffraction grating that is part of the laser cavity and whose tilt angle is varied to tune to the laser frequency. If we have a spatially dependent EOM modulation strength, the frequency dependent alignment of the laser through the EOM results in a frequency dependent effective modulation depth. Given the complicated dependence of the demodulated FM signal on the modulation depth of the laser, this source of error cannot easily be accounted for in our computer fitting and analysis programs and could certainly be the source of the irregular oscillatory background that our once-demodulated FM signal reveals.

### **Etaloning Within EOM**

Furthermore, although the faces of our EOM are anti-reflection coated, there may be some internal reflections within the EOM. This results in a multiple reflection etalon-like effect, in which the laser power inside the EOM is laser-frequency dependent and very likely non-reproducible. Furthermore, the beam path through the EOM changes as the piezo-electric transducer (PZT) scans the frequency of the laser, so the overall magnitude of the etaloning effect may vary with frequency as well. The good news is that due to the anti-reflection coatings, this effect is very small, i.e. the finesse of the etalon very small. Thus, the power fluctuations would be approximately sinusoidal rather than sharply peaked. Note that the FM spectroscopy technique does nothing to remove this effect, as this is variation in the modulation depth of the FM as a function of frequency. Such etaloning within the EOM likely contributes to the time varying sinusoidal background mentioned in the previous section.

We effectively eliminate these last two effects by implementing our dual-modulation scheme. We modulate the atomic beam at several hundred hertz by means of an in-vacuum chopper wheel and demodulate the once-demodulated FM signal again at this relatively low second modulation frequency. The optical effects discussed above are certainly independent of this beam chopping and so are removed.



# Chapter 4

## Experimental Apparatus

The experimental apparatus has not changed in a major way since the previous theses on this measurement. Therefore, we offer a brief overview of the experimental apparatus and refer the interested reader to [43, 44] for additional discussion.

### 4.1 Atomic Beam Apparatus

As discussed in 1.2.1, the Stark effect is manifest as a 10-50 MHz shift in the transmitted signal depending on the voltage applied. We wish to measure this shift to less than 1% uncertainty, requiring the FM signal to have a combination of narrow spectral features with a high signal-to-noise ratio. However, as discussed in 3.2, the spectral features of the FM signal will spread in frequency as the Doppler width increases. Without any effort to reduce the Doppler width, we therefore will have FM signals that are much too broad to resolve the Stark shift with high precision. We probe indium atoms in a well-collimated atomic beam to reduce the Doppler width of the atoms' resonance profile. Our atomic beam apparatus produces this atomic beam and so is of critical importance to the experimental design.

Because of the need for both high temperatures and accurate electric field determination, the entire atomic beam apparatus is kept under vacuum. Beneath both the source and interaction chambers, we have installed a diffusion pump and a liquid nitrogen trap to condense and remove residual gas. The entire system is capable of achieving pressures below  $10^{-7}$  torr. While operating the atomic beam, the pressure equilibrates closer to  $10^{-6}$  torr, under which conditions the mean free path of the residual gas is several tens to hundreds of meters. Therefore, we can ignore possible effects of atomic beam collisions with the background gas.

#### 4.1.1 Atomic Beam Source

A homebuilt oven heats  $\sim 100$  grams of indium pellets to  $900^\circ\text{C}$  inside of a blind bore molybdenum crucible. This crucible tilts upwards to keep liquid indium contained inside, while the heated indium produces a vapor that effuses out of the crucible. The

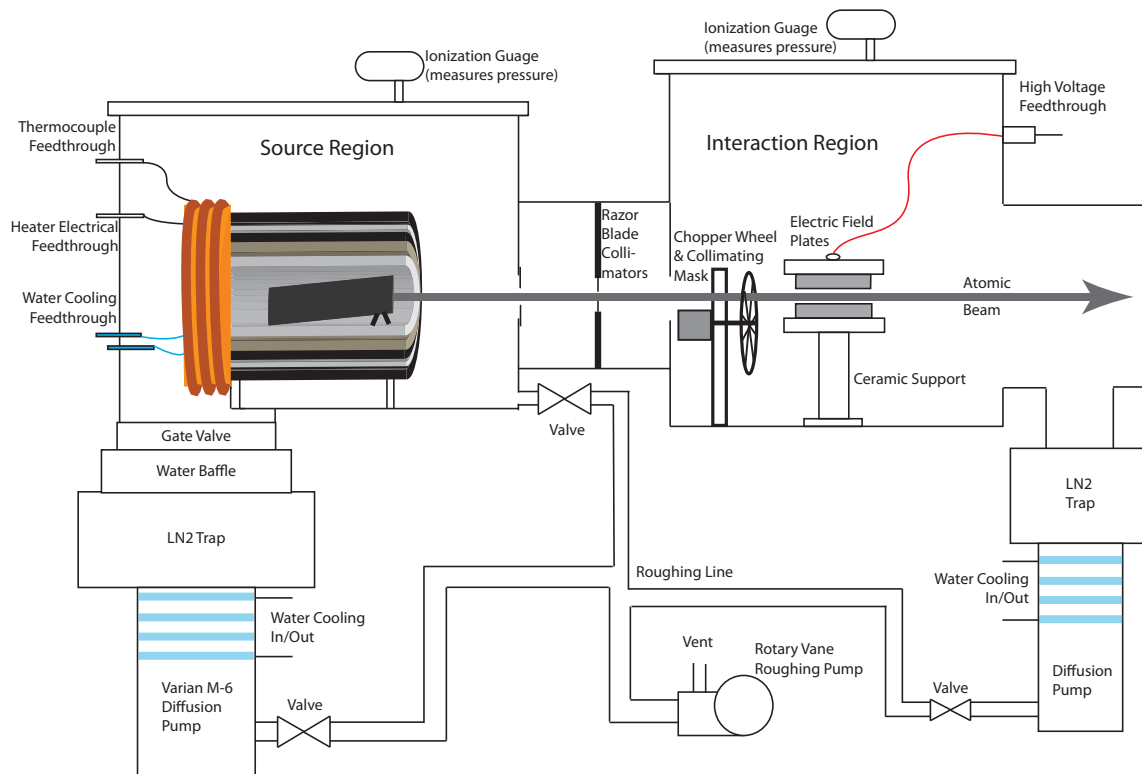
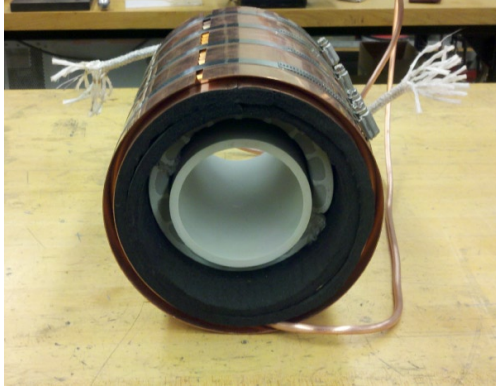


Figure 4.1: A diagram of the atomic beam apparatus showing the source and interaction regions along with the vacuum system.

crucible face is milled to vertical so that the exiting indium vapor travels horizontally. To provide initial transverse collimation of the atomic beam, a molybdenum faceplate with 20 parallel 0.25 mm slits attaches to the front of the crucible. The crucible sits atop a ceramic tube that spreads and evens the heat delivered by a home-built ceramic clamshell heater. Layers of carbon felt insulation and stainless steel sheet around the ceramic heater trap and reflect heat, allowing the system to reach higher temperatures for a given input power. These layers along with an outer water-cooled copper cold wall also protect the rest of the system from the high temperatures. For more information on the source, please see [43, 44].

### 4.1.2 Collimation and Interaction

Primary collimation of the beam is provided by geometry, which therefore requires the interaction region to be spatially far from the source. Adjustable razor blades placed 20 cm away from the crucible faceplate mask all atoms except those effusing sufficiently straight out from the source, and they define the atomic beam to be 2 mm x 1.5 cm in cross section. Sharp razor blades are used to minimize scattering off of the edges of the collimator. Between the razor blade collimators and the interaction



(a) Oven Assembly



(b) Crucible

Figure 4.2: Photos of the assembled oven (a) and the molybdenum blind bore crucible with its faceplate (b). The elements, from inside to outside, that make up the oven are the crucible, ceramic tube, clamshell heater, carbon felt, stainless steel sheet, carbon felt, water-cooled copper cold wall.

region another 20 cm further downstream, we insert a final atomic beam mask to block any scattered atoms and a chopping wheel with an in-vacuum motor. This provides the second, low-frequency modulation in our dual modulation scheme. The atoms are modulated at  $\sim 500$  Hz, and a second signal demodulation at this frequency helps remove systematic errors from the optical setup, particularly in suspected frequency dependent modulation of the laser by the EOM (see section 3.4).

The interaction region is defined as the transverse intersection of the 410 nm FM laser beam with the atomic beam. The laser beam enters and exits the interaction chamber through two anti-reflection coated windows and passes between two highly polished stainless steel plates separated by ceramic standoffs. Metric gauge blocks and three adjustable bolt-and-nut height adjustments are used to parallelize the field plates and set their separation to 0.999(1) cm across the interaction region. Our high voltage supply (Glassman High Voltage, Inc. Model PS/ER40P07.5XX0) can produce voltages up to 40 kV. The output of the supply enters the interaction chamber via a fragile high voltage feedthrough and is attached to the top field plate. Thus, we produce an electric field in the interaction region,

$$\vec{E} = -\frac{V}{d}\hat{z}. \quad (4.1)$$

In the event of arcing (catastrophic failure) across the field plates, we limit the current flow to the milliamperage range by means of a 100 M $\Omega$  series of ballast resistors in series with the field plates. While ideally no current flows through the gap between the field plates, very small ion currents grow as indium metal builds up on the field plate surfaces. There is also always a small additional current ( $\sim 10$  nA) associated with the  $10^{12}$   $\Omega$  resistance of the ceramic spacers. We monitor the combined ‘leakage’ current with a voltmeter across another 10.68 M $\Omega$  resistor. A dramatic spike in the

leakage current is a sign of either a dangerous pressure spike or excessive buildup of indium on the field plates; in either case, immediate shut-down of the high-voltage system is required. We also choose to limit the voltage output to 20 kV; if we approach 30 kV or above, we can experience field plate discharges. Such high voltage flowing to ground can elevate the electric potential of that ground (since no ground is perfect) and thereby create a ground loop. This is quite dangerous to anything, human or electronic, that encounters it. For proof, we simply look to the electronics reset or destroyed as current passed backwards from ‘ground’ into the equipment. To avoid this, we vary the voltage only up to 20 kV.

Finally, we must also precisely measure the output of the high voltage supply. In parallel with the supply, we attach a Ross Engineering high voltage divider, which consists of 1000 precisely matched resistors that divide the input voltage by a factor of 1000 to 0.01%. An impedance-matched and calibrated microvolt precision voltmeter (Keithley 197A) then provides a high precision measurement of the output high voltage. Simple DC circuit equations then provide the actual voltage across the field plates.

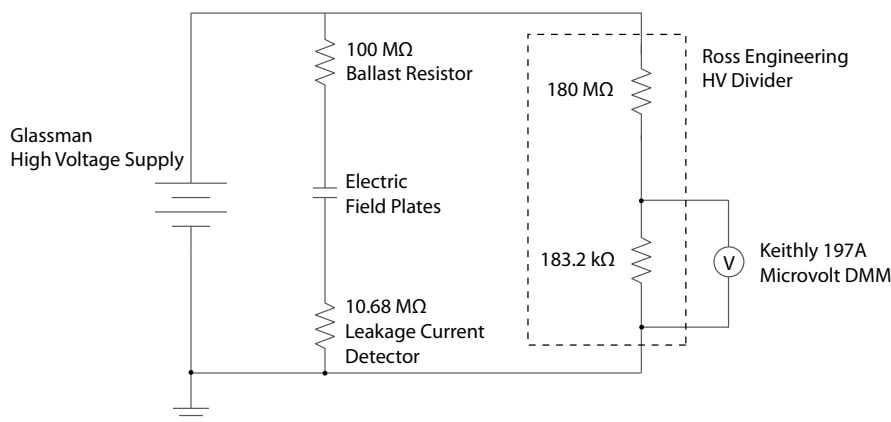


Figure 4.3: A circuit diagram of the high voltage system.

The above uncertainty in the field plate separation turns out to be the limiting uncertainty in this experiment (see Table 5.2). We calculate the uncertainty in the electric field as  $\delta E = \sqrt{\delta V^2 + \delta d^2}$ , where the deltas denote *fractional* uncertainties. Since we measure the voltage to an order of magnitude better precision than the 0.1% uncertainty of the field plate separation  $d$ ,  $\delta E = 0.001$ . Recalling section 1.2.1, the Stark shift constant,  $k_S = \frac{\Delta\nu_S}{E^2}$ , is derived from the square of the electric field, so the fractional uncertainty of  $k_S$  is given by  $\delta k_S = \sqrt{\delta\nu_S^2 + 2\delta E^2}$ . Thus, the electric field uncertainty corresponds to a 0.2% uncertainty in  $k_S$ . Since every measurement was taken with the same field plate configuration, this error is entirely non-statistical, and so must be added in as a systematic error. We measured the field plate parallelization and separation both before and after taking data, so we are confident in this assignment of error.

## 4.2 Optical System

To probe the  $5P_{1/2} \rightarrow 6S_{1/2}$  atomic transition in indium, we use a 410 nm Toptica DL 100 diode laser in the Littrow external cavity configuration. We tune the laser to excite one of the two hyperfine levels of this transition, modulate the laser frequency, and send it transversely through the in-vacuum atomic beam. A 1 GHz bandwidth high speed photodetector (New Focus Model 1601 High-Speed Photoreceiver) collects the transmitted laser light for recording and analysis. Fabry-Pérot interferometry and saturated absorption spectroscopy are employed for frequency linearization and calibration, respectively. See Fig. 4.4 for the full optical setup used in the present work.

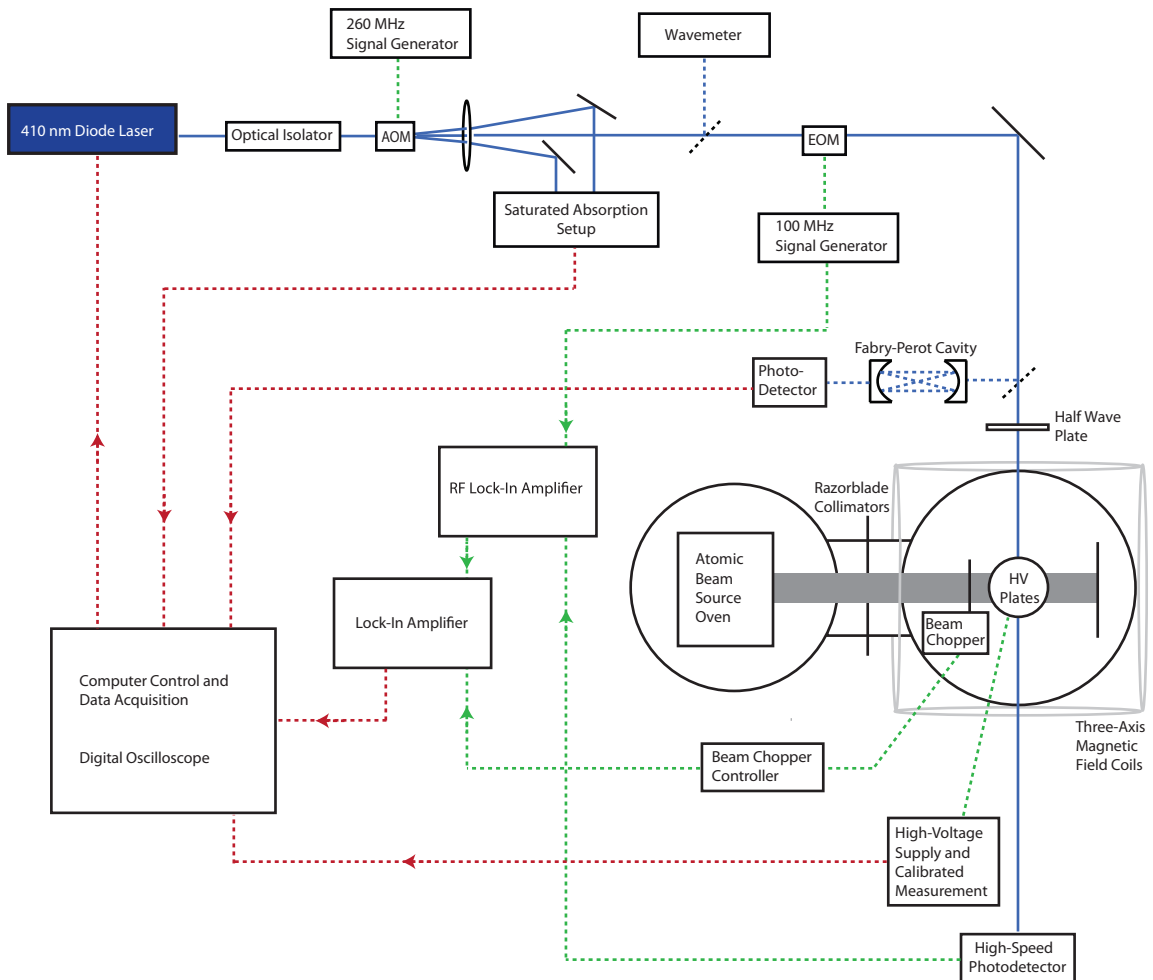


Figure 4.4: The experimental setup used in the present work.

### 4.2.1 Diode Laser

A GaN semiconductor diode in the Littrow configuration produces the laser light used in this experiment. The laser produces light over a relatively broad range of frequencies that is quickly captured and directed by a collimating lens to a diffraction grating. This grating reflects most of the light like a mirror, but diffracts a portion of the light by an angle that depends on the frequency of that light. By adjusting the diffraction grating so that this first order diffraction counter-propagates back into the laser diode, we form an external cavity, in which the returning light causes lasing to occur predominately at the same frequency. However, only a very narrow range of frequencies diffracts by the exact angle necessary to re-enter the semiconductor, so the laser in this configuration lases at a precise frequency. This frequency is then controlled by carefully tilting the grating which selects for a different frequency. A piezo-electric transducer (PZT) is placed behind the grating support so that a voltage ramp across the PZT corresponds to a frequency scan of the laser. Use of the laser then necessitates two steps:

1. adjustment of grating angle, temperature, and laser current to produce single mode and stable lasing over several gigahertz around the atomic transition, and
2. conversion between the PZT ramp voltage and the actual instantaneous frequency of the laser.

We frequency-stabilize the laser through a variety of passive systems; active frequency locking proves unnecessary. We use power stabilized laser diode controllers to limit power fluctuations to the laser and place the laser inside an acoustic foam lined box to minimize temperature fluctuations. The heavy optical table and sub-basement location of the lab help reduce mechanical noise. Since we do not lock the frequency of the laser—after all, we are scanning the laser across the atomic resonance—we do find that over the course of a few minutes, the laser drifts ten or twenty megahertz. Our scans take two seconds however, so any effects from this slow drift are minimized. The dominant source of laser noise is a constant high frequency jitter of order 1 MHz as displayed in Table 2.1. No matter the kind, we constantly monitor laser frequency fluctuations with the simultaneous Fabry-Pérot transmission spectra.

Single mode lasing, as distinguished from multi-mode lasing, refers to a laser in which only one frequency is produced. The external cavity laser, like a Fabry-Pérot interferometer, is resonant at many frequencies that are separated by constant frequency. It is possible—and indeed very common—that, because of imprecise alignment and unfortunate choice of laser current, several modes of the laser are excited simultaneously.

### 4.2.2 Laser Control and Frequency Monitoring

There is a well developed art to adjusting diode lasers into single mode operation. Coarse adjustment of the diffraction grating, both vertical and horizontal, is required

to bring the laser to the approximately correct frequency. A combination of the three primary parameters (temperature, current, and voltage) then must be employed. Temperature is the only predictive parameter, by which we mean that the result of adjusting the other two is largely random. Increasing the temperature lengthens the cavity and therefore lowers the frequency of the output light; the inverse also holds. Current and voltage are best reserved for removing multi-mode behavior. A reader might be wondering at this point how we determine the frequency of the laser while it is far from the atomic resonance as well as how we observe multi-mode behavior.

To find the frequency of the laser, we utilize a commercial seven digit wavemeter (Burleigh WA-1500). This device, a scanning Michaelson interferometer, compares the fringe spacing of the input laser to those of a stabilized reference HeNe laser. The ratio of peak spacings is the ratio in frequencies, so the input laser frequency is thus determined. We can then use this device to bring the laser close to the atomic resonance. However, if the laser outputs multiple frequencies, the wavemeter analyzes only the most powerful and tends to jump between various frequencies. To remove such multi-mode behavior, we look at power spectra.

A Burleigh RC 110IR Fabry-Pérot interferometer provides these power spectra. As discussed in section 3.1 and developed in appendix C, the output of the Fabry-Pérot will produce a repeating profile of the intensity spectrum of the laser beam given arbitrary frequency inputs.<sup>1</sup> Single mode operation of the laser (not frequency modulated) should produce a classic Airy function; additional frequency components appear as additional Airy functions of arbitrary amplitude. We use the laser current and voltage adjustments to optimize the Fabry-Pérot output to be exactly a single Airy function.

One might think that the conversion between PZT ramp voltage and laser frequency would be trivial. However, the expansion of the PZT is distinctly non-linear and hysteretic. Despite the difficulty of doing so, we must convert back to frequency for every scan. As will be developed in section 5.1.2, the Fabry-Pérot signal is used to undo this frequency axis non-linearity. A saturated absorption setup using a separate indium vapor cell further provides a frequency reference point, protecting against long-term drifts in either the laser frequency or the Fabry-Pérot cavity. A detailed discussion of the theory and implementation of saturated absorption spectroscopy is given in appendix F. Therefore, it is sufficient to note that saturated absorption spectroscopy provides a Doppler-narrowed transmission peak located at the resonant frequency. As it is derived from atoms under non-changing conditions, this signal serves as an ideal reference from which to define shifts in frequency.

---

<sup>1</sup>Technically, this only holds as long as the reflectivity of the mirrors is constant. As a practical matter, this is always true, and even if it were not, we need only see the appearance of other modes. We do not care about the exact relative amplitudes.

### 4.2.3 FM Implementation and Prerecording Signal Analysis

We perform basic manipulations to relevant signals before recording them for fitting and analysis. As discussed in appendix F, the saturated absorption setup directs the photodiode voltage to a lock-in amplifier (300  $\mu$ s time constant) to reveal the Doppler narrowed peak.

As introduced in section 3.1, we frequency modulate the laser by means of a New Focus 4001 EOM. A very stable 100 MHz signal, between -8 and -3 dBm in power, is produced by a Hewlett-Packard 8656B Signal Generator. This signal is amplified to 1000x greater power by a Mini-Circuits ZHL-03-5WF High Power Amplifier. Thus, the EOM input RF power ranges from -8 to -3 dBW, safely below the 1 W = 0 dBW stated maximum RF input power of the EOM. This signal produces the external oscillating electric field necessary for operating the EOM and also provides the reference signal for the first step, RF lock-in amplifier (SRS model SR844). The lock-in demodulates the output of the high-speed photodetector with a sensitivity of 3 mV and no filtering. The output of this lock-in provides the input for the second low frequency lock-in (SRS model SR810) with a time constant of 1 ms, filter rolloff of 24 dB/oct., and sensitivity of 3 mV. This lock in is referenced by the output of the controller (HP E3620A Dual Output DC Power Supply) of the in-vacuum chopping wheel. The output of the second lock-in is then acquired and recorded.

## 4.3 Data Acquisition

We interface between the experimental apparatus and the experimental control and data acquisition computer via a National Instruments data acquisition board (DAQ, NI USB-6221).

From the discussion above, it is clear that we must record three signals simultaneously: the Fabry-Pérot, the saturated absorption, and the demodulated FM signals. This forms one part of our experimental control and data acquisition LABVIEW program. This program

generates a timing sequence for alternating the high voltage and scanning the laser. It then records the three signals mentioned above along with the precise voltage value and data configuration information (see Fig. 4.6). This configuration information is essential for later systematic error searches. We take data in the on-off-off-on ordering so that we can explore possible drifts in the observed Stark shift or possible high voltage state dependent effects.

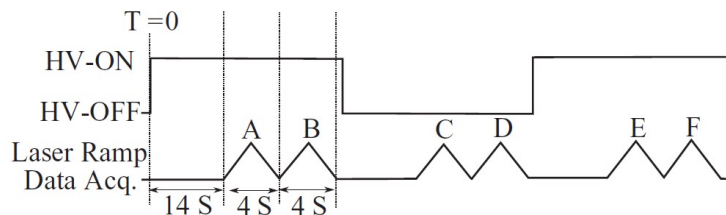


Figure 4.6: A diagram of the timing sequence for experimental control and data acquisition.

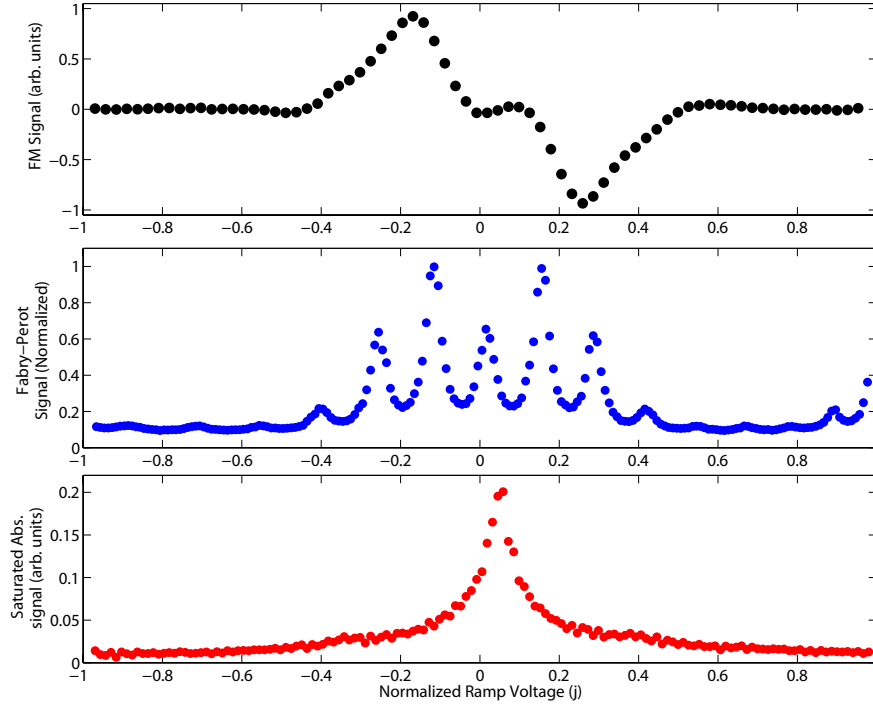


Figure 4.5: A sample scan showing the three simultaneously recorded signals. Note that the horizontal axis is not frequency, but rather corresponds the normalized PZT ramp voltage.

A single data scan takes roughly 2 s, and we take two up-scans and two down-scans per high voltage state. Due to the capacitance of the high voltage system and the requirement of a precise calibration of the electric field, we wait 14 seconds between HV on and HV off scans so that voltage transients may subside. We compute the Stark shift by comparing consecutive same-scan-direction data.<sup>2</sup> Because of the 1 ms time constant used in the FM signal demodulation, we can take data much faster than the system can respond. In order to ensure that all data points are statistically independent so that the determination of fit parameter errors is valid, we use data points that are temporally separated by at least 7 ms. This is accomplished by downsampling the recorded data. Please refer to Paul Hess’ thesis [45] for further discussion of downsampling and the SRS-844 manual for the relevant formulae.

### 4.3.1 Summary of Collected Data

Using the experimental apparatus described above, we recorded approximately 15,000 scans over 22 days resulting in approximately 7,500 Stark shift measurements. Each day, we took either one or two sets of data, and each data set consisted of either

<sup>2</sup>i.e. B-up — C-up; B-down — C-down; D-up — E-up; D-down — E-down; etc.

25 or 50 scans at 11 different voltage values. These nominal values in kilovolts were 10, 11, ..., 19, 20, but we recorded the exact voltages for each scan. Each set of data varied with respect to the numerous experimental parameters (see Table 5.1). As analysis proceeded, we found four days with unfittable data—this was due to equipment breakage<sup>3</sup> or Fabry-Pérot instability. After discarding such data, we were left with 18 days of data corresponding to roughly 6,000 Stark shift measurements. The final statistical uncertainty in our measurements is less than 0.1%. Such high statistical precision enabled us to explore many possible sources of systematic error.

---

<sup>3</sup>In particular, the in-vacuum chopping wheel motor would overheat and fail due to line-of-sight exposure to radiation from the atomic beam source oven. Future experiments of this type would be improved with a better in-vacuum chopping wheel motor assembly design.

# Chapter 5

## Data Analysis

### 5.1 Data Fitting

We explored several different methods to fit the FM signals and thereby extract the Stark shift. We used various approximation methods without fitting to the full line shape as well as implementing full analytic Voigt fits based on Eqs. (3.10) and (3.11) with the sideband amplitudes,<sup>1</sup> lock-in phase, and Voigt profile component widths as fit parameters in a non-linear least-squares fitting program. Significant effort in fitting automation became essential, since a fit of a single data scan takes between 30 seconds and several minutes. Furthermore, we fit every data set twice, once with the full analytic fitting program and once by the relevant polynomial or Lorentzian approximation program. We developed routines for peak finding and sensible initial guesses so that large sets of data could be fit with minimal human intervention. It is worth turning some attention to the guts of our fitting programs, as this elucidates, among other things, the linearization procedure hinted at in section 5.1.1. We begin with the background to this linearization procedure.

#### 5.1.1 Frequency Linearization and Calibration

The Fabry-Pérot interferometer is used to linearize the frequency axis when the laser is frequency modulated. The period of repetition of the Airy function output of our confocal Fabry-Pérot cavity is the free spectral range given by  $FSR = \frac{c}{4d}$ , where  $c$  is the speed of light and  $d$  is the length of the cavity. By choosing our  $FSR$  to be 1 GHz, we ensure that even at high modulation depths (with power out to the third 100 MHz sideband), the successive power spectra from nearby longitudinal modes do not overlap. We use the exact 100 MHz separation of the power spectrum peaks to define a third order polynomial relation  $f(x_j) = a_0 + a_1x_j + a_2x_j^2 + a_3x_j^3$  between

---

<sup>1</sup>This should, in theory, only be the modulation depth, with the the sideband amplitudes determined by the relevant Bessel function of that modulation depth. However, due to effects mentioned in 3.4 and E, the actual sideband amplitudes are not given exactly by Bessel functions. To accommodate this, we simply leave each as an independent fit parameter.

the normalized ramp voltage  $x_j$  and the laser frequency  $f$ . By recording scans of the Fabry-Pérot simultaneously with the demodulated FM transmission signal, we can determine the coefficients of  $f(x_j)$  and apply the function to the FM signal. Variation in the non-linearity parameters  $a_2$  and  $a_3$  necessitates that we perform this procedure for every scan we take. This might be sufficient; however, additional concerns required further frequency calibration.

To extract the Stark shift, we must determine the frequency shift between two different laser scans, requiring the frequency axes to be linearized. However, it is essential to understand the meaning of the frequency zero point, as any uncertainty in that directly propagates into uncertainty in the Stark shift. In the linearization procedure, a convenient Fabry-Pérot peak is chosen as the zero point frequency. The Fabry-Pérot scans should all be identical, and so the zero point frequency should be constant, but, unfortunately, we must wait 14 seconds between HV on and HV off scans. These scans are to be compared, yet we are concerned that the Fabry-Pérot is not exactly stable over this time. Despite acoustic foam vibrational and thermal insulation, we did observe slow drifts in the Fabry-Pérot peaks.<sup>2</sup> The simplest and most accurate frequency reference available are the atoms themselves, so we reference the frequency to a simultaneous saturated absorption peak. We find the peak frequency and redefine  $a_0$  so that this peak is the zero frequency. Thus the frequency reference is stable between any two scans and we need not worry about slow drifts of the Fabry-Pérot.

### 5.1.2 Fitting Program Details

The fitting program breaks down into five primary sections, namely

1. Parameter management, loop control, data scanning, and formatting;
2. Fabry-Pérot fitting and extraction of non-linearity parameters;
3. Saturated absorption fitting and application of the frequency linearization function to the normalized laser PZT voltage;
4. FM signal fitting—either via approximation or the full analytic Voigt method—and extraction of reliable frequency reference; and
5. Subtraction of consecutive frequency references, propagation of errors, removal of outlying and misfit data, and output saving.

The formatting section of part 1 refers to normalization of both horizontal and vertical scales. In particular, the PZT voltage is normalized to  $x_j$  values such that  $-1 < x_j \leq 1$ .

The raw Fabry-Pérot scan appears as seven peaks of varying height approximately equally separated in frequency; due to the PZT non-linearity, this is not an exact

---

<sup>2</sup>We attempted active temperature stabilization via a PID controller and resistive heater, but this additional complexity did not produce better results.

equality. A peak finding routine locates the  $x_j$  value for each of the seven peaks:  $x_j^{(1)}, x_j^{(2)}, \dots, x_j^{(7)}$ . We define the center peak to be  $f = 0$  and each sideband to be exactly 100 MHz apart. Therefore, we have seven points on the relation  $f(x_j)$ , which are  $\{x_j^{(1)}, -300\}$ ;  $\{x_j^{(2)}, -200\}$ ;  $\{x_j^{(3)}, -100\}$ ;  $\{x_j^{(4)}, 0\}$ ;  $\{x_j^{(5)}, 100\}$ ;  $\{x_j^{(6)}, 200\}$ ;  $\{x_j^{(7)}, 300\}$ . These are shown as the points in Fig. 5.1b. The curve fit to these points represents the relation  $f(x_j)$  and serves to interpolate between these fixed values.

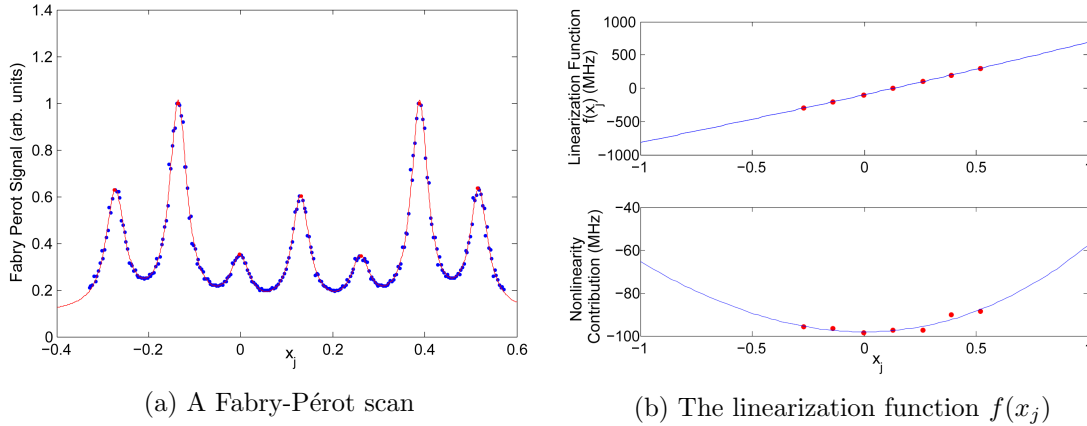


Figure 5.1: A Fabry-Pérot scan provides the locations of the seven 100 MHz - separated peaks in (a). These are represented in (b) on a frequency vs.  $x_j$  plot (upper). The non-linearity of order 2% is highlighted by subtracting off the linear term (lower).

In practice, we do not implement a linearization procedure exactly as described above. We assume a third order polynomial form for  $f(x_j)$ , and perform a sum of seven Lorentzians non-linear least-squares fit on the entire Fabry-Pérot scan. The functional form of this fit is

$$\begin{aligned}
 S_{FP} &= \sum_{n=-3}^3 \frac{h_n \gamma^2}{\gamma^2 + (f(x_j) - 100 \cdot n)^2} \\
 &= \sum_{n=-3}^3 \frac{h_n \gamma^2}{\gamma^2 + (a_0 + a_1 x_j + a_2 x_j^2 + a_3 x_j^3 - 100 \cdot n)^2}, \quad (5.1)
 \end{aligned}$$

where  $\gamma$  is the half-width at half-maximum of the Lorentzian peak,  $h_n$  is the amplitude, and  $a_i$  are the linearization parameters.  $\gamma^2$  appears in the numerator to remove  $\gamma$  dependence in the amplitude. Given the nature of such non-linear fits, we must give reasonably accurate initial guesses for the coefficients of  $f(x_j)$ . We find approximate values for  $a_0$ ,  $a_1$ , and  $a_2$  by means of a quadratic fit to the seven raw signal peak values. The initial guess for  $a_3$  is taken to be zero. Increasing the polynomial order to include an  $a_4 x_j^4$  term did not improve the quality (root mean standard error) of the fits, and markedly increased the  $1\sigma$  confidence intervals of the non-linearity parameters  $a_2$  and  $a_3$  due to fitting correlations between the parameters. By incorporating the linearization procedure into a fit of the full Fabry-Pérot scan rather than using a

fit to seven points, we achieve higher precision in the non-linearity parameters. This linearization procedure is critical to the extraction of the Stark shift, and so this reduces a major potential source of error.

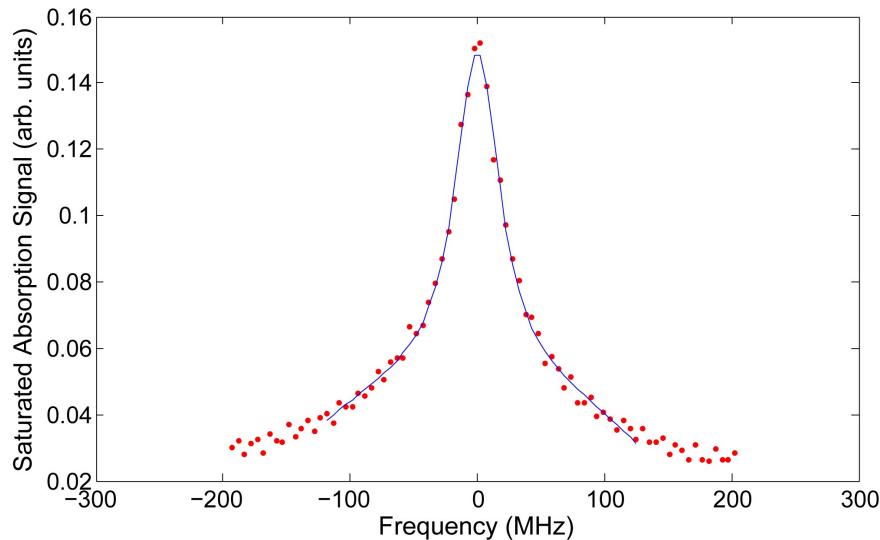


Figure 5.2: A fit to the saturated absorption signal is used to redefine the zero frequency as that of the SA peak.

From here, the saturated absorption fit redefines  $a_0$ , and so the normalized horizontal  $x_j$  axis is mapped to the frequency axis according to the cubic function determined above (this axis redefinition has already been accomplished in Fig. 5.2). We can fit the saturated absorption peak with either a Lorentzian or a Voigt profile. The Lorentzian fit is somewhat faster; however, this procedure is not the rate-limiting step in the total fitting routine, so this time difference is largely irrelevant. Figure 5.2 shows a full Voigt fit.

To improve computational speed, the final fit parameters from a run in a data set are used as the initial guesses for the next run. Counteracting this speed improvement but to improve fit quality, we implemented a ‘bootstrapping’ routine by which data is refit multiple times using the fit parameters from the previous fit to the same data. Due to the complicated landscape of  $\chi^2$  in parameter space, refitting can move beyond local minima, improving fit quality. Looping this process through several iterations can, depending on the data set, improve the reliability and quality of the fits remarkably.

With a well defined frequency axis, we then fit the FM signal. Our most reliable method is the full analytic Voigt fitting routine as mentioned at the beginning of this section. However, in order to improve fitting speed, we also explored numerous approximation methods, the most useful of which are discussed below.

### 5.1.3 Approximation Methods

Due to the inherent complexity of the full analytic profiles derived in sections 3.2 and 3.3, we spent significant effort in implementing and comparing various approximation methods. We only need to extract a frequency reference point out of each line shape, so an approximate fit to a limited section of the profile could, in theory, be just as useful as a full analytic fit—the full line shape fit is unnecessary.

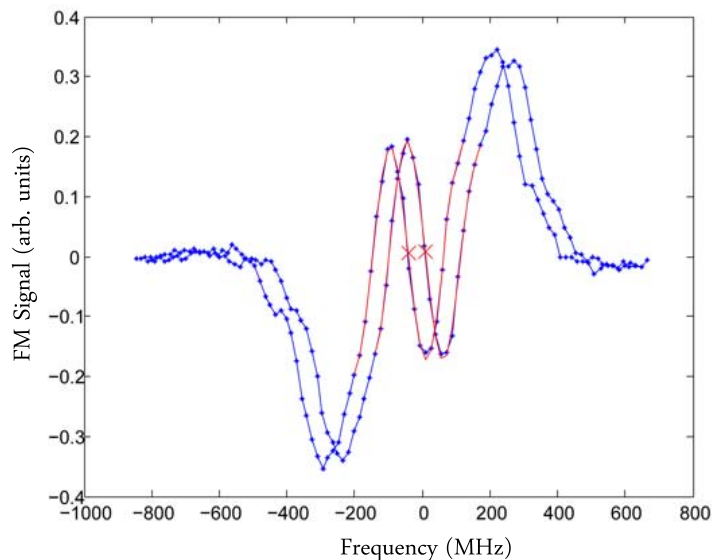


Figure 5.3: Two scans of the 410 nm transition in indium using 1f FM spectroscopy. The scan on the right corresponds to the high voltage off, and the scan on the left corresponds to the high voltage on. We wish to extract the horizontal separation between the two line shapes, so we need only find the horizontal separation between the two frequency reference points, which are marked by the X's.

#### Method 1: Overlap

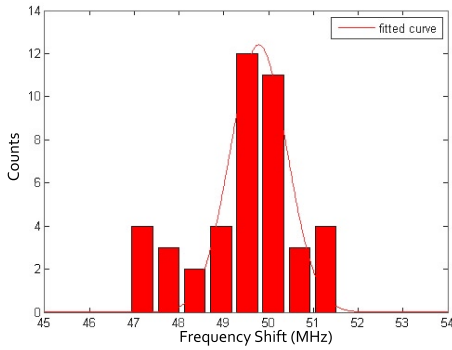
The first method quantifies the ‘error in overlap’ of the two scans. We calculate this quantity as we shift one scan in frequency towards the other. The minimum in this error corresponds to the shift at which the two profiles maximally overlap, and so this shift *is* the Stark shift. The great appeal of this method is its disregard for the functional form of the profiles being compared. Additionally, one can increase the accuracy simply by making the signals steeper.

At every frequency,  $f_i$ , at which we have a data point, we take the squared difference between the HV-on signal  $\mathcal{S}(f)$  and HV-off signal  $\mathcal{S}(f - s)$ . By summing over all frequencies, we have a figure of merit  $\xi$ , which we show to be quadratic for small shifts  $s$ .

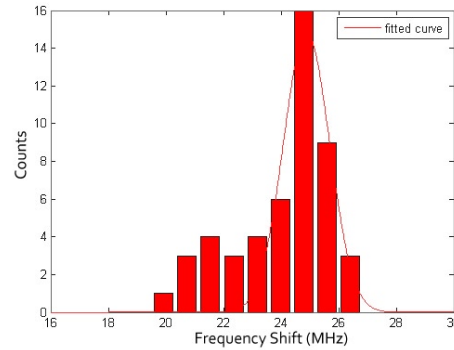
$$\begin{aligned}
\xi(s) &= \int_{all f} [\mathcal{S}(f) - \mathcal{S}(f - s)]^2 df \\
&= \int_{-\infty}^{\infty} [\mathcal{S}(f) - (\mathcal{S}(f) - \mathcal{S}'(f) \cdot s)]^2 df \\
&= \int_{-\infty}^{\infty} [\mathcal{S}'(f) \cdot s]^2 df \\
&= s^2 \int_{-\infty}^{\infty} \mathcal{S}'^2(f) df
\end{aligned} \tag{5.2}$$

We manually shift the HV-off signal by  $s$  and numerically compute  $\xi$ . By finding the minimum in a quadratic fitted to  $\xi(s)$ , we arrive arrive at a value for the Stark shift.

Unfortunately, this method does not result in uniformly accurate fits. For sufficient noisy data, which ours was, the figure of merit  $\xi(s)$  becomes a noisy quadratic with a particularly poorly resolved minimum. While one might think that this would be a random, statistical error, for opaque reasons, this method tended to underestimate the Stark shift, as revealed by non-normal, skew histograms of Stark shift values.



(a) 43 measurements at 20 kV.



(b) 42 measurements at 14 kV.

Figure 5.4: Two representative histograms of Stark shift measurements derived from overlap fitting. As was typical, this method produced non-normal and skew histograms.

## Method 2: Polynomial Root Finding

We can exploit symmetries in the FM signal to make good approximations to full analytic line shape. The  $1f$  FM signals are odd functions while the  $2f$  FM signals are even functions. Thus we can fit the central portions of both types and find either the central root or the central peak/trough depending on the demodulation frequency. For low modulation depth, the  $1f$  data looks qualitatively like a dispersion curve,

with a very nearly linear portion in the middle. We exploit this by fitting the linear region of each scan with a line which provides the frequency intercept of the scan. By subtracting the frequency intercepts of the appropriate scans, we extract the Stark shift (see Fig. 5.5).

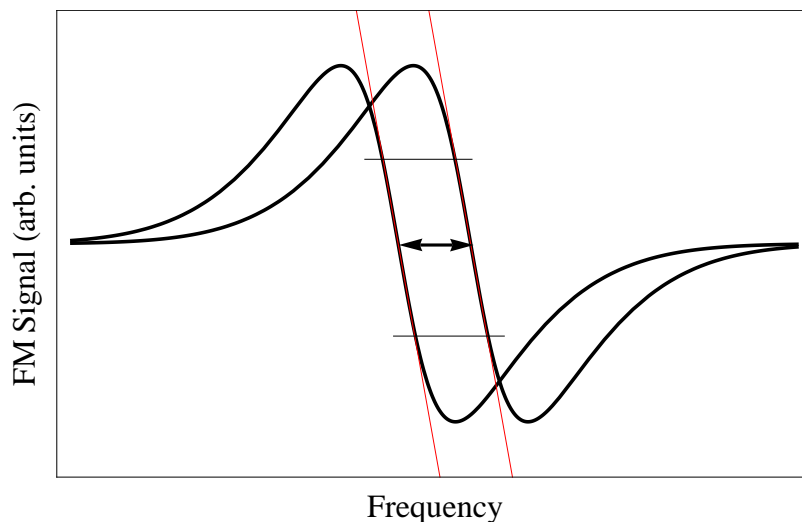


Figure 5.5: Linear approximation fit representation. The horizontal lines represent the cutoff values for the approximation region. The data inside the approximation region is then fit to a line. The separation in frequency intercepts, represented here by the double-headed arrow, is the Stark shift.

Unfortunately, due to our frequency linearization scheme which requires high modulation depths ( $\beta > 1$ ), the FM line shape is significantly more complicated and so the linear approximation breaks down. We can, however, take the natural extension of this idea, and fit the central region of the FM profile with a polynomial. Finding the global maximum and minimum brackets the central portion of the line shape for 1f signals, and so we take this central portion and fit it to a seventh degree odd polynomial (see Fig. 5.3). The polynomial fairly clearly must be at least fifth degree, and we found better quality fits in certain cases by extending the fit polynomial to seventh degree. This method was quite successful; the full Voigt fits were more consistent (smaller standard deviation for the same collection) by only a factor of two.

For the 2f data we implemented a similar scheme using quadratic and then quartic fit to the central peak or trough. This method was not nearly as successful as the polynomial fitting for the 1f data. This may be because, where the 1f data analysis needed to extract roots which are highly sensitive to the highly sloped middle of the scan, the 2f data analysis consisted in peak/trough finding which was less precise. We were able to circumvent this complication by switching to Lorentzian fitting.

### Method 3: Lorentzian Peak Finding

The FM line shapes, whether 1f or 2f, are composed of sums of Voigt line shapes. The 2f signals all have a central peak or trough which is well approximated by a single Voigt profile. In our atomic beam, the Lorentzian contribution is significant compared to the Gaussian contribution, and so we can approximate the central peak or trough as a Lorentzian. The Lorentzian fit has the advantage over the polynomial fit in that the approximate line shape is naturally closer to the data, and so we can fit a much larger portion of the data with only a few fit parameters. This is especially helpful since the extra included data points are in the steeper part of the data scan, so they offer stronger constraints on the frequency reference. Nevertheless, both the polynomial and Lorentzian approximation fits only use a fraction of the data, so we find, as expected, that the result is less precise than that from the full analytic fitting.

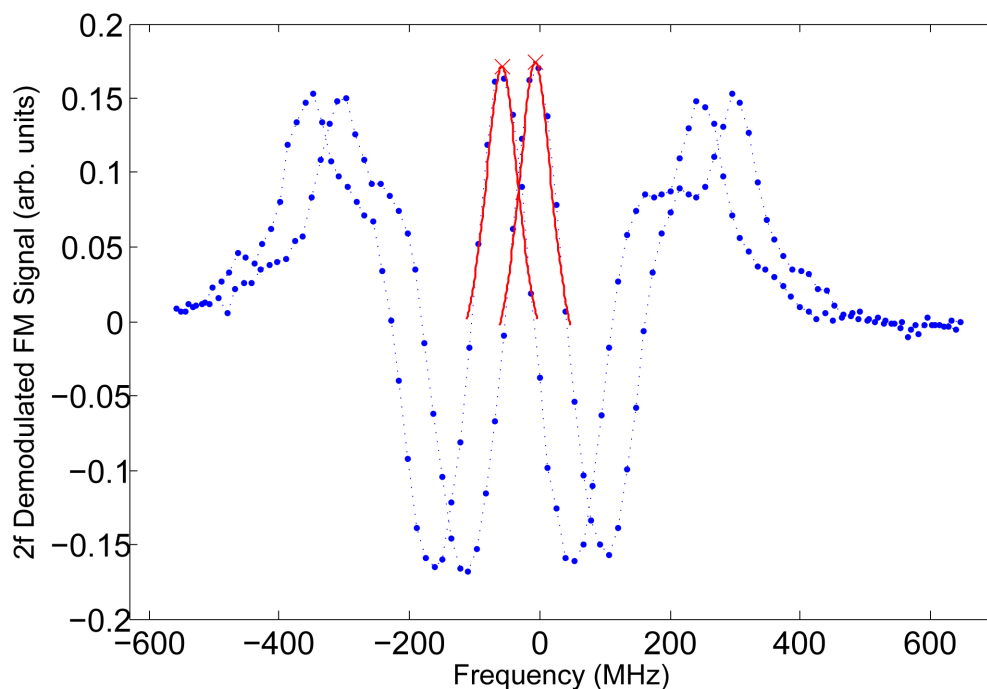


Figure 5.6: Fit to the central peak in a 2f FM signal using a Lorentzian approximation.

At this point, it is worth noting that, in all, we used four different FM line shape fitting programs: the polynomial approximation, the 1f analytic, the Lorentzian approximation, and the 2f analytic fit programs. These four different programs each serve as checks on the quality of the others.

## 5.2 Extraction of $k_S$

Error in the non-linearity parameters from either the Fabry-Pérot or saturated absorption fits clearly propagates into a final Stark shift uncertainty. We add in quadrature

with this the error associated with the actual FM signal fits to assign error bars to each individual Stark shift measurement. Due to the signal-to-noise ratio of our data and the fitting routines used, we can fit line shape features to about a MHz. All told, this results in an uncertainty of 3-5 MHz for each Stark shift measurement, between 6% and 50% of the total shift. We can extract a much more precise value of  $k_S = \frac{\Delta\nu_S}{E^2}$  by averaging the Stark shifts,  $\Delta\nu_S$ , for each high voltage value and plotting these eleven averages against the corresponding squared electric field value. The slope of such a plot is  $k_S$  extracted from one entire set of 550 data scans taken in one day. Figure 5.7 displays a sample plot of this kind. The uncertainty in the slope of the best fit line is roughly 0.4%. One might worry that this extraction method masks

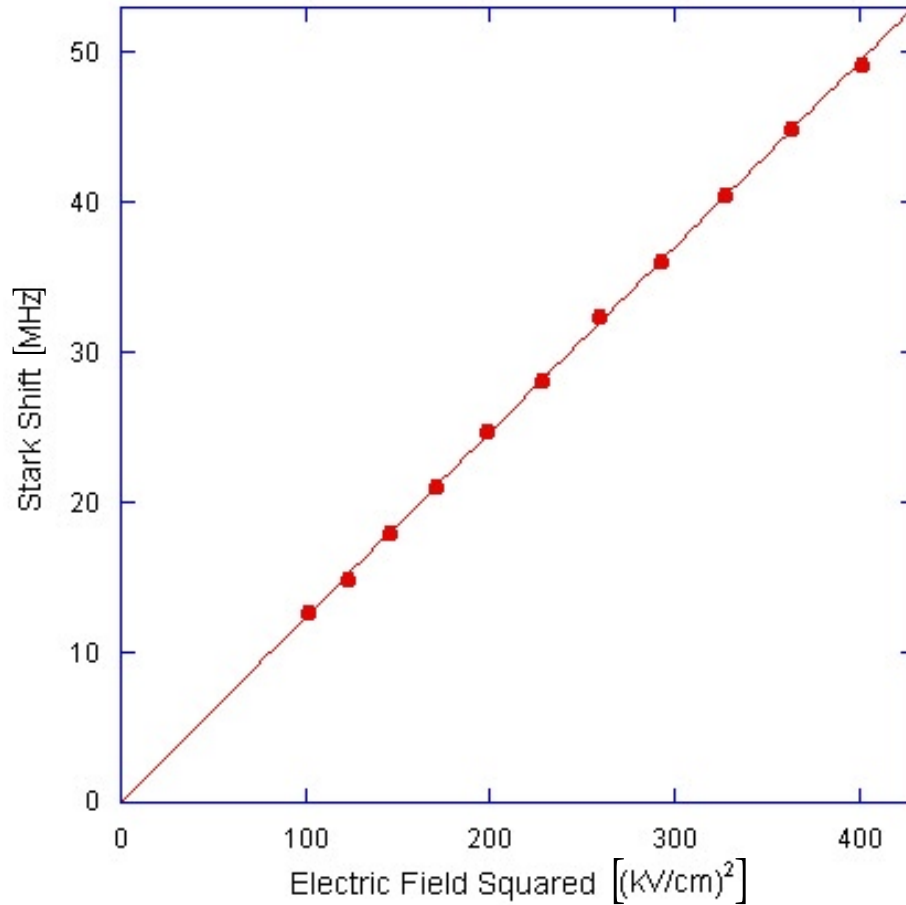


Figure 5.7: The Stark shift versus electric field squared. This represents one day of data, and the error bars are within the point size. The slope is  $|k_S|$ . Encouragingly, the vertical offset is consistent with zero.

errors due to unequal actual voltages corresponding to the same nominal voltage. To explore this, we also compute  $k_S$  from *every* Stark shift measurement since we record the precise simultaneous high voltage value with each data scan. This type of investigation does not reveal any remarkable structure. Figure 5.8 shows a histogram

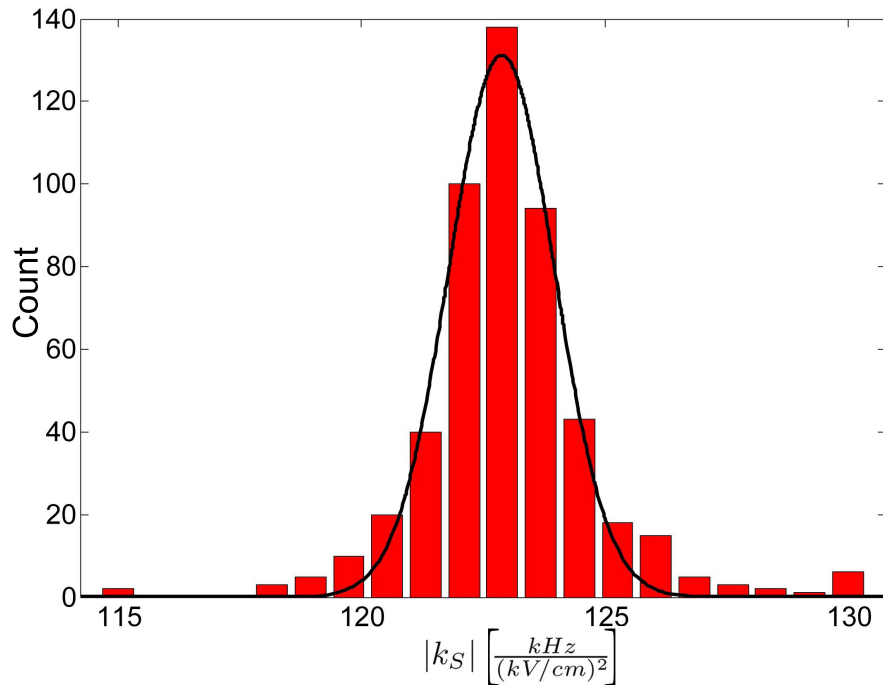


Figure 5.8: A histogram of all data. The solid line represents a fitted Gaussian, the peak of which is consistent with the weighted average of all data. The vertical axis represents bin counts.

of approximately 500 values, each value in which represents the weighted average of all data in a given set at a particular nominal voltage. We also fit a Gaussian to the binned counts, and the peak location of this Gaussian is consistent with both the weighted average of the individual values and the average of the 18 daily  $k_S$  values from the previous method. We finally quote our experimental value for  $k_S$  using the weighted mean of 6,000 full analytic Voigt fit  $k_S$  measurements,

$$k_S = -122.92(05) \frac{\text{kHz}}{(\text{kV/cm})^2}, \quad (5.3)$$

where the 0.04% error expresses the one-standard-deviation purely statistical uncertainty.<sup>3</sup> Recalling our electric field calibration systematic error of 0.2%, this is plenty of statistical precision.

<sup>3</sup>We can compare this to the linear fit extraction method. The average of 18  $k_S$  measurements with 0.4% uncertainty has an uncertainty of approximately  $0.4\%/\sqrt{18} = 0.09\%$ , or approximately twice the uncertainty of the full weighted averaging.

## 5.3 Investigation of Systematic Errors

We took data under numerous experimental configurations and fit the data in several independent ways to ensure that our final experimental value for the Stark shift was robust. In all, we explored 12 different systematic parameters, six binary comparisons and six continuous correlations; they are listed in Table 5.1.

Binary
1. fitting program (Voigt vs. approx.)
2. scan direction (up vs. down)
3. HV alternation direction (off $\rightarrow$ on vs. on $\rightarrow$ off)
4. demodulation frequency (1f vs. 2f)
5. hyperfine level ( $F = 5 \rightarrow F' = 4$ vs. $F = 4 \rightarrow F' = 5$ )
6. laser polarization (horizontal vs. vertical)
Continuous
1. laser power
2. modulation depth
3. electric field strength (squared)
4. magnetic field strength
5. demodulation phase
6. beam temperature

Table 5.1: A list of all explored variables for potential systematic errors. The value of  $k_S$  should not depend on any of these variables, so therefore, if we observe any dependence, we are resolving systematic errors within our experiment.

### 5.3.1 Binary Variables and Correlation Plots

For the binary comparisons, we split the entire data set according to that variable. Figure 5.9 compares the total weighted averages of each half set according to each variable. We assign a systematic error to each variable that has a difference in averages resolved to at least two combined standard deviations.<sup>4</sup> The magnitude of the error is taken to be equal to half the difference between the averages. We find that most binary variables are confidently consistent with each other. In particular, the independent fitting methods agree remarkably well, giving us assurance that the fitting programs do not introduce artifacts into the final value. We do resolve, however, small and only just resolved systematic errors corresponding to the scan direction and to the polarization of light. The scan direction dependence may indicate nascent multi-mode behavior of the laser at one end of the frequency sweep. This would not appear

<sup>4</sup>That is, with two weighted averages and uncertainties  $a \pm \delta a$  and  $b \pm \delta b$ , we find the difference  $\Delta_{ab} = a - b$  and the combined uncertainty in the difference  $\delta\Delta_{ab} = \Delta_{ab} \sqrt{(\frac{\delta a}{a})^2 + (\frac{\delta b}{b})^2}$ . The resolution of the difference in units of combined standard deviations is the ratio  $\frac{\delta\Delta_{ab}}{\Delta_{ab}}$ .

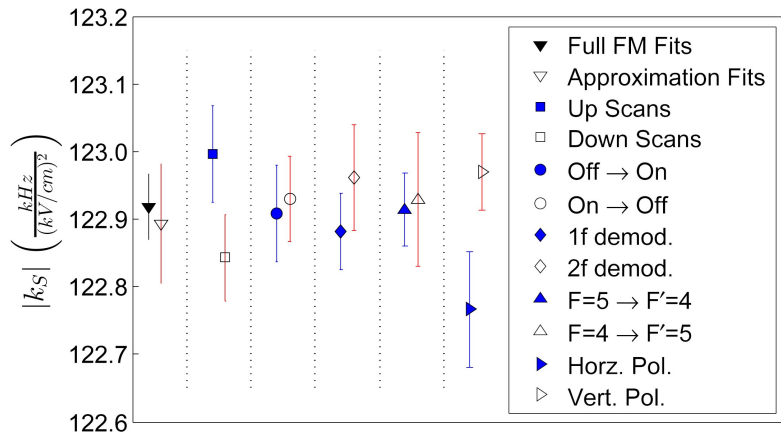


Figure 5.9: A comparison of binary systematic variations. Each point and error bar represents the weighted average of all data of the appropriate type. The comparisons, in order, are: results based on full analytic Voigt fitting vs. results derived from approximation fits; direction of the laser sweep; sequence of HV switching; rf lock-in demodulation frequency; hyperfine transition; and laser polarization. By comparing the two values in a binary partition of the total data set, we can explore potential systematic errors.

until the very end of one sweep direction, while the hysteresis of the system would prolong the multi-mode behavior a good while longer in the other sweep direction, and this imbalance could result in a sweep direction dependence. There is no good reason why we should detect a polarization dependence. Because the excited  $6S_{1/2}$  state has combined orbital and spin angular momentum  $J = \frac{1}{2}$ , there should be only a scalar, rather than tensor, polarizability, meaning that the atomic polarizability is independent of the polarization of light. One might worry that, since the hyperfine interaction can mix states with different  $F$  values, we might have a small tensor polarizability from the mixed states; however, because it derives from the hyperfine interaction, this additional polarizability is proportional to  $\frac{E_{hfs}}{E_{opt}} \alpha_0$  [46], which in this transition is  $2.6 \times 10^{-5} \alpha_0$ . At 0.16% of the mean, the dependence on polarization must be an artifact of the experiment. It is important to note that both of these resolved errors are distinctly less than 0.2% of the mean value—it is only our high statistical precision that enables us to resolve these effects.

We also used one additional tool to investigate and understand binary systematic errors: the correlation plot. Rather than averaging over the entire data subsets and then comparing, we can perform the comparisons first if the variable to be investigated is symmetric, by which we mean that there is a logical one-to-one assignment from each member of first partition set to the second. The first three binary variables of Table 5.1 (fitting program, scan direction, and HV alternation direction) are symmetric, while the last three are not. For a symmetric variable, we assign a point corresponding to each pair in a plot of mean value versus difference in values. If this seems a little

opaque, let us turn to an example: the dependence of  $k_S$  on the fitting method used.

The fitting program is a symmetric variable as long as every set of data is fit with both programs, as is the case for us. Therefore, for each data scan, we compare the results of the two programs and plot a point on a correlation plot (Fig. 5.11). First of all, we check the mean value of the high density center and confirm that it matches the calculated weighted fit.<sup>5</sup> The advantage of these plots resides in conferring increased confidence in our belief of the final value. If no correlation is found, then the variable dependence is truly statistically random and the regular mean is sufficient. If we do find a correlation, however, then we wish to extrapolate or interpolate to an appropriate value. This is often necessary in spectroscopic measurements of absolute energy differences between states, as the electric field probing the transition causes an AC Stark shift that increases the energy difference. A proper determination is the result of many measurements over a range of laser powers, after which the energy difference is extrapolated to *zero* laser power (see Fig. 5.10).

In our case, we wish to measure where the two fitting methods agree, i.e.  $\Delta k_S = 0$  in Fig. 5.11. The vertical intercept of the line of best fit predicts just this. Encouragingly, this value agrees with the overall mean, so the correlation plot does not reveal a new error in the data. The example in Fig. 5.11 was chosen for the quality of the correlation. The correlation does, though, lend support to our belief that the full Voigt fits are more reliable. A positive difference corresponds to a higher mean value, consistent with a model in which the Voigt fits are relatively constant compared to more widely, yet randomly varying approximate fits. However, this method provides a powerful and useful tool for exploring symmetric binary systematic variables, displaying structure that would otherwise remain hidden.

### 5.3.2 Continuous Correlations

We also searched for systematic errors in the possible dependence of  $k_S$  on continuous experimental parameters. Out the six variables explored, we found issue with only one, the squared electric field. By the very definition of  $k_S$  as the constant of proportionality between the Stark shift and the squared electric field,  $k_S$  should be independent of  $E^2$ . As can be seen in Fig. 5.12, we do not resolve a slope in a plot of  $|k_S|$  versus  $E^2$ . Nevertheless, we find excessive scatter about the mean among the

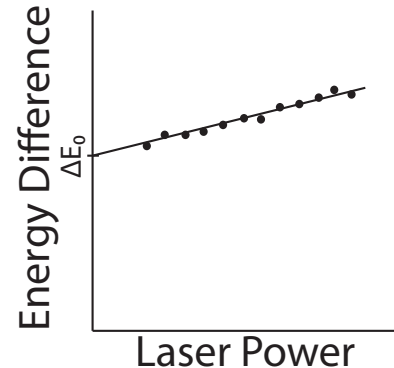


Figure 5.10: A model of laser power correlation in spectroscopic energy difference measurements. The actual difference  $\Delta E_0$  is unmeasurable and determined through extrapolation.

<sup>5</sup>There may be slight discrepancies, as correlation plots mask the weights of the points.

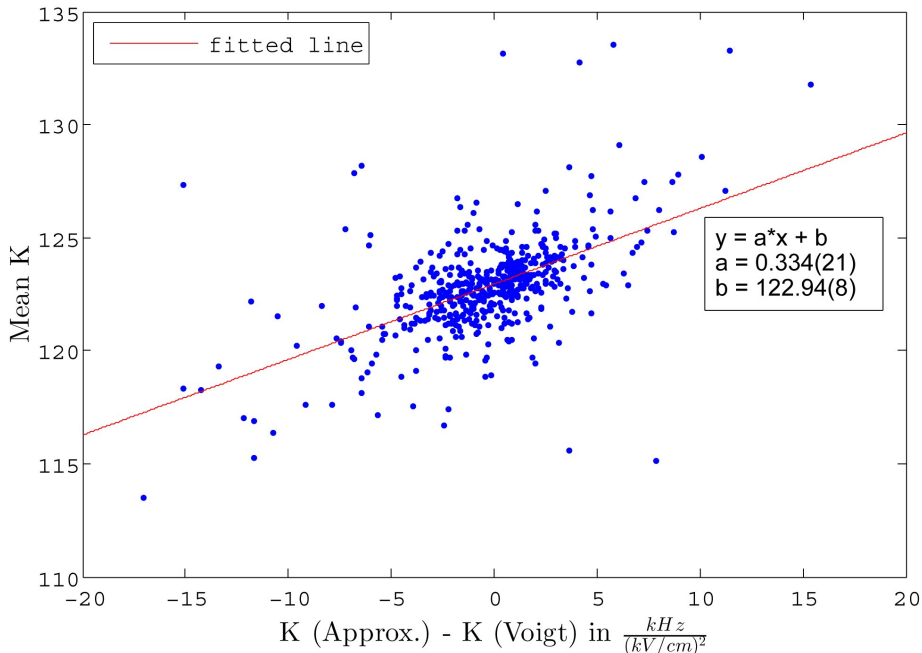


Figure 5.11: An example correlation plot exploring the fitting program systematic variable. Note that, despite the correlation, we find a vertical intercept that is consistent with the quoted value.

eleven voltage-averaged values. This is quantified by calculating a reduced  $\chi^2$  approximately equal to two. This is not strictly speaking a systematic error, but rather reflects an factor of  $\sqrt{2}$  underestimate in the statistical error. Therefore, due to the electric field dependence we assign an additional error equal to the intrinsic statistical error of  $0.05 \frac{\text{kHz}}{(\text{kV}/\text{cm})^2}$ , so that the combined statistical error (the quadrature sum of the intrinsic and additional statistical error) is  $0.05\sqrt{2} \frac{\text{kHz}}{(\text{kV}/\text{cm})^2} = 0.07 \frac{\text{kHz}}{(\text{kV}/\text{cm})^2}$ .

The Stark shift should be completely independent of the magnetic field, but we still control and zero the magnetic field in the interaction region by means of three axis magnetic field coils. We use a three axis flux gate magnetometer (Stefan Mayer Instruments FL3-100) to calibrate the field coils. While most data is taken with zero magnetic field, to explore any possible dependence, we vary the field strength. As expected, we find no dependence.

The Stark shift also should not depend on the modulation depth or the demodulation phase of the FM signal. Any dependence here would indicate issues with the lock-in amplifiers or, more likely, with our fitting programs, and so would have been helpful in troubleshooting these programs had any difference been found between the full analytic Voigt fits and the approximation fits or between the 1f and 2f demodulation data. However, all four of these fitting algorithm verification variables reveal no  $k_S$  dependence.

We did not find any dependence on the temperature of the beam. This could only arise if something strange were happening in our oven or collimation system,

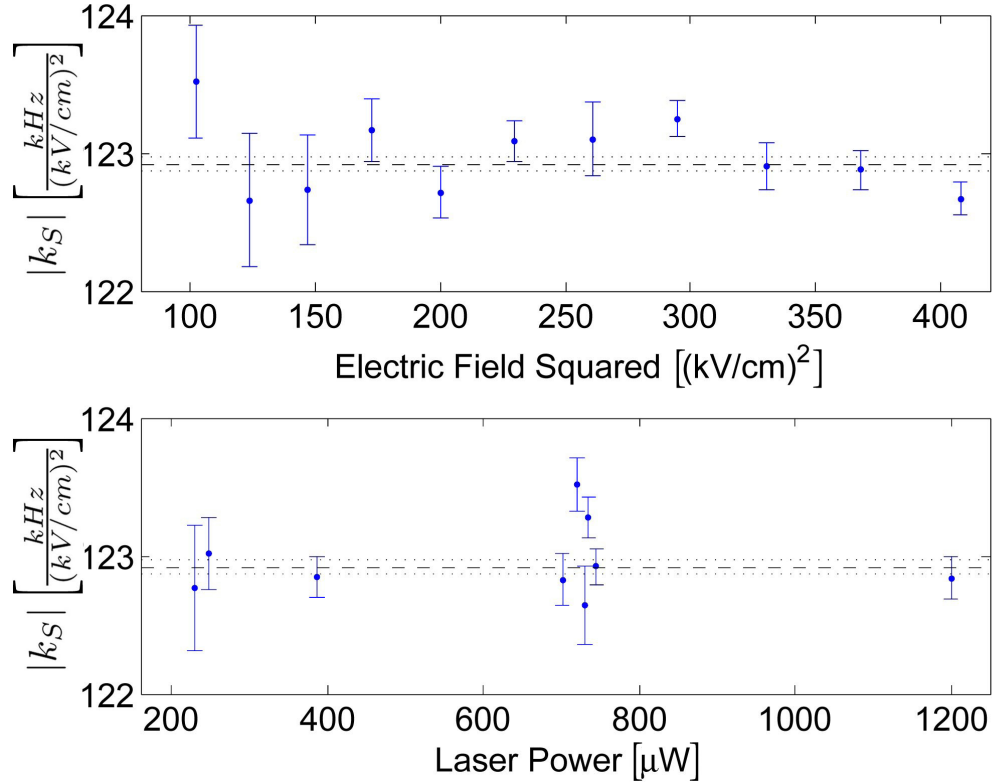


Figure 5.12: Two representative plots exploring potential systematic error in a continuous experimental variable.

such as wetting of the faceplate with indium, creating a poorly collimated spray of atoms which would increase the Doppler width of the signal. Nevertheless, it is nice to confirm that nothing unexpected is occurring.

We also were concerned about possible optical pumping, saturation, or even AC Stark effects due to high laser power in the interaction region. As can be seen in Fig. 5.12, over a factor of 6 variation in interaction region laser power, we resolve no dependence. This confirms our prediction from appendix B in which we show that the intensity of the laser in the interaction region is 0.012% of the saturation intensity. While the saturation intensity is not an exact threshold value for the appearance of any of these intensity dependent effects, this does show that the intensity of the laser is very low compared to a characteristic intensity of saturation.

### 5.3.3 Final Uncertainties and Results

In all, we have identified four sources of systematic error. These are tabulated in Table 5.2, along with the intrinsic statistical uncertainty and the quadrature sum of all errors. This results in our final value for  $k_S$  within the  $5P_{1/2} \rightarrow 6S_{1/2}$  transition

Table 5.2: All sources of error resolved in the present work.

Magnitude in		Sources of error
$\frac{\text{kHz}}{(\text{kV}/\text{cm})^2}$	% of mean	
0.05	0.04	statistical
0.05	0.04	electric field dependence
0.14	0.11	laser scan direction
0.20	0.16	laser polarization
0.25	0.20	electric field calibration
0.33	0.27	quadrature sum of errors

in atomic indium of

$$k_S = -122.92(33) \frac{\text{kHz}}{(\text{kV}/\text{cm})^2} \quad (5.4)$$

Working through the conversions given in appendix A and section 1.2, this corresponds to a polarizability difference of

$$\Delta\alpha_0 = 1000.2(2.7) \text{ a.u.}, \quad (5.5)$$

29 times more precise than the previous result by Fowler and Yellin, [28] and in excellent agreement with the new theoretical prediction of this value [29]. Following the derivation provided in section 1.2.2, this results in lifetimes for the  $6P_{1/2}$  and  $6P_{3/2}$  states of

$$\tau_{6P_{1/2}} = 63.77(50) \text{ ns} \quad (5.6)$$

$$\tau_{6P_{3/2}} = 58.17(45) \text{ ns}, \quad (5.7)$$

values which are an order of magnitude more precise than previous measurements [32] and are also in excellent agreement with recent predictions based on an entirely independent theoretical calculation [31].

# Chapter 6

## Ongoing and Future Work

While we have completed a measurement of the polarizability difference between the  $5P_{1/2}$  and  $6S_{1/2}$  states, there are plenty of exciting options for further work. The combination of the atomic beam apparatus and FM spectroscopy allows for very high sensitivity, high precision measurements in a wide variety of systems.

### 6.1 Thallium Lifetimes

The first logical extension of this work does not involve further experimentation, however. In 2002, the Majumder lab published a precise measurement the Stark shift of the first excited state in thallium, exactly analogous to the work presented in this thesis [47]. Using the results of state-of-the-art atomic theory, the thallium reduced electric dipole matrix elements can be calculated with uncertainty of order 1%. This allows an extraction of the thallium  $7P_{1/2;3/2}$  lifetimes exactly we described in section 1.2.2 for indium. This has been accomplished and published [48].

$$\tau(\text{Tl } 7P_{1/2}) = 60.21(55) \text{ ns}$$

$$\tau(\text{Tl } 7P_{3/2}) = 46.44(42) \text{ ns}$$

### 6.2 Two Step Excitation: the $6P_{3/2}$ Polarizability

We are in the process of setting up a two step, two color excitation to the indium  $6P_{3/2}$  state. Due to the quantum mechanical selection rule that requires  $\Delta l = \pm 1$ , we cannot excite the  $5P_{1/2}$  valence electron directly to this state. Instead, we use our existing 410 nm laser to excite a population of the indium into the  $6S_{1/2}$  state. A second overlapping 1291 nm laser can then excite these atoms to the  $6P_{3/2}$  state. This two step, two color technique has been used in the Majumder lab already in indium and thallium vapor cells to measure hyperfine structure and is described in Gunawardena *et al.* [49] We plan to overlap these lasers and pass them through the atomic beam. By locking the blue laser to the 410 nm transition and also performing

FM spectroscopy with the IR laser, we aim to measure the Stark shift in this excited state transition.

To lock the blue laser, we will implement the frequency stabilization technique developed in the Majumder lab and described in [50]. In brief, we send the blue laser through a 260 MHz acousto-optic modulator (AOM), which produces two sidebands shifted by  $\delta\omega_{\pm} = \pm 260$  MHz. The zeroth order beam passes straight through to the experiment. The two first order sidebands are overlapped via a polarizing beam splitter and sent through an indium vapor cell. The two beams are both absorbed by the atoms, with highly Doppler broadened Gaussian profiles, but the absorption profiles are shifted relative to each other by 520 MHz. After passing through the cell, the beams are separated with another polarizing beam splitter and directed to a differential photo-detector. This outputs the *difference* between the two broad absorption profiles, an output which is very nearly linear over several hundred megahertz. Sending this into a PID lock-box allows for fast, real-time adjustment of the laser, locking it to a specified frequency. This method regularly achieves sub-MHz level laser frequency stabilization.

Extraction of the Stark shift from this setup is complicated due to the two step excitation scheme. Figure 6.1 shows the three relevant energy levels, both unperturbed and Stark shifted. Note that the electric field shifts all levels to lower energies, with the upper levels shifted more. As discussed in [48], we define the Stark shift in the lower transition as  $\Delta_{21} = f_{21}^0 - f'_{21}$  and the Stark shift in the upper transition as  $\Delta_{32}$ . As will be shown in section 6.2.2,  $\Delta_{32} \gg \Delta_{21}$ . The primary subtlety arises because we will be locking the blue laser to the atomic transition in an external, field-free vapor cell. This means that the blue laser will excite a non-zero velocity class of atoms in the atomic beam. We might worry that the Stark shift will pull the atoms off resonance with the laser, but for typical electric fields of around 10 kV/cm,  $\Delta_{21} \approx 10$  MHz. Since the residual Doppler width in the atomic beam is around 100 MHz, the excitation efficiency of the blue laser will not be meaningfully affected. Nevertheless, we must take the Doppler shift of the ex-

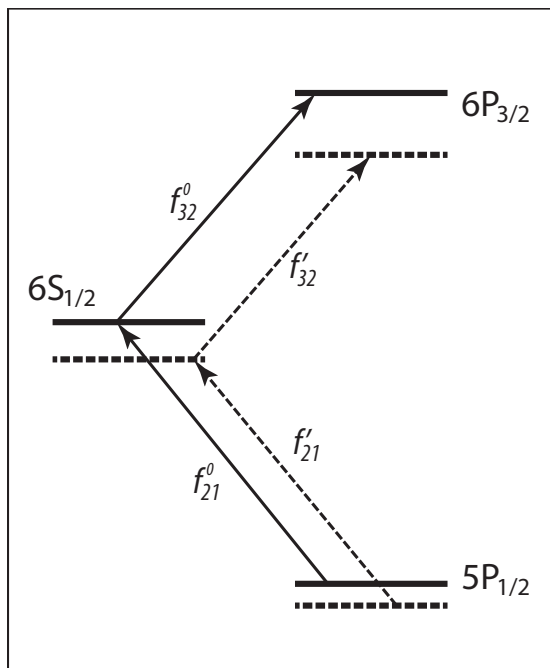


Figure 6.1: A partial energy level diagram showing the three relevant levels for the two step excitation (not to scale). Solid lines indicate the unperturbed system while dotted lines indicate the same system under the influence of the electric field.

cited  $6S_{1/2}$  atoms into account:

$$|\Delta_{32}| = f_{32}^0 - f'_{32} + |\Delta_{21}| \frac{f_{32}}{f_{21}}. \quad (6.1)$$

Since the resonance frequencies  $f_{32}$  and  $f_{21}$  are very accurately known, and we have just completed a precise measurement of  $\Delta_{21}$ , our experimental measurements of  $f_{32}^0 - f'_{32}$  will determine  $\Delta_{32}$  with no loss of precision.

We have already rebuilt a Littrow configured diode laser using an old 1291 nm Mitsubishi ML7781A diode. A major challenge of this experiment lies in the very low optical depth of the atomic beam. Frequency modulation spectroscopy proved able to resolve a clean signal for the first step. However, the second step IR laser has at most half as many atoms in the excited state, and actually many fewer. The low laser power that resulted in a narrow clean signal in the completed work now will result in a small population excited to the  $6S_{1/2}$  state. Very careful overlapping and alignment will be required to see any signal. At best, we hope to see a signal that is an order of magnitude weaker than that recorded in the completed work.

### 6.2.1 Two Tone Modulation

Because of the particular equipment we have in the lab at IR wavelengths, we will use a form of FM spectroscopy for this measurement that differs from that used in the present work. Used previously in the Majumder lab [42], this method calls for modulating the 1291 nm laser at *two* nearby frequencies. First described by Janik *et al.* in 1986 [51], this so called “two-tone” spectroscopy retains the high signal-to-noise ratio of regular frequency modulation spectroscopy while allowing detection and processing frequencies to be significantly lower. In this method, the laser is modulated at both  $\omega_m + \Omega/2$  and  $\omega_m - \Omega/2$  with  $\Omega \ll \omega_m$ . Phase sensitive detection by means of a lock-in amplifier referenced at  $\Omega$  provides a low noise, high sensitivity demodulated signal. Since  $\Omega$  is by assumption much smaller than  $\omega_m$ , we save money and aggravation by using cheaper, off-the-shelf commercial electronics. Another convenience of note is our ability to use low modulation depths—we need not push the limits of phase modulators. We compare spectra for regular and two-tone frequency modulated lasers in Fig. 6.2

For this experiment, we plan on setting  $\omega_m = 1$  GHz, 10 times faster than in the completed work, and  $\Omega/2 = 1$  MHz. The output of two the RF synthesizers that produce these frequencies will be sent to an RF mixer, effectively multiplying the two signals. This multiplication results in frequency components at the sum and difference frequencies, i.e. 1,001 MHz and 999 MHz.<sup>1</sup> In his thesis, Holmes derives the resulting demodulated transmission signal given this two-tone modulation assuming  $\beta \ll 1$ . Following his derivation but also allowing for arbitrary relative demodulation

---

<sup>1</sup>Nonlinear effects in the mixing circuit can lead to additional harmonics i.e.  $\omega_m \pm \Omega, \omega_m \pm \frac{3}{2}\Omega, \dots$ . Keeping the power of the lower frequency signal sufficiently low makes this effect negligible.

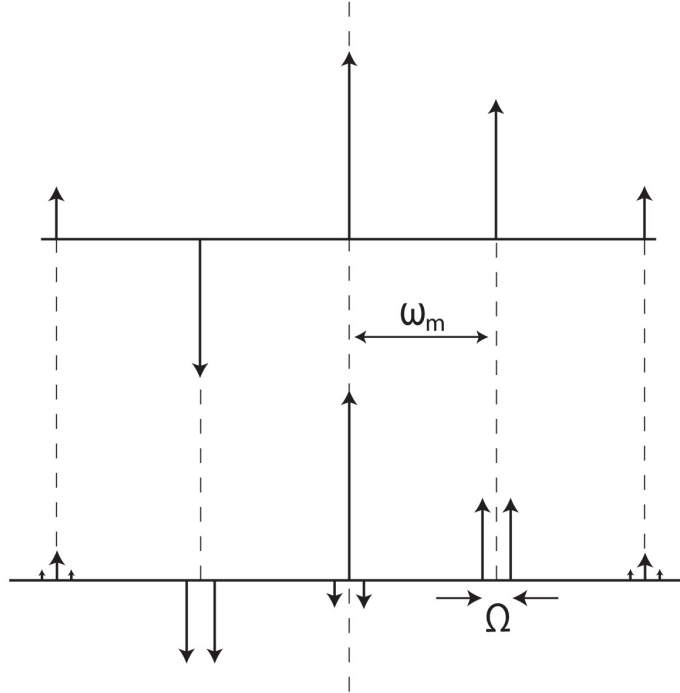


Figure 6.2: A comparison of the spectra of regular (top) and two-tone (bottom) frequency modulation at moderate modulation depth ( $\beta \approx 1$ ). Note the small amplitudes at  $\omega_0 \pm \Omega/2$ . Arrow directions indicate the relative phase of electric field components.

phase with a complex transmission function  $T = e^{-\delta - i\phi}$ , we find

$$\begin{aligned} I_{demod}^{two-tone} &= 4c\epsilon_0 |\tilde{E}_0|^2 J_0^2(\beta) J_1^2(\beta) [T^2(\omega_c - \omega_m) + T^2(\omega_c + \omega_m) - 2T^2(\omega_c)] \cos(\theta_d) \\ &= 8c\epsilon_0 |\tilde{E}_0|^2 J_0^2(\beta) J_1^2(\beta) [2\delta(\omega_c) - \delta(\omega_c - \omega_m) - \delta(\omega_c + \omega_m)] \cos(\theta_d) \quad (6.2) \end{aligned}$$

In the low modulation depth limit, there are no cross terms between transmission functions, so we only have  $T^*(\omega_n)T(\omega_n) = e^{-2\delta(\omega_n)}$  terms. Therefore, the term involving  $\sin(\theta_d)$  times dispersion profiles is zero.

This results in two downward dips each separated from the larger central peak by  $\omega_m = 1$  GHz. Figure 6.4 shows a simulation of this demodulated transmission two-tone FM signal. Clearly, we will need to scan the IR over more than two GHz to reveal the entire signal. Once we have found this signal, the experiment will proceed similarly to the completed work: we will take scans with the electric field alternating on and off. Measuring the frequency shift between these scans relative to a stable reference such as a saturated absorption signal<sup>2</sup> will then provide the Stark shift. A full experimental layout of this next experiment is provided in Fig. 6.3.

A primary challenge to be addressed is determining a reliable frequency linearization scheme. Since we will have low modulation depths such that only first order

<sup>2</sup>Technically, this would be a ‘hole burning’ technique. It is the same as a saturated absorption set up except that the pump beam is the first step laser and can be co-propagating rather than counter-propagating. The distinction is not just semantic, but it is not worth worrying about it.

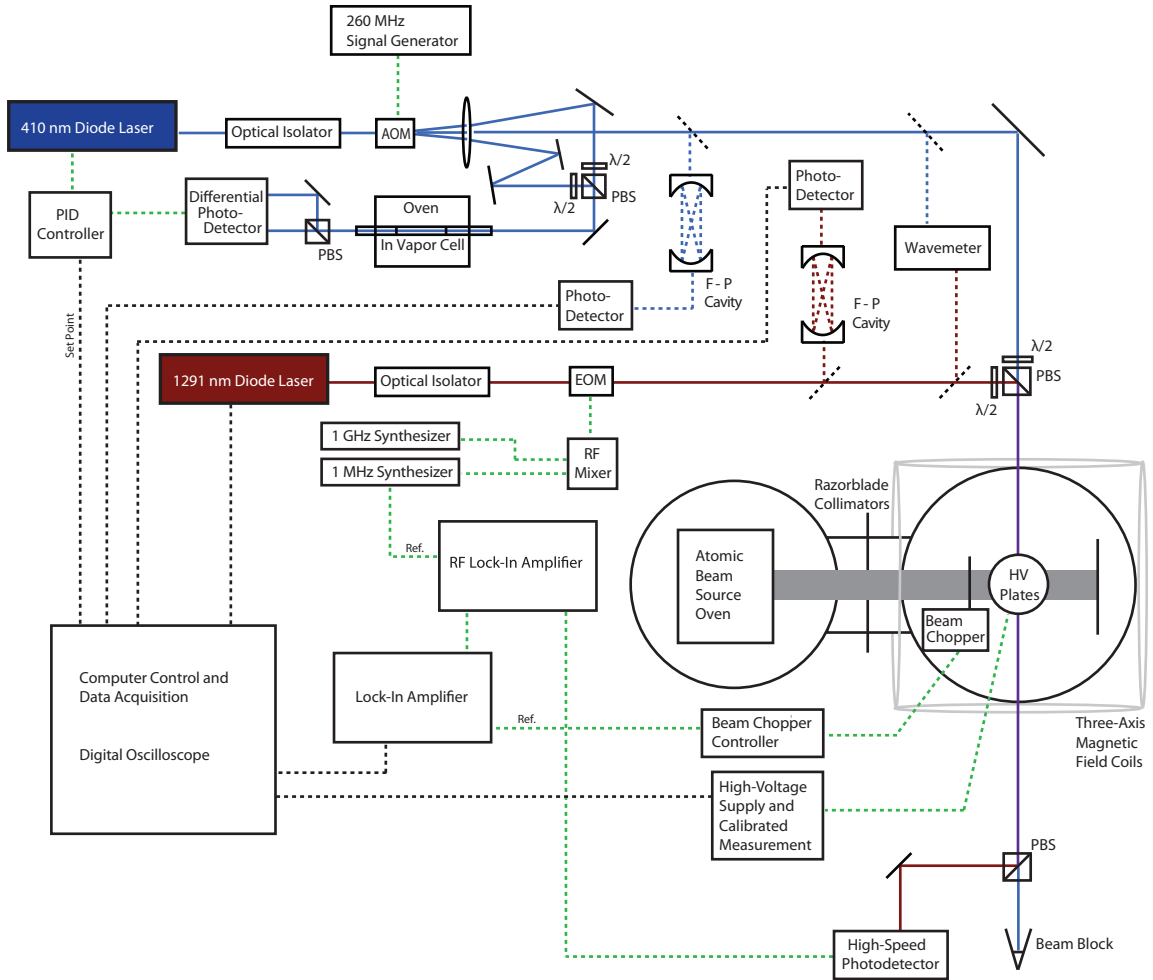
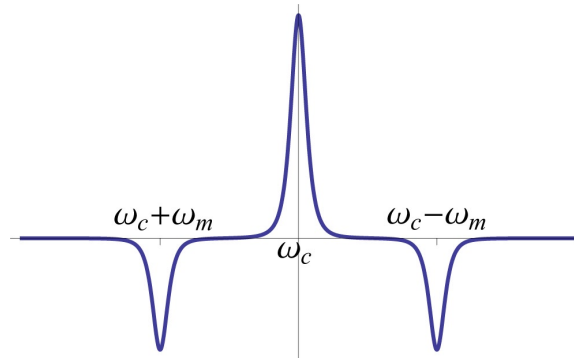


Figure 6.3: A diagram of the full setup for the second step Stark shift measurement.

Figure 6.4: A simulation of the demodulated transmission two-tone FM signal as expressed in Eq. (6.2). Note that while we demodulate at  $\Omega = 1$  MHz, the spectral features are separated by  $\omega_m = 1$  GHz.



sidebands and the carrier frequency are present, we cannot reuse the current method of linearization utilizing Fabry-Pérot frequency spectra. However, in the atomic beam, the spectral width of the features will still be  $\Gamma \sim 100$  MHz, but the modulation frequency is now  $\omega_m = 1$  GHz, so we are approaching the  $\Gamma \ll \omega_m$  limit, in which the demodulated signal has features exactly separated by  $\omega_m$  (see section 3.2). Therefore, the signal should be self-calibrating. This, combined with more traditional linearization methods using the stabilized free spectral range of a calibrated Fabry-Pérot, should provide reliable frequency linearization.

## 6.2.2 Rough Estimate of Magnitude

Before beginning this new Stark shift measurement, we wanted to have a rough, “experimentalist’s,” understanding of its magnitude. We expect the magnitude of the polarizability of the  $6P_{3/2}$  state to be much larger than either the  $6S_{1/2}$  or  $5P_{1/2}$  states because of the higher density of nearby energy levels. Figure 6.5 gives an energy level diagram for indium that includes many excited states approaching the continuum.

To estimate the magnitude of the  $6S_{1/2}$  state’s polarizability, we first recall the definition of atomic state polarizability from Eq. (1.7),

$$\alpha_0(\xi) = \frac{2}{3(2j_\xi + 1)} \sum_{k \neq \xi} \frac{\langle k || D || \xi \rangle^2}{\mathcal{E}^{(0)}(k) - \mathcal{E}^{(0)}(\xi)}.$$

We need only look up values for the reduced electric dipole matrix elements to calculate a truncated sum. This sum ignores many important effects from continuum (unbound) electron states as well as core excitations (e.g. states like  $5S^26P^2$ ), but it is nevertheless useful for quantifying the dominant effects. We first conduct the calculations for the  $5P_{1/2}$  and  $6S_{1/2}$  states as a gauge of the accuracy of this method. Then we calculate the  $6P_{3/2}$  polarizability. These calculations are shown in Table 6.1.

The reduced electric dipole matrix elements squared are listed under line strengths; the values of the line strengths as well as the transition wavelengths are quoted from [15]. The energy difference in Hartrees (the atomic unit of energy, see Appendix A for review) is calculated from the transition wavelength. Then the contribution  $\frac{\langle k || D || \xi \rangle^2}{\Delta \mathcal{E}_{k,\xi}}$  of each matrix element is calculated and tabulated. We truncate the sum after the

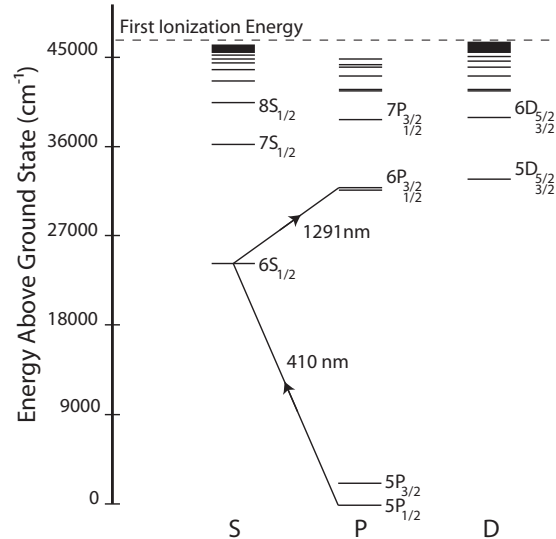


Figure 6.5: An energy level diagram for indium showing higher energy states connecting to one of the relevant states by an E1 transition. Hyperfine structure is not shown. This plot is constructed from data in [52].

Initial State	Final State	Line Strength (a.u.)	Transition Wavelength ( $\text{\AA}$ )	Energy Difference (Hartrees)	Contribution
$5P_{1/2}$	$6S_{1/2}$	3.64	4153	0.1097	33.2
	$5D_{3/2}$	7.24	3045	0.1496	48.4
	$7S_{1/2}$	0.293	2792	0.1631	1.80
	$6D_{3/2}$	1.23	2578	0.1767	6.96
	$8S_{1/2}$	0.0888	2493	0.1827	0.486
	$7D_{3/2}$	0.406	2410	0.1891	2.15
	$8D_{3/2}$	0.187	2329	0.1956	0.956
<b>Polarizability <math>\alpha_0(5P_{1/2})</math></b>					31.3
$6S_{1/2}$	$5P_{1/2}$	3.64	-4153	-0.1097	-33.2
	$5P_{3/2}$	8.56	-4576	-0.0995	-86.0
	$6P_{1/2}$	36.1	13669	0.0333	1083
	$6P_{3/2}$	70.3	13146	0.0347	2028
	$7P_{1/2}$	0.475	7002	0.0651	7.30
	$7P_{3/2}$	1.30	6949	0.0656	19.8
	$8P_{1/2}$	0.0786	5806	0.0785	1.00
	$8P_{3/2}$	0.245	5787	0.0787	3.11
<b>Polarizability <math>\alpha_0(6S_{1/2})</math></b>					1008
$6P_{3/2}$	$6S_{1/2}$	70.3	-13146	-0.0347	-2029
	$5D_{3/2}$	20.5	86580	0.00526	3896
	$5D_{5/2}$	186	84890	0.00537	34661
	$7S_{1/2}$	88.8	24184	0.0188	4714
	$6D_{3/2}$	8.45	14065	0.0324	261
	$6D_{5/2}$	74.8	14043	0.0324	2306
	$8S_{1/2}$	3.22	11858	0.0384	83.8
	$7D_{3/2}$	1.59	10197	0.0447	35.6
	$7D_{5/2}$	14.2	10190	0.0447	317
	$8D_{3/2}$	0.598	8889	0.0512	11.7
	$8D_{5/2}$	5.36	8886	0.0513	105
<b>Polarizability <math>\alpha_0(6P_{3/2})</math></b>					7394
<b>Rough Estimations of Polarizability Difference</b>					
$\alpha_0(6S_{1/2}) - \alpha_0(5P_{1/2}) = 977$ a.u.					
$\alpha_0(6P_{3/2}) - \alpha_0(6S_{1/2}) = 6386$ a.u.					
$\alpha_0(6P_{3/2}) - \alpha_0(5P_{1/2}) = 7363$ a.u.					

Table 6.1: Tabular representation of our rough estimation calculation of the excited state polarizabilities. This does not include continuum or core contributions. Compare to Safronova's results in Table 6.2.

contributions become negligible. We then multiply the sum by the angular factor  $\frac{2}{3(2j_\xi+1)}$  and present the result below. All that is left, then, is to take differences.

Our estimation for  $\alpha_0(6S_{1/2}) - \alpha_0(5P_{1/2})$  is within 5% of the measured value and Safronova's "real" theory. It seems safe to assume that atomic theory calculations for the higher energy levels are less precise, so we expect a larger error in the  $6P_{3/2}$  polarizability. Rather than speculate about the magnitude of this error, we can look to Safronova, *et al.* who recently published theoretical predictions of these polarizabilities. In [29], Safronova used two state-of-the-art numerical methods to calculate the polarizabilities of the  $5P_{1/2}$ ,  $6S_{1/2}$ ,  $6P_{1/2}$ , and  $6P_{3/2}$  states of indium. Her results are consolidated into Table 6.2. While our estimation of  $\alpha_0(6S_{1/2})$  was within 5% of her result, our estimation for  $\alpha_0(5P_{1/2})$  was 50% smaller because core effects are relatively larger here, and our estimation for  $\alpha_0(6P_{3/2})$  was also 30% too small. The small magnitude of  $\alpha_0(5P_{1/2})$  makes this error matter little to the overall prediction of the polarizability difference  $\alpha_0(6S_{1/2}) - \alpha_0(5P_{1/2})$ ; however, the new result of Safronova is very useful in understanding the magnitude of the new polarizability difference  $\alpha(6P_{3/2}) - \alpha_0(6S_{1/2})$  for which Safronova predicts,

$$\alpha_0(6P_{3/2}) - \alpha_0(6S_{1/2}) = \begin{cases} 9068 \text{ a.u.} : & F = 3, 6 \\ 11932 \text{ a.u.} : & F = 4, 5 \end{cases} \quad (6.3)$$

### 6.2.3 Tensor Polarizability

It would be reasonable to wonder why we are probing the  $6P_{3/2}$  state rather than the  $6P_{1/2}$  state. As can be extracted from Table 6.1, driving the transition from  $6S_{1/2}$  to  $6P_{1/2}$  requires a 1343 nm IR laser. While there exist diodes that can be tuned to reach both 1291 nm and 1343 nm, we currently do not have any. We do, however, have old diodes that lase at 1291 nm. If we have to pick between the two 6P states, though, we would rather explore the  $6P_{3/2}$  state. As alluded to in 1.2.1, measuring polarizability differences involving a  $j = 3/2$  state such as  $6P_{3/2}$  offers the opportunity to measure a tensor polarizability. This means that we expect to observe a Stark shift (and polarizability difference) that depends on the polarization of the IR light. Observing this tensor polarizability in addition to the scalar polarizability is a promising goal of significant theoretical interest.

Following [29] and [26], the tensor polarizability is an additional component  $\alpha_2$  to the polarizability. This results in an energy shift given by

$$\Delta\mathcal{E}(J, m_J) = -\frac{1}{2}\alpha_0 E^2 - \frac{1}{2} \frac{3m_j^2 - J(J+1)}{J(2J-1)} \left( \frac{3\cos^2(\theta_\varepsilon) - 1}{2} \right) \alpha_2 E^2, \quad (6.4)$$

where  $J$  is the combined orbital and spin angular momentum,  $m_j$  is the z-projection of that angular momentum,  $E$  is the magnitude of the applied electric field, and  $\theta_\varepsilon$  is angle of the polarization vector of the laser from vertical. This ignores the hyperfine dependence, which we actually wish to use to measure  $\alpha_2$ . Therefore we rewrite this to contain the hyperfine dependence explicitly:

$$\Delta\mathcal{E}(F, m_F) = -\frac{1}{2}\alpha_0 E^2 - \frac{1}{2} C(F, m_F) (3\cos^2(\theta_\varepsilon) - 1) \alpha_2 E^2, \quad (6.5)$$

where the state dependent coefficient  $C(F, m_F) = \frac{[3m_F^2 - F(F+1)][3X(X-1) - 4F(F+1)J(J+1)]}{(2F+3)(2F+2)2F(2F-1)2J(2J-1)}$ , and  $X = F(F+1) + J(J+1) - I(I+1)$ . We recall that indium has a nuclear spin of  $I = 9/2$ . The explicit dependence on the magnetic quantum number,  $m_F$ , results in significant additional complexity, as the atomic population of each sublevel must be understood in order to extract  $\alpha_2$ . One can show, for instance, that an equal population of atoms in all possible sublevels for a given  $F$  results in an average tensor polarizability of 0. In the special case that both laser polarizations are in the  $\hat{z}$  direction, we know that  $\Delta m_F = 0$  for all transitions. We can safely assume that the ground state has even population between sublevels, so if, as an example, we consider the transition  $5P_{1/2}(F=4) \rightarrow 6S_{1/2}(F'=5) \rightarrow 6P_{3/2}(F''=6)$  with  $\hat{z}$  laser polarizations, we conclude that the  $|m_F| \leq 4$  sublevels all have equal population while the  $5 \leq |m_F| \leq 6$  sublevels are unpopulated. This results in a total tensor polarizability coefficient  $C_{net} = \sum_{m_F=-4}^4 C(6, m_F) = -\frac{3}{4}$ . If instead, we considered the  $5P_{1/2}(F=4) \rightarrow 6S_{1/2}(F'=5) \rightarrow 6P_{3/2}(F''=5)$  transition with the same  $\hat{z}$  laser polarizations, we find  $C_{net} = \sum_{m_F=-5}^5 C(6, m_F) = -\frac{1}{2}$ . In this way, the tensor polarizability depends on the hyperfine levels. Each set of hyperfine transitions we drive must be studied in this way, taking into account the  $m_F$  selection rule given the polarization of the lasers.

All that is left is to provide an explicit form of  $\alpha_2$  to show its dependence on the reduced electric dipole matrix elements. The tensor polarizability of state  $\xi$  with angular momentum  $J(\xi) = J$  is given by a sum intermediate states over  $k$ ,

$$\alpha_2(\xi) = 4\sqrt{\frac{5J(2J-1)}{6(2J+3)(2J+1)(J+1)}} \sum_k (-1)^{J+J_k} \left\{ \begin{matrix} J & 1 & J_k \\ 1 & J & 2 \end{matrix} \right\} \frac{|\langle J||D||J_k \rangle|^2}{\mathcal{E}_k - \mathcal{E}_\xi}, \quad (6.6)$$

where the term in curly braces is a Wigner 6-j symbol. With this mathematical machinery in place, we now can extract  $\alpha_2$  by measuring the hyperfine level dependence and laser polarization dependence. Since it is difficult to calibrate the laser polarization angle to sufficient precision, we can take data at a range of laser polarization angles and fit the measured polarizabilities to a curve, leaving  $\theta_\varepsilon$  as the independent variable.

Safronova's predicted values for the polarizabilities of the  $6P_{3/2}$  state is included in Table 6.2. Therefore, we expect  $\alpha_2$  to be an order of magnitude smaller than  $\alpha_0$ . Nevertheless, even if we lose an order of magnitude in precision in performing the second step due to a weaker signal, so that our precision is  $\sim 2.5\%$ , we should still be able to clearly resolve  $\alpha_2$ .

### 6.2.4 P-D Linestrengths

Similar to the lifetime model-dependent measurements already accomplished in indium and thallium, a measurement of the polarizability of the  $6P_{3/2}$  state in indium provides a determination of the  $6P$ - $5D$  transition rates. The contributions from the  $\langle 5D_{3/2}||D||6P_{3/2} \rangle$  and  $\langle 5D_{5/2}||D||6P_{3/2} \rangle$  matrix elements constitute over 80% of the

Polarizabilities of Low Lying States in Indium
$\alpha_0(5P_{1/2}) = 61.5(1.3)$
$\alpha_0(6S_{1/2}) = 1056(20)$
$\alpha_0(6P_{1/2}) = 7817(300)$
$\alpha_0(6P_{3/2}) = 10500(400)$
$\alpha_2(6P_{3/2}) = -1432(45)$

Table 6.2: Theoretical polarizabilities (in a.u.) in indium from [29]. Note that the magnitude increases for higher energy states.

total magnitude of both sums ( $|\alpha(6P_{3/2})| + |\alpha(6S_{1/2})|$ ). While not quite as dominating as the 6P terms in the  $\alpha(5P_{1/2}) - \alpha(6S_{1/2})$  sums, this is still enough to extract the  $6P_{3/2} - 5D$  matrix elements. Because of other strong transition channels to the  $5P_{1/2;3/2}$  states, these do not correspond to measurements of the 5D state lifetimes. However, these particular linestrengths cannot be determined from lifetime measurements and so have not been experimentally measured. Therefore, this experiment would provide the first experimental test of the atomic theory predictions for these values.

## 6.3 Further Options in Thallium

An exactly analogous experiment to the one proposed above may be performed in thallium. The 410 nm laser would be replaced by a 378 nm laser, and the 1291 nm laser would be replaced by a 1301 nm laser. The two step excitation in thallium is currently operating in another experiment in the Majumder lab, and the lasers, especially the IR laser, are quite robust. It should not be particularly hard to place thallium in the crucible and move the lasers across the lab. The rest of the optics could stay the same. Although the IR laser currently in use in the thallium two step excitation experiment could be tuned to the indium 1343 nm line ( $6S_{1/2} \rightarrow 6P_{1/2}$ ), it can not reach the analogous  $7S_{1/2} \rightarrow 7P_{1/2}$  line in thallium at 1151 nm. While unfortunate, the  $j = 3/2$  state is more interesting anyway, so this is not a large loss. Furthermore, because thallium has a dramatically higher vapor pressure than indium, we should also have the benefit of a much stronger signal in this experiment, making a future determination of  $\alpha_2$  in the  $7P_{3/2}$  state potentially very precise.

### 6.3.1 Probing the 1283 nm ‘Forbidden’ $6P_{1/2} \rightarrow 6P_{3/2}$ M1/E2 Transition

Because of the high vapor pressure in thallium, we can also attempt to probe the “forbidden”  $6P_{1/2} \rightarrow 6P_{3/2}$  transition in thallium. Since  $\Delta l \neq \pm 1$  for this transition, it cannot be driven by an electric dipole (E1). However, this transition can occur by

means of a magnetic dipole (M1) or electric quadrupole (E2), albeit with a greatly suppressed rate. We can only circumvent this rate suppression by increasing the optical depth of the sample of atoms. In a vapor cell, this is easy: we simply turn up the oven temperature. However, in the atomic beam, this is significantly harder.

In order to perform the completed experiment in indium, though, we had to contend with very much lower vapor pressures. Therefore, we expended significant effort in designing and building an oven that can operate at  $900^{\circ}\text{C}$ . At this temperature, the optical depth of an E1 transition in a thallium atomic beam should be of order 10. Therefore, the M1 transition, which is four orders of magnitude weaker, would have an optical depth of about  $10^{-3}$ , about where we were for the completed experiment.

This means that frequency modulation spectroscopy using a 1283 nm laser in such a beam has the potential for observing this forbidden transition. A Stark shift measurement within this transition has never been accomplished and so would be of great interest. Furthermore, by measuring the increased amplitude of the FM signal, we can measure the Stark-induced amplitude in this transition. The increased transition rate comes about because the electric field mixes both  $P$  states in the transition with nearby  $S$  and  $D$  states, states to which the principle states have strong E1 transitions. While the state mixing is relatively weak, the E1 transition is sufficiently strong to contribute a significant and measurable transition rate. This measurement is also attractive because the M1 transition rate does not derive from matrix elements that are only known imprecisely. Therefore, by simply tuning between the hyperfine levels, we can use the amplitude of the M1 transition as a calibration of the E2 transition amplitude measurement. This makes comparison with the theory of the E2 transition very much easier.

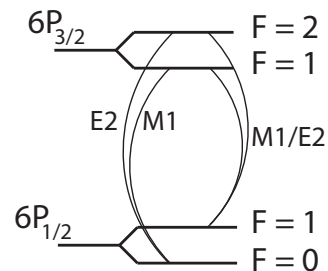


Figure 6.6: A diagram of the  $6P_{1/2} \rightarrow 6P_{3/2}$  forbidden transition.

# Appendix A

## Atomic Units

During any investigation into atomic physics, messy unit conversions are bound to arise. This section is intended to elucidate the origin of these difficulties and guide the reader through some pertinent conversions. All of this information may be found in an atomic physics reference such as [35].

Most atomic theory is calculated in the aptly named atomic units. In this system of natural units four quantities are taken to be 1:

Dimension	Quantity	Symbol
Mass	Electron Mass	$m_e$
Charge	Elementary Charge	$e$
Angular Momentum	Planck's Constant (Reduced)	$\hbar$
Electric Constant	Coulomb Force Constant	$1/(4\pi\epsilon_0)$

Table A.1: The four quantities taken to be one in atomic units.

Dimension	Quantity	Symbol
Length	Bohr Radius	$a_0 = \frac{\hbar}{m_e c \alpha}$
Energy	Hartree	$E_h = \frac{\hbar c \alpha}{a_0}$
Magnetic Moment	Twice Bohr Magnetron	$2\mu_B = \frac{e\hbar}{m_e}$

Table A.2: Units in which other dimensions are measured. Note that these all have numerical values of one given their definition in terms of the relevant quantities assumed to be one.

Note that dimensionless quantities like the fine structure constant  $\alpha = \frac{e^2}{(4\pi\epsilon_0)\hbar c} \approx 1/137$  are necessarily unchanged by any change in units. This choice of units results in convenient units of measurement for common dimensions like length (see Table A.2) and also results in some nice values for quantities commonly used in atomic systems. For examples, see Table A.3.

Quantity	Symbol	Value in Atomic Units
Speed of Light	$c$	$1/\alpha \approx 137$
Electron Radius	$r_e$	$\alpha^2 \approx 5.33 * 10^{-5}$
Proton Mass	$m_p$	1836

Table A.3: Physical quantities that take convenient values in atomic units.

These are atomic units. Atomic polarizability, then, is measured in units of  $a_0^3$  in atomic units. In our experiment, however, we measure polarizability in the metric units:  $\frac{\text{kHz}}{(\text{kV/cm})^2}$ . Technically, this is not the metric polarizability, which should be  $\frac{\text{Energy}}{(\text{Electric Field})^2}$ ; however, the conversion from frequency to energy through Plank's constant results in simply numeric factors since  $\hbar = 1$  in atomic units. Therefore we list the following useful conversions in Table A.4.

Conversion
1 a.u. = $1 a_0^3$
1 a.u. = $1.48187 * 10^{-25} \text{ cm}^3$
1 a.u. = $0.245803 \frac{\text{kHz}}{(\text{kV/cm})^2}$

Table A.4: Useful conversions for calculating atomic polarizabilities.



# Appendix B

## Other Broadening Mechanisms

Here, we discuss the broadening mechanisms glossed in 2.2.2. We follow [34], and show that the theoretical magnitudes of these effects are, in fact, much smaller than the other sources of line broadening.

### Laser Line-Width Broadening

Even if the atomic resonance were a delta function, the experimenter would observe a resonance width if the laser driving the transition is not purely mono-chromatic. Since all lasers emit light along a distribution of frequencies, even the delta function atomic resonance will be driven by a laser if its nominal frequency within a bandwidth of the resonance at  $\omega_0$ . For our laser, after extensive thermal and vibrational stabilization techniques, we achieve an RMS fast jitter in frequency of  $\sim 1$  MHz. Therefore, the laser line width broadening is taken to be  $\Gamma_l \approx 2$  MHz.

### Pressure Broadening

Two atoms in close proximity will interact such that each atom's energy levels will shift as a function of the distance between the atoms. Following [43], this interaction can be shown to result in a broadened absorption profile which is a Lorentzian of width (FWHM)

$$\Gamma_p = 4p_b\sigma_b\sqrt{\frac{2}{\pi\mu kT}}, \quad (\text{B.1})$$

where  $\sigma_b$  is the collisional cross section,  $p_b$  is the pressure of the gas, and  $\mu$  is the reduced mass of the two colliding atoms.

Previous thesis student Antonio Lorenzo crunches the numbers in [43] to show that, in our vapor cell, pressure broadening is only of order  $\Gamma_p \approx 10$  kHz. Our atomic beam, on the other hand, does not have a statistical distribution of velocities, since the atoms are at very low density and are well collimated. Therefore, we must treat it like a sample with zero pressure, and so we expect no pressure broadening in laser absorption that occurs in the atomic beam. The background gas pressure is completely negligible, with a mean free path in the tens to hundreds of meters.

### Transit-Time Broadening

The finite time of interaction between the laser and the atoms results in a resonance broadening. The laser's electric field can only drive oscillations in the atoms for as long as the atoms are exposed to the radiation. Thus the atoms' oscillations in time may be approximated by a rectangular pulse multiplying the sinusoidal oscillation. While in frequency space, the sinusoid is a delta function, the rectangular pulse introduces a frequency spread. This square pulse has a duration dependent only on the velocity,  $v$ , of that atoms and the collimation width,  $d$ , of the laser:  $\tau = d/v$ . We quantify the frequency spread due to the interaction time  $\tau$  by taking the Fourier transform of the atomic oscillation,  $x(t) = \begin{cases} x_0 \cos \omega_0 t & : 0 < t < \tau \\ 0 & : \text{Otherwise} \end{cases}$ .

$$A(\omega) = \frac{1}{\sqrt{2\pi}} \int_0^\tau x_0 \cos \omega_0 t e^{-i\omega t} dt \quad (\text{B.2})$$

This results in an intensity spectrum  $I(\omega) = A^*A$  near  $\omega_0$

$$I(\omega) \propto \tau^2 \frac{\sin^2 a}{a^2} = \tau^2 \text{sinc}^2 a \quad (\text{B.3})$$

where  $a \equiv (\omega - \omega_0)\tau/2$ .  $\text{sinc}(a)$  goes to 0 for  $a = \pi$  so  $I(\omega)$  goes to 0 for  $(\omega - \omega_0) = \frac{2\pi}{\tau}$ . Therefore, since the full width *in frequency* of  $I(\omega)$  is  $\Delta f = \frac{2}{\tau}$ , we can simply say that the additional broadening due to the finite transit time of the atom in the laser field is

$$\Gamma_t = \Delta f/2 = \frac{1}{\tau}. \quad (\text{B.4})$$

To quantify this, we need only find the transit time itself. As can be found in any general overview of atomic beam physics such as provided in [35], the root mean square velocity of atoms in a vapor cell or atomic beam is<sup>1</sup>

$$v_{rms} = \left\{ \begin{array}{l} \sqrt{\frac{3}{2}} : \text{Vapor Cell} \\ \sqrt{2} : \text{Atomic Beam} \end{array} \right\} \sqrt{\frac{2kT}{m}}, \quad (\text{B.5})$$

where  $T$  is the temperature of the beam in Kelvin and  $M$  is the atomic mass in a.m.u. of the atoms of the beam. This gives the root mean square velocities for indium.

$$v_{rms} \simeq \left\{ \begin{array}{l} 480 \frac{m}{s} : \text{Vapor Cell} \\ 550 \frac{m}{s} : \text{Atomic Beam} \end{array} \right.$$

For our 1 mm diameter laser, we therefore have a typical atom-laser interaction time of

$$\tau \simeq \left\{ \begin{array}{l} 2.1 \mu s : \text{Vapor Cell} \\ 1.8 \mu s : \text{Atomic Beam} \end{array} \right.$$

---

<sup>1</sup>This is being sloppy with notation as we have taken the FWHM to be our figure of width; however, since this ends up being negligible, we carry through with the more intuitive calculation.

We now can simply apply Eq. (B.4) to find the additional resonance width due to transit time broadening.

$$\Gamma_t \simeq \begin{cases} 480kHz & : \text{Vapor Cell} \\ 550kHz & : \text{Atomic Beam} \end{cases} \quad (\text{B.6})$$

### Saturation Broadening

The last broadening mechanism considered is power or saturation broadening. At high laser power on resonance, a substantial proportion of the atoms are in an excited state at any particular time. With fewer (approaching 1/2) of the atoms in the ground state able to be excited, the absorption of the laser light near resonance is less than what would otherwise be expected. With the laser farther from resonance, the probability of absorption is already low enough that only an insignificant number of atoms are excited, even at high power. Therefore, there is little to no decrease in absorption from the expected value. Reducing on-resonance absorption while preserving the less frequent off-resonance absorption results in a lower resonance peak height with a wider FWHM (see Fig. B.1). It can be shown [35] that the fractional increase in line

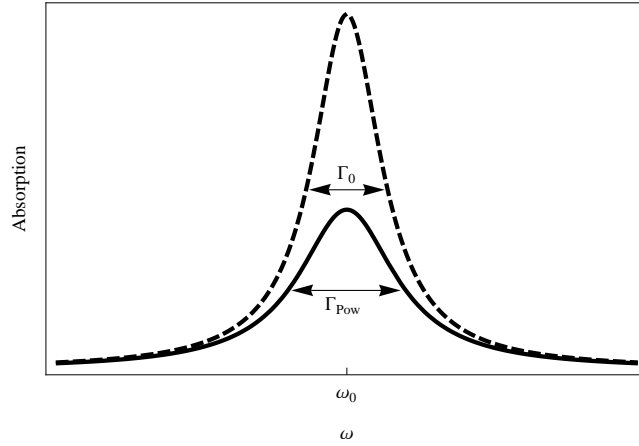


Figure B.1: A comparison of a power broadened resonance profile (solid) and normal resonance profile (dashed) near a resonance at  $\omega_0$ . Absorption reduction is most pronounced nearest the resonance.

width due to power broadening is

$$\frac{\Gamma_{P.B.}}{\Gamma_0} = \sqrt{1 + \frac{I}{I_{sat}}} \quad (\text{B.7})$$

where  $I$  is the intensity of the laser beam driving the atomic resonance, and  $I_{sat}$  is the saturation intensity given by

$$I_{sat} = \frac{\pi}{3} \frac{hc}{\lambda^3 \tau} \quad (\text{B.8})$$

$\tau$  is the lifetime of the excited state, which implies that  $\tau = \Gamma_{nat}^{-1}$  where  $\Gamma_{nat}$  is the natural line width of the resonance. For our setup,  $I_{sat} = 4300 \frac{mW}{mm^2}$ . This results in a certainly negligible 0.012% or  $\frac{12kHz}{100MHz}$  increase in line width due to power.

# Appendix C

## Frequency Modulated Fabry-Pérot

We derive the output of a Fabry-Pérot interferometer given a frequency modulated laser input. We find that the output intensity is a sum of Airy functions, one centered at each frequency component of the laser.

The electric field incident on the Fabry-Pérot is frequency modulated:

$$\tilde{E}_1 = E_0 e^{i(\omega_c t + \beta \sin(\omega_m t))}, \quad (\text{C.1})$$

where  $\omega_c = 730,673$  GHz is the carrier frequency of the laser, and  $\omega_m = 100$  MHz is the modulation frequency. Using the Jacobi-Anger relation, this can be reexpressed as

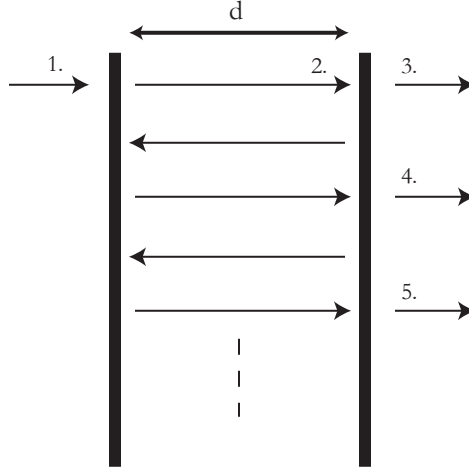
$$\tilde{E}_1 = E_0 e^{i\omega_c t} \sum_{n=-\infty}^{\infty} J_n(\beta) e^{in\omega_m t}. \quad (\text{C.2})$$

Entering and crossing the Fabry-Pérot cavity once results in the electric field

$$\tilde{E}_2 = E_0 e^{i\omega_c t} \sum_{n=-\infty}^{\infty} J_n(\beta) \tilde{t} e^{ik_n d} e^{in\omega_m t}, \quad (\text{C.3})$$

where  $k_n$  is the wavenumber of the  $n^{\text{th}}$  sideband, and  $\tilde{t}$  is the complex transmission coefficient defined through the transmittance  $T$  and the phase shift  $\varphi_t$  of the transmitted light,  $\tilde{t} = \sqrt{T} e^{i\varphi_t}$ . The complex coefficient of reflection is defined similarly. It is worth noting that, across the frequency range over which we sweep, we can and do assume that  $\tilde{t}$  and  $\tilde{r}$  are constant.

Since  $k_n d$  is the phase shift picked up by the laser by traveling a distance  $d$ , I define the phase shift  $\Delta_n = k_n d$ . Therefore, the electric fields at positions 2 and 3 may be written as

Figure C.1: Schematic of a Fabry-Pérot cavity of length  $d$ .

$$\tilde{E}_2 = E_0 e^{i\omega c t} \tilde{t} \sum_{n=-\infty}^{\infty} J_n(\beta) e^{i\Delta_n} e^{in\omega_m t} \quad (\text{C.4})$$

$$\tilde{E}_3 = E_0 e^{i\omega c t} \tilde{t}^2 \sum_{n=-\infty}^{\infty} J_n(\beta) e^{i\Delta_n} e^{in\omega_m t}. \quad (\text{C.5})$$

Between position 3 and position 4, the electric field components undergo two reflections, adding two factors of the complex coefficient of reflection  $\tilde{r}$ , and they pick up a phase of  $2\Delta_n$  from crossing the cavity twice. Therefore,

$$\tilde{E}_4 = E_0 e^{i\omega c t} \tilde{t}^2 \tilde{r}^2 \sum_{n=-\infty}^{\infty} J_n(\beta) e^{3i\Delta_n} e^{in\omega_m t}, \quad (\text{C.6})$$

and similarly,

$$\tilde{E}_5 = E_0 e^{i\omega c t} \tilde{t}^2 \tilde{r}^4 \sum_{n=-\infty}^{\infty} J_n(\beta) e^{5i\Delta_n} e^{in\omega_m t}. \quad (\text{C.7})$$

Adding up all transmitted beams gives the total transmitted electric field.

$$\begin{aligned} \tilde{E}_t &= \tilde{E}_3 + \tilde{E}_4 + \tilde{E}_5 + \dots \\ &= E_0 e^{i\omega c t} \tilde{t}^2 \sum_{q=0}^{\infty} \left[ \tilde{r}^{2q} \sum_{n=-\infty}^{\infty} (J_n(\beta) e^{i(2q+1)\Delta_n} e^{in\omega_m t}) \right] \end{aligned} \quad (\text{C.8})$$

Now, by rearranging terms and interchanging the order of summation, the summation over  $q$  is a geometric series, which is easily evaluated.

$$\begin{aligned}
\tilde{E}_t &= E_0 e^{i\omega_c t} \tilde{t}^2 \sum_{q=0}^{\infty} \sum_{n=-\infty}^{\infty} J_n(\beta) \tilde{r}^{2q} e^{i(2q+1)\Delta_n} e^{in\omega_m t} \\
&= E_0 e^{i\omega_c t} \tilde{t}^2 \sum_{n=-\infty}^{\infty} \sum_{q=0}^{\infty} J_n(\beta) \tilde{r}^{2q} e^{i(2q+1)\Delta_n} e^{in\omega_m t} \\
&= E_0 e^{i\omega_c t} \tilde{t}^2 \sum_{n=-\infty}^{\infty} \left[ J_n(\beta) e^{i\Delta_n} e^{in\omega_m t} \sum_{q=0}^{\infty} \left[ (\tilde{r} e^{i\Delta_n})^2 \right]^q \right] \\
&= E_0 e^{i\omega_c t} \tilde{t}^2 \sum_{n=-\infty}^{\infty} J_n(\beta) e^{i\Delta_n} e^{in\omega_m t} \frac{1}{1 - \tilde{r}^2 e^{2i\Delta_n}}. \tag{C.9}
\end{aligned}$$

Given the relation between electric field and intensity,

$$I = \frac{1}{2} \epsilon_0 c \tilde{E} \tilde{E}^*, \tag{C.10}$$

we now calculate the intensity of a frequency modulated laser that passes through a Fabry-Pérot cavity.

$$\begin{aligned}
I &= \frac{1}{2} \epsilon_0 c \left| E_0 e^{i\omega_c t} \tilde{t}^2 \sum_{n=-\infty}^{\infty} \frac{J_n(\beta) e^{i\Delta_n}}{1 - \tilde{r}^2 e^{2i\Delta_n}} e^{in\omega_m t} \right|^2 \\
&= I_0 T^2 \left| \sum_{n=-\infty}^{\infty} \frac{J_n(\beta) e^{i\Delta_n}}{1 - \tilde{r}^2 e^{2i\Delta_n}} e^{in\omega_m t} \right|^2, \tag{C.11}
\end{aligned}$$

where we identify  $I_0 = \frac{1}{2} \epsilon_0 c E_0^2$  as the intensity of the incident laser and use the relation  $|\tilde{t}|^2 = T$ . Rewriting the modulus squared of the sum as the product of two sums, we then break apart the expression into a sum over square-terms and a sum over cross-terms. To avoid confusion with the subscript  $m$  for modulation, the sums will be indexed with  $n$  and  $l$ .

$$\begin{aligned}
I &= I_0 T^2 \left( \sum_{n=-\infty}^{\infty} \frac{J_n(\beta) e^{i\Delta_n}}{1 - \tilde{r}^2 e^{2i\Delta_n}} e^{in\omega_m t} \right) \left( \sum_{l=-\infty}^{\infty} \frac{J_l(\beta) e^{-i\Delta_l}}{1 - \tilde{r}^{*2} e^{-2i\Delta_l}} e^{-il\omega_m t} \right) \\
&= I_0 T^2 \left[ \sum_{n=-\infty}^{\infty} \frac{J_n^2(\beta)}{(1 - \tilde{r}^2 e^{2i\Delta_n}) (1 - \tilde{r}^{*2} e^{-2i\Delta_n})} + \right. \\
&\quad \left. + \sum_{\substack{n, l = -\infty \\ n \neq l}}^{\infty} \frac{J_n(\beta) J_l(\beta) e^{i(\Delta_n - \Delta_l)}}{(1 - \tilde{r}^2 e^{2i\Delta_n}) (1 - \tilde{r}^{*2} e^{-2i\Delta_l})} e^{i(n-l)\omega_m t} \right]. \tag{C.12}
\end{aligned}$$

These two sums are treated separately: ( $I = S_1 + S_2$ ).  $S_1$  is shown to be exactly equal to a sum of Airy functions centered at each of the sidebands with magnitudes given by  $J_n^2(\beta)$ .

$$\begin{aligned} S_1 &= I_0 T^2 \sum_{n=-\infty}^{\infty} \frac{J_n^2(\beta)}{(1 - \tilde{r}^2 e^{2i\Delta_n})(1 - \tilde{r}^2 e^{-2i\Delta_n})} \\ &= I_0 T^2 \sum_{n=-\infty}^{\infty} \frac{J_n^2(\beta)}{1 - \tilde{r}^2 e^{2i\Delta_n} - \tilde{r}^{*2} e^{-2i\Delta_n} + \tilde{r}^2 \tilde{r}^{*2}}. \end{aligned}$$

Recalling the definition of the complex coefficient of reflection,  $\tilde{r} = \sqrt{R}e^{i\varphi_r}$  where  $R$  is the reflectivity of the mirror and  $\varphi_r$  is the phase shift of the reflected beam due to the reflection, so

$$\begin{aligned} \tilde{r}^2 e^{2i\Delta_n} + \tilde{r}^{*2} e^{-2i\Delta_n} &= 2\Re\{\tilde{r}^2 e^{2i\Delta_n}\} \\ &= 2\Re\{R e^{2i(\varphi_r + \Delta_n)}\} \\ &= 2R \cos(2(\varphi_r + \Delta_n)), \end{aligned}$$

and so,

$$\begin{aligned} S_1 &= I_0 T^2 \sum_{n=-\infty}^{\infty} \frac{J_n^2(\beta)}{1 + R^2 - 2R \cos(2(\varphi_r + \Delta_n))} \\ &= I_0 T^2 \sum_{n=-\infty}^{\infty} \frac{J_n^2(\beta)}{1 + R^2 - 2R(1 - \sin^2(\varphi_r + \Delta_n))} \\ &= \sum_{n=-\infty}^{\infty} J_n^2(\beta) \frac{I_0 T^2}{(1 - R)^2 + 4R \sin^2(\varphi_r + \Delta_n)}. \end{aligned}$$

Defining  $F = \frac{4R}{(1-R)^2}$ , using  $R + T = 1$ , and plugging in for  $\Delta_n = k_n d$ ,

$$S_1 = \sum_{n=-\infty}^{\infty} J_n^2(\beta) \frac{I_0}{1 + F \sin^2(k_n d + \varphi_r)}, \quad (\text{C.13})$$

which is exactly a sum of Airy functions. The phase  $\varphi_r$  may be dropped, as it uniformly shifts the forest of peaks by a constant, and we are only concerned with the intensity as a function of frequency. As for the second sum,

$$S_2 = I_0 T^2 \sum_{\substack{n, l = -\infty \\ n \neq l}}^{\infty} \frac{J_n(\beta) J_l(\beta) e^{i(\Delta_n - \Delta_l)}}{(1 - \tilde{r}^2 e^{2i\Delta_n})(1 - \tilde{r}^{*2} e^{-2i\Delta_l})} e^{i(n-l)\omega_m t}. \quad (\text{C.14})$$

Since  $n \neq l$ , all terms in  $S_2$  will oscillate at some non-zero integer multiple of the modulation frequency  $\omega_m = 100 \text{ MHz}$ . Our Thorlabs PDA55 photodiode has a bandwidth of 10 MHz, so these terms are time averaged to zero. Therefore, without the aid of an RF lock-in amplifier,

$$S_2 = 0, \quad (\text{C.15})$$

and so the detected intensity of the FM laser through the Fabry-Pérot is

$$I_{transmitted} = \sum_{n=-\infty}^{\infty} J_n^2(\beta) \frac{I_0}{1 + F \sin^2(k_n d)}. \quad (\text{C.16})$$



# Appendix D

## FM Signal Derivation

Herein, we fill out the steps skipped in sections 3.2 and sect:2fDemod. We start from Eq. (3.6).

### D.1 1f Signal

Cross-terms with  $l = n - 1$  or  $l = n + 1$  will oscillate at the modulation frequency. By using a lock-in amplifier, we can pick out only these terms, so it is worth looking at the analytic form of the ‘1f’ signal.

$$|\tilde{E}_T(t)|_{1f}^2 = E_0^2 \sum_{n=-\infty}^{\infty} (J_n T_n^* e^{-in\omega_m t} J_{n-1} T_{n-1} e^{-i(n-1)\omega_m t}) + \dots$$

$$\sum_{n=-\infty}^{\infty} (J_n T_n^* e^{-in\omega_m t} J_{n+1} T_{n+1} e^{-i(n+1)\omega_m t}) \quad (\text{D.1})$$

In the first sum, we switch indices to  $n' = n + 1$  and drop the primes. Then we combine the time dependences and combine into one sum, arriving at

$$|\tilde{E}_T(t)|_{1f}^2 = E_0^2 \sum_{n=-\infty}^{\infty} J_n J_{n+1} (T_{n+1}^* T_n e^{-i\omega_m t} + T_n^* T_{n+1} e^{i\omega_m t}). \quad (\text{D.2})$$

We now split the sum in to two halves so that we can re-express this as a sum over positive  $n$ .

$$|\tilde{E}_T(t)|_{1f}^2 = E_0^2 \sum_{n=-\infty}^{-1} J_n J_{n+1} (T_{n+1}^* T_n e^{-i\omega_m t} + T_n^* T_{n+1} e^{i\omega_m t}) + \dots$$

$$E_0^2 \sum_{n=0}^{\infty} J_n J_{n+1} (T_{n+1}^* T_n e^{-i\omega_m t} + T_n^* T_{n+1} e^{i\omega_m t}). \quad (\text{D.3})$$

In the first sum, we switch indices to  $n' = -n - 1$  and drop the primes. Then we combine into one sum, arriving at

$$|\tilde{E}_T(t)|_{1f}^2 = E_0^2 \sum_{n=0}^{\infty} \left( J_{-n} J_{-n-1} T_{-n}^* T_{-n-1} e^{-i\omega_m t} + J_{-n} J_{-n-1} T_{-n-1}^* T_{-n} e^{i\omega_m t} + \dots \right. \\ \left. J_n J_{n+1} T_{n+1}^* T_n e^{-i\omega_m t} + J_n J_{n+1} T_n^* T_{n+1} e^{i\omega_m t} \right). \quad (\text{D.4})$$

Now we note the following property of Bessel functions  $J_{-n}(x) = (-1)^n J_n(x)$  and conclude that  $J_{-n} J_{-n-1} = -J_n J_{n+1}$ . Thus we write

$$|\tilde{E}_T(t)|_{1f}^2 = E_0^2 \sum_{n=0}^{\infty} J_n J_{n+1} \left[ (T_{n+1}^* T_n - T_{-n}^* T_{-n-1}) e^{-i\omega_m t} + (T_n^* T_{n+1} - T_{-n-1}^* T_{-n}) e^{i\omega_m t} \right] \quad (\text{D.5})$$

All we have left to do is understand these odd combinations of the transmission function. We start with the definition  $T_n = e^{\delta_n - i\phi_n}$ . We assume that  $\delta(\omega)$  and  $\phi(\omega)$  are slowly varying functions. This assumption can take two forms which for us are identical, namely  $|\delta_0 - \delta_n| \ll 1$  or  $|\delta_n - \delta_{n+1}| \ll 1$ . Previous treatments of FM modulation tend to prefer the former, so we use this assumption. [39] In any case, we also assume  $|\phi_0 - \phi_{n+1}| \ll 1$ . We will use the assumption about  $\delta$  by rewriting the transmission function as  $T_n = e^{-\delta_0} e^{\delta_0 - \delta_n - i\phi_n}$ . With this we can proceed.

$$\begin{aligned} T_{n+1}^* T_n - T_{-n}^* T_{-n-1} &= e^{-2\delta_0} \left( e^{\delta_0 - \delta_{n+1} + i\phi_{n+1}} e^{\delta_0 - \delta_n - i\phi_n} - e^{\delta_0 - \delta_{-n} + i\phi_{-n}} e^{\delta_0 - \delta_{-n-1} - i\phi_{-n-1}} \right) \\ &= e^{-2\delta_0} \left( e^{(\delta_0 - \delta_{n+1} + \delta_0 - \delta_n) + i(\phi_{n+1} - \phi_n)} - e^{(\delta_0 - \delta_{-n} + \delta_0 - \delta_{-n-1}) + i(\phi_{-n} - \phi_{-n-1})} \right) \\ &= e^{-2\delta_0} \left[ ((1 + \delta_0 - \delta_{n+1} + \delta_0 - \delta_n)(\cos(\phi_{n+1} - \phi_n) + i \sin(\phi_{n+1} - \phi_n))) - \dots \right. \\ &\quad \left. ((1 + \delta_0 - \delta_{-n} + \delta_0 - \delta_{-n-1})(\cos(\phi_{-n} - \phi_{-n-1}) + i \sin(\phi_{-n} - \phi_{-n-1}))) \right] \\ &= e^{-2\delta_0} ((\delta_{-n} - \delta_n + \delta_{-n-1} - \delta_{n+1}) + i(\phi_{n+1} - \phi_n + \phi_{-n-1} - \phi_{-n})). \quad (\text{D.6}) \end{aligned}$$

Similarly,

$$T_n^* T_{n+1} - T_{-n-1}^* T_{-n} = e^{-2\delta_0} ((\delta_{-n} - \delta_n + \delta_{-n-1} - \delta_{n+1}) + i(-\phi_{n+1} + \phi_n - \phi_{-n-1} + \phi_{-n})). \quad (\text{D.7})$$

Now we can evaluate Eq. (D.5). We split the complex exponentials into real sines and cosines to reveal explicitly the in phase and quadrature components.

$$|E_T(t)|_{1f}^2 = E_0^2 e^{-2\delta_0} \sum_{n=0}^{\infty} J_n J_{n+1} \left[ 2(\delta_{-n} - \delta_n + \delta_{-n-1} - \delta_{n+1}) \cos(\omega_m t) + \dots \right. \\ \left. 2(\phi_{n+1} - \phi_n + \phi_{-n-1} - \phi_{-n}) \sin(\omega_m t) \right] \quad (\text{D.8})$$

Finally, we can write down the output of our lock-in amplifier, which effectively multiplies the signal by  $\cos(\omega_m + \theta_d)$  and integrates, resulting in

$$I_{demod}^{1f}(t) = I_0 e^{-2\delta_0} \sum_{n=0}^{\infty} J_n J_{n+1} \left[ (\delta_{-n} - \delta_n + \delta_{-n-1} - \delta_{n+1}) \cos(\theta_d) + \dots \right. \\ \left. (\phi_{n+1} - \phi_n + \phi_{-n-1} - \phi_{-n}) \sin(\theta_d) \right]. \quad (\text{D.9})$$

## D.2 2f Signal

For each value of  $n$ , we obtain  $2\omega_m$  oscillatory terms if  $l = n - 2$  or if  $l = n + 2$ . In these cases, we obtain

$$|\tilde{E}_T(t)|_{2f}^2 = E_0^2 \sum_{n=-\infty}^{\infty} (J_n T_n^* e^{-in\omega_m t} J_{n-2} T_{n-2} e^{i(n-2)\omega_m t}) + \dots \\ \sum_{n=-\infty}^{\infty} (J_n T_n^* e^{-in\omega_m t} J_{n+2} T_{n+2} e^{i(n+2)\omega_m t}). \quad (\text{D.10})$$

The first sum's indices are recast to  $n' = n + 2$ . Dropping the primes and combining terms,

$$|\tilde{E}_T(t)|_{2f}^2 = E_0^2 \sum_{n=-\infty}^{\infty} J_n J_{n+2} (T_{n+2}^* T_n e^{-2i\omega_m t} + T_n^* T_{n+2} e^{2i\omega_m t}). \quad (\text{D.11})$$

Now we wish to re-express this as a sum over positive  $n$ .

$$|\tilde{E}_T(t)|_{2f}^2 = E_0^2 \left[ \sum_{n=-\infty}^{-2} J_n J_{n+2} (T_{n+2}^* T_n e^{-2i\omega_m t} + T_n^* T_{n+2} e^{2i\omega_m t}) + \dots \\ J_{-1} J_1 (T_1^* T_{-1} e^{-2i\omega_m t} + T_{-1}^* T_1 e^{2i\omega_m t}) + \dots \\ \sum_{n=0}^{\infty} J_n J_{n+2} (T_{n+2}^* T_n e^{-2i\omega_m t} + T_n^* T_{n+2} e^{2i\omega_m t}) \right]. \quad (\text{D.12})$$

The indices of the first sum are rewritten as  $n' = -n - 2$ . Dropping the primes and combining sums, we have,

$$|\tilde{E}_T(t)|_{2f}^2 = E_0^2 \left[ J_{-1} J_1 (T_1^* T_{-1} e^{-2i\omega_m t} + T_{-1}^* T_1 e^{2i\omega_m t}) + \dots \\ \sum_{n=0}^{\infty} (J_{-n} J_{-n-2} (T_{-n}^* T_{-n-2} e^{-2i\omega_m t} + T_{-n-2}^* T_{-n} e^{2i\omega_m t}) + \dots \\ J_n J_{n+2} (T_{n+2}^* T_n e^{-2i\omega_m t} + T_n^* T_{n+2} e^{2i\omega_m t})) \right]. \quad (\text{D.13})$$

Using  $J_{-n} = (-1)^n J_n$ , we have  $J_{-1} = -J_1$  and  $J_{-n} J_{-n-2} = J_n J_{n+2}$ . Therefore, we can combine terms,

$$|\tilde{E}_T(t)|_{2f}^2 = E_0^2 \left[ -J_1^2 (T_1^* T_{-1} e^{-2i\omega_m t} + T_{-1}^* T_1 e^{2i\omega_m t}) + \dots \\ \sum_{n=0}^{\infty} J_n J_{n+2} \left( (T_{-n}^* T_{-n-2} + T_{n+2}^* T_n) e^{-2i\omega_m t} + (T_{-n-2}^* T_{-n} + T_n^* T_{n+2}) e^{2i\omega_m t} \right) \right]. \quad (\text{D.14})$$

We now evaluate the combinations of transmission functions (as in Eqs. (D.6) and (D.7)).

$$\begin{aligned}
T_1^* T_{-1} &= e^{-2\delta_0} [(1 + 2\delta_0 - \delta_1 - \delta_{-1}) + i(\phi_1 - \phi_{-1})] \\
T_{-1}^* T_1 &= e^{-2\delta_0} [(1 + 2\delta_0 - \delta_1 - \delta_{-1}) + i(\phi_{-1} - \phi_1)] \\
T_{-n}^* T_{-n-2} + T_{n+2}^* T_n &= e^{-2\delta_0} [(2 + 4\delta_0 - \delta_n - \delta_{-n} - \delta_{n+2} - \delta_{-n-2}) + \dots \\
&\quad i(\phi_{-n} - \phi_n + \phi_{n+2} - \phi_{-n-2})] \\
T_{-n-2}^* T_{-n} + T_n^* T_{n+2} &= e^{-2\delta_0} [(2 + 4\delta_0 - \delta_n - \delta_{-n} - \delta_{n+2} - \delta_{-n-2}) + \dots \\
&\quad i(-\phi_{-n} + \phi_n - \phi_{n+2} + \phi_{-n-2})]
\end{aligned} \tag{D.15}$$

Now we can expand the complex exponentials into real sine and cosines. Combining terms to associate the in-phase components together and the quadrature components together, we have,

$$\begin{aligned}
|E_T(t)|_{2f}^2 &= E_0^2 e^{-2\delta_0} \left[ 2 \cos(2\omega_m t) \left[ -J_1^2(1 + 2\delta_0 - \delta_1 - \delta_{-1}) + \dots \right. \right. \\
&\quad \left. \left. \sum_{n=0}^{\infty} J_n J_{n+2} (2 + 4\delta_0 - \delta_n - \delta_{-n} - \delta_{n+2} - \delta_{-n-2}) \right] + \dots \right. \\
&\quad \left. 2 \sin(2\omega_m t) \left[ -J_1^2(\phi_1 - \phi_{-1}) + \sum_{n=0}^{\infty} J_n J_{n+2} (\phi_{-n} - \phi_n + \phi_{n+2} - \phi_{-n-2}) \right] \right]. \tag{D.16}
\end{aligned}$$

The output of the lock-in amplifier with reference input of  $2\omega_m$  and demodulation phase  $\theta_d$  is therefore

$$\begin{aligned}
I_{demod}^{2f} &= I_0 \left[ \left( -J_1^2(1 + 2\delta_0 - \delta_1 - \delta_{-1}) + \dots \right. \right. \\
&\quad \left. \left. \sum_{n=0}^{\infty} J_n J_{n+2} (2 + 4\delta_0 - \delta_n - \delta_{-n} - \delta_{n+2} - \delta_{-n-2}) \right) \cos(\theta_d) + \dots \right. \\
&\quad \left. \left( -J_1^2(\phi_1 - \phi_{-1}) + \sum_{n=0}^{\infty} J_n J_{n+2} (\phi_{-n} - \phi_n + \phi_{n+2} - \phi_{-n-2}) \right) \sin(\theta_d) \right] \tag{D.17}
\end{aligned}$$

At this point, we wish to recall our note concerning an arbitrary choice of assumptions before the derivation in Eq. (D.6). Suppose we had made the second assumption, i.e.  $|\delta_n - \delta_{n+1}| \ll 1$ . It can be shown that this assumption results in

an alternative form of the 2f transmission function Eq. (D.16) given by

$$|E_T(t)|_{2f}^2 = E_0^2 \left[ 2 \cos(2\omega_m t) \left[ -J_1^2(1 - \delta_1 - \delta_{-1}) + \cdots \right. \right. \\ \left. \left. \sum_{n=0}^{\infty} J_n J_{n+2} (2 - \delta_n - \delta_{-n} - \delta_{n+2} - \delta_{-n-2}) \right] + \cdots \right. \\ \left. 2 \sin(2\omega_m t) \left[ -J_1^2(\phi_1 - \phi_{-1}) + \sum_{n=0}^{\infty} J_n J_{n+2} (\phi_{-n} - \phi_n + \phi_{n+2} - \phi_{-n-2}) \right] \right]. \quad (\text{D.18})$$

As can be seen by comparison with Eq. (D.16) this amounts to canceling all occurrences of  $\delta_0$ . Starting from Eq. (D.16), if we assume  $\delta_0 \ll 1$  as is the case for us,  $e^{-2\delta_0} \simeq (1 - 2\delta_0)$ . The 1 picks up the entire following expression, while  $-2\delta_0$  will only pick out terms in following that are proportional to unity. This second term precisely cancels all occurrences of  $\delta_0$  within the first term. Thus, in the limit of small absorption, Eq. (D.16) is equivalent to Eq. (D.18) and so the choice between the two assumptions above Eq. (D.6) was, in fact, arbitrary.



# Appendix E

## Non-Ideal Modulation

Herein we explore the manifestations and causes of the non-ideal frequency spectrum of our laser. We expect the peak height of the  $n^{\text{th}}$  sideband in the laser spectrum to be proportional to  $n^{\text{th}}$  Bessel function squared of the modulation depth (see Fig. E.1). In particular, this means that each frequency component should go to zero for a particular modulation depth. However, as we scan the input RF power of the EOM and thus scan the modulation depth of the frequency modulation, we clearly do not extinguish the principle carrier frequency. (see Fig. E.2. From Fig. E.1, we see that the carrier frequency component should go to zero for  $\beta \simeq 2.4$ ).

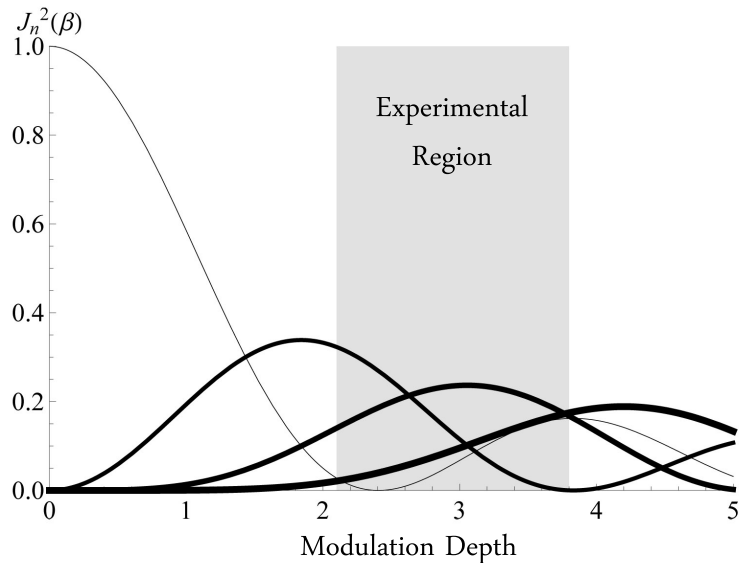


Figure E.1: The first four Bessel functions  $J_n$  for  $n = 0, 1, 2,$  and  $3$ . The boldness level corresponds to the order of the Bessel function. Notice that our experimental region lies well outside of the small- $\beta$  limit. The lower bound of the experimental region is determined by the minimum  $\beta$  at which the third order side band is significant. The upper bound is determined by the maximum input power of our modulator.

The first explanation for this deviation from the Bessel function distribution of frequencies (Eq. (3.3)) is that a component of the laser power is transmitted through the EOM without being modulated. This explains our frequency spectrum including the constant addition to the central carrier peak. Since we want additional zeroth order *intensity*, not amplitude, we replace  $J_0(\beta)$  with  $J'_0(\beta)$ , where

$$J'_0(\beta) = \sqrt{J_0^2(\beta) + d}. \quad (\text{E.1})$$

By taking Fabry-Pérot scans within one free spectral range (a single longitudinal mode), we can extract the frequency spectrum. By doing so over a range of EOM input RF powers, we can extract the frequency components as a function of the modulation depth. This requires converting the EOM input RF power into a modulation depth. The specifications of our New Focus 4001 EOM offer a curve on a semi-log plot of modulation depth versus input RF power that is approximately linear over the relevant range of this experiment. Therefore, we expect the relationship to be exponential. However, the slope of this line is small, and so for ease of fitting, we approximate this relation instead as a quadratic:  $\beta(p) = a_0 + a_1p + a_2p^2$  where  $p$  is the input RF power. With this approximation scheme, we can perform a non-linear least-squares fit to the extracted carrier peak height versus EOM power data using a functional form given by

$$h(p) = AJ_0^2(a_0 + a_1p + a_2p^2) + d. \quad (\text{E.2})$$

After performing this fit, we have the coefficients  $a_0$ ,  $a_1$ , and  $a_2$  with which we can convert the horizontal axis to modulation depth. Unfortunately, these conversion coefficients are not constant across the seven frequency peaks; each frequency component must be fit using its own distinct values of  $a_0$ ,  $a_1$ , and  $a_2$ . This is, on the face of it, absurd, since the frequency components are extracted from a single underlying set of spectra. Therefore, each spectrum should correspond to one modulation depth, not seven depending on the frequency of interest. This indicates that there is more going on here than previously thought. In particular, we find an underlying structure to these inequalities. After taking average values for these coefficients,  $\bar{a}_0$ ,  $\bar{a}_1$ , and  $\bar{a}_2$ , we can describe the inequalities between the seven  $\beta(p)$  relations with only *one* parameter per relation (one would naively expect three per relation). If we define an average modulation depth  $\hat{\beta}(p) = \bar{a}_0 + \bar{a}_1p + \bar{a}_2p^2$ , we can then redefine the Bessel functions as

$$J'_n(\beta) = J_n(\hat{\beta}) + c_n. \quad (\text{E.3})$$

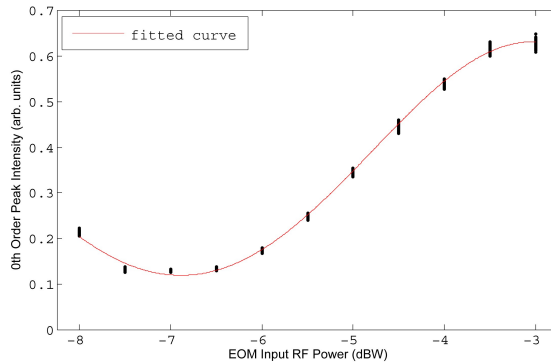


Figure E.2: A plot of zeroth order peak heights versus EOM input RF power. The red line represents the results of a fit using the form of Eq. (E.2)

Note that  $J_n^2(\beta)$  will still go to zero, but at shifted values of  $\beta$ . With this, we can finally fit all seven components assuming a common modulation depth.

$$\begin{aligned} h_0(\hat{\beta}) &= A_0(J_0(\hat{\beta}) + c_0)^2 + d \\ h_n(\hat{\beta}) &= A_n(J_n(\hat{\beta}) + c_n)^2, \text{ for } n = \pm 1, \pm 2, \pm 3 \end{aligned} \quad (\text{E.4})$$

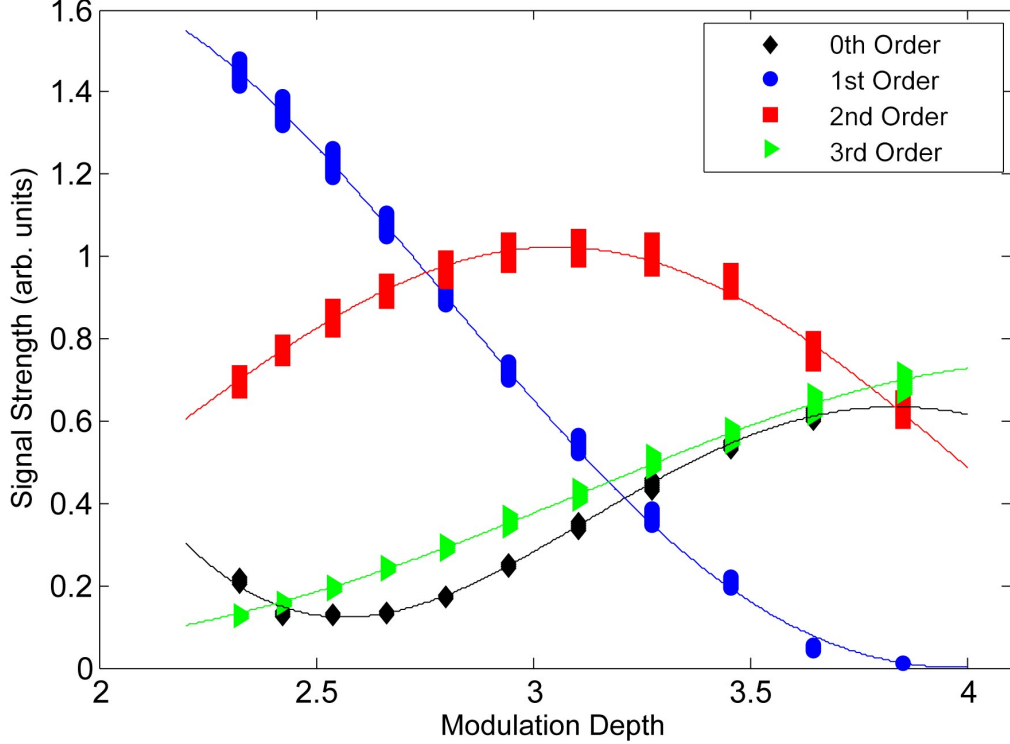


Figure E.3: Four (non-negative detuning) frequency components versus modulation depth.  $d = 0.123$ ,  $c_0 = 0.081$ ,  $c_1 = 0.061$ ,  $c_2 = -0.091$ , and  $c_3 = -0.0008$ .

Having found  $d = 0.123$ , we wish to interpret this as a percent of the laser power that is unmodulated by the EOM. Since our fits, by construction, find that the  $d$  parameter is constant over the range of our fits (from  $\beta = 2.3$  to  $\beta = 3.8$ ), we make the assumption that  $d$  remains independent of  $\beta$  down to low modulation depths. With this assumption in hand, we can go to  $\beta = 0$  and there say that all of the laser power is in the carrier frequency. In the same units, the carrier intensity has a signal strength of  $h_0 = 5.1$ . Therefore, we conclude that about 2.5% of the laser power is transmitted unmodulated by the EOM.

Once we completed these fits, we also looked at the difference in intensity between the two first order sidebands as a measure of the residual amplitude modulation. We do not resolve any difference in intensity between the first order peaks, giving us confidence that our EOM is only phase modulating. This very nice result stands in contrast to a common alternative method for frequency modulating the laser, in which a sinusoidal current is added onto the laser diode current. This is a cheap and

easy way of modulating the laser frequency, but it comes at the cost of strong residual amplitude modulation.

For the data used in these fits, we paid special attention to optimizing the Fabry-Pérot signal, while for the Stark shift data, we were primarily concerned with smooth, fittable peaks. Therefore, we understand the results presented here as a lower bound for the non-ideality of the frequency modulation.

The variation in the  $c_n$  values remains troubling. It is certainly encouraging that the deviation from ideal is characterized by seven rather than twenty-one parameters; however, it remains to show why we should have any non-ideality at all. One likely source is a spatially non-uniform modulation strength of the EOM. Assuming a modulation density inside the electro-optic crystal given by a function  $u_\beta(r, z)$ , if the direction of laser propagation is in the  $\hat{z}$  direction, we identify the modulation depth as the integral,

$$\beta(r) = \int_{z_1}^{z_2} u_\beta(r, z) dz, \quad (\text{E.5})$$

Throughout our analysis, we take the common assumption that  $\beta$  is constant; however, if, in fact, the modulation depth depends on the laser's path through the electro-optic crystal, we can explain the complicated effects found above. Since the laser is itself spread over its own cross section, it does not 'see' a single modulation depth. Therefore, we would certainly not expect the frequency components to go to zero. Furthermore, this could explain our  $c_n$  values as non-trivial parameters characterizing this spatial non-uniformity.

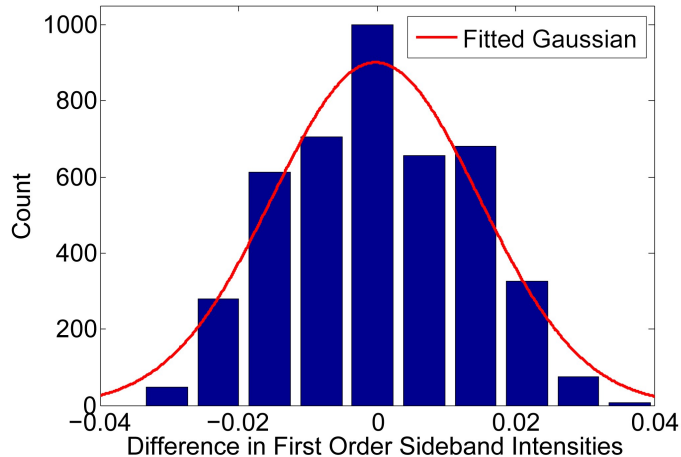


Figure E.4: A histogram of the moving difference between the first order sidebands. The average value for the difference is  $-0.00001(1320)$ .

# Appendix F

## Saturated Absorption Theory

The saturated absorption technique is used to remove Doppler broadening from an absorption signal. This setup fundamentally consists in two counter-propagating laser beams passing through a vapor sample. A more powerful ‘pump’ beam excites most of the atoms as compared to the less intense ‘probe’ beam that is sent to a photodetector. Off resonance, each laser beam may be absorbed by the atoms; however, these atoms are different for each beam. To wit, below resonance only atoms that are moving towards the laser’s source may absorb a photon. Likewise, above resonance, only atoms that are moving in the same direction as the laser may absorb a photon. Since the probe and pump are counter-propagating, this means that, off resonance, different atoms ‘see’ each beam. When the laser is tuned exactly to the resonance frequency, though, atoms that have zero longitudinal velocity (parallel to the laser beams) will see both beams.

Now it becomes important that the pump beam is much more intense, so that it may saturate the sample. It is powerful enough to excite approximately half of all atoms in the sample, which causes a photon to be as likely to cause stimulated emission as it is to be absorbed. The photodiode voltage follows the absorption of the probe beam, so therefore follows the broad absorption profile of an off resonance laser until the laser scans just on resonance. At this frequency, atoms see both lasers, but are most likely to be excited by (and cause an intensity reduction in) the pump laser. Thus the absorption of the probe beam is significantly smaller on resonance. The final line shape is a broad Gaussian dip with small Lorentzian peaks at each resonance.

In our setup, the Doppler broadened Gaussian absorption profile has a width of  $\sim 1.6$  GHz, and the small transmission peaks on resonance are Lorentzians with widths of  $\sim 100$  MHz. We modulate the pump beam with a chopping wheel at  $\sim 3000$  Hz and send the photodiode voltage into a lock-in amplifier (SRS Model SR810). Without the pump beam, the probe purely follows the Gaussian absorption profile, since there is no saturation on resonance. Therefore, the addition of the chopping wheel turns on and off the small Lorentzian peaks at precisely the modulation frequency, so the lock-in amplifier picks out the Lorentzian profiles cleanly.

### Multifrequency saturated absorption

Beyond the standard saturated absorption setup, we utilize an acousto-optic modulator with a reference frequency of  $\delta\omega = 260$  MHz to provide the pump and probe beams. These are mixed with a polarizing beam splitter into two two-color beams, consisting of both  $\omega + \delta\omega$  and  $\omega - \delta\omega$  frequency light (See Fig. F.3 for full optical setup).

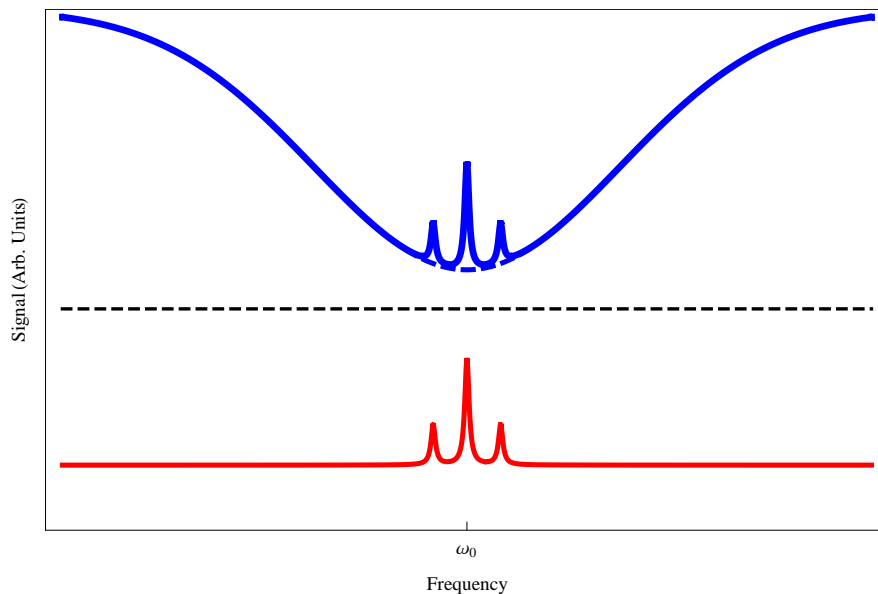


Figure F.1: The probe beam absorption profile (upper) and the demodulated saturated absorption signal (lower).

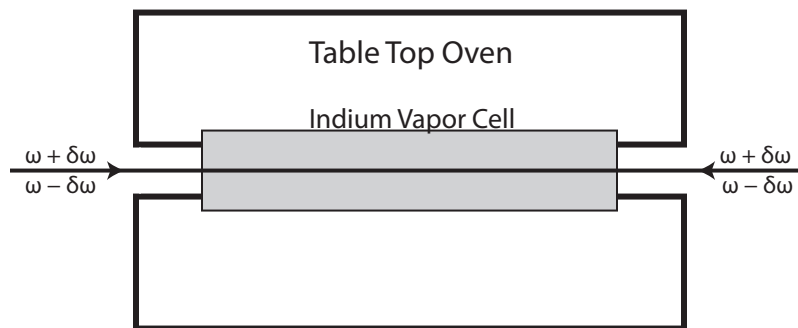


Figure F.2: Diagram of the laser interaction within the vapor cell. Note that both frequencies travel in both directions.

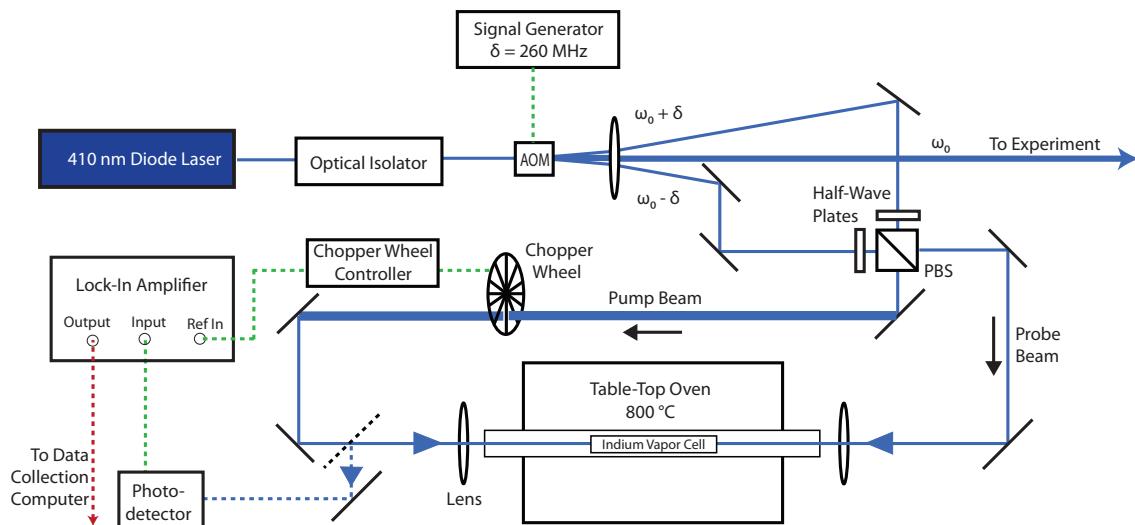
This setup of four beams produces a total of three peaks. As in the basic setup, the counter-propagating  $\omega + \delta\omega$  beams produce a peak at  $\omega_0 + \delta\omega$ , and the  $\omega - \delta\omega$  beams

produce a peak at  $\omega_0 - \delta\omega$ . Note that  $\omega$  refers to the frequency of the laser, which is scanning, while  $\omega_0$  refers to the actual resonance frequency of the  $5P_{1/2} \rightarrow 6S_{1/2}$  transition. Perhaps surprisingly, the interaction between counter-propagating  $\omega + \delta\omega$  and  $\omega - \delta\omega$  laser beams does produce an additional peak at the resonance frequency  $\omega_0$ . The so called 'crossover' peak arises because instead of picking out the class of atoms with zero longitudinal velocity (as the normal peaks do), the setup responds to atoms that have longitudinal velocity. We start with the equation for the Doppler shift,

$$\Delta\omega = -\frac{v}{c}\omega \quad (\text{F.1})$$

where  $v$  is the velocity of the atoms and is positive when the atoms are moving in the same direction as the laser. Atoms with a longitudinal velocity  $v_{\parallel} = \frac{\delta\omega}{\omega_0}c$  will experience the  $\omega_0 + \delta\omega$  light as shifted down to  $\omega_0$  and the  $\omega_0 - \delta\omega$  light as shifted up to  $\omega_0$ . Therefore, the pump beam will saturate the same atoms that the probe beam sees, and so saturation occurs. It turns out that this crossover peak is much larger than either of the two principle peaks, so much so that it requires significant effort in optimizing and aligning the system to resolve the principle peaks. Given the results of the analysis below, we did not want to resolve the principle peaks, opting instead just to use the large crossover peak, as in Fig. 5.2.

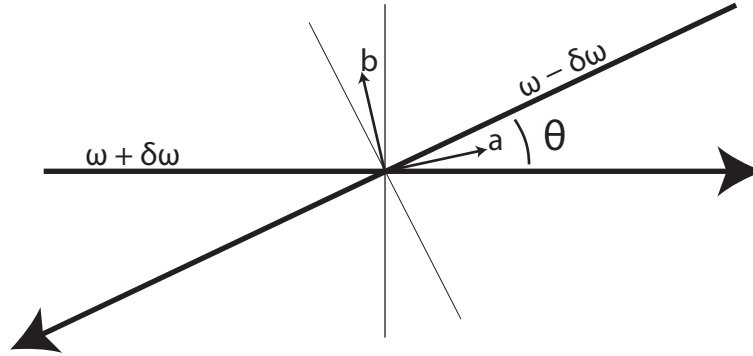
Figure F.3: Saturated Absorption Setup



## Error Analysis

Alignment is never perfect, however, and this causes a change in the frequency of the peaks. Specifically, the probe and pump beams will never be precisely parallel, but will always diverge at some small angle  $\theta$  (see Fig. F.4).

Figure F.4: Diagram of a misaligned setup. The misalignment is exaggerated for clarity.



The crossover peak, which arises due to conjugate-frequency interactions, remains at  $\omega = \omega_0$ . Consider atoms that move with speed  $v$ , not longitudinally, but at an angle  $\theta/2$  as indicated by vector  $\vec{a}$ . These atoms have a speed  $v_{\parallel}^+$  in the direction of the  $\omega_0 + \delta\omega$  beam and speed  $v_{\parallel}^-$  in the direction of the  $\omega_0 - \delta\omega$  beam equal to

$$v_{\parallel}^+ = v_{\parallel}^- = v_{\parallel} = v \cos(\theta/2). \quad (\text{F.2})$$

Therefore, we need only require that the atoms move such that

$$v_{\parallel} = \frac{\delta\omega}{\omega_0} c, \quad (\text{F.3})$$

or, after a small angle expansion, with speed

$$v = \frac{\frac{\delta\omega}{\omega_0} c}{1 - \frac{\theta^2}{4}} \quad (\text{F.4})$$

in the  $\theta/2$  direction. With this velocity, both beams are Doppler shifted onto resonance. Any velocity into or out of the page is allowed.

The smaller principle peaks, which arise from same-frequency interactions, do not remain at the same frequency, however. We again start by requiring the projection of the atoms' velocity onto the two beams to be equal. In this case, this results in a direction of  $\frac{1}{2}(\pi + \theta)$  as indicated by vector  $\vec{b}$ . The speed of these atoms in the direction of the beams is

$$v_{\parallel} = v_{\parallel}^+ = v_{\parallel}^- = v \sin(\theta/2), \quad (\text{F.5})$$

so the Doppler shift is,

$$\begin{aligned}
\Delta\omega &= \frac{v_{\parallel}}{c}\omega_0 \\
&= \frac{v}{c}\sin(\theta/2)\omega_0 \\
\Delta\omega &= \frac{\theta v}{2c}\omega_0
\end{aligned}
\tag{F.6}$$

For atoms with velocity parallel to vector  $\vec{b}$ , each beam appears Doppler shifted by the same amount  $\Delta\omega$  in the same direction. Therefore, the laser may be arbitrarily off resonance as long as the atoms' speed and the lasers' misalignment angle conspire to shift the laser frequency back onto resonance. In practice, the velocity of atoms follows a Boltzmann distribution, so only a fairly small range of velocities (compared to  $c$ ) are present, so only a range of shifts occur. Therefore, a particular oven temperature determines the shift in the principle peaks for a given misalignment angle. Taking the most likely speed at a our given temperature, we can calculate the likely shift due to misalignment, taking the temperature to be  $T = 800^\circ C$  and using the mass of an indium atom  $m = 114.82$  a.m.u.,

$$\begin{aligned}
\bar{v} &= \sqrt{\frac{3k_B T}{m}} \\
&= 487 \frac{m}{s}.
\end{aligned}
\tag{F.7}$$

With a common misalignment angle of  $\theta = 4$  mRad and plugging in for constants and the resonance frequency ( $\omega_0 = 730673$  GHz), we arrive at

$$\overline{\Delta\omega} = 2.4 \text{ MHz}.
\tag{F.8}$$

A convenient cutoff for the maximum speed of atoms in the cell is twice twice the *rms* speed, so, with our setup, it is possible to see shifts up to 5 MHz. Therefore, it is reasonable to assume that at any likely temperatures and alignments, the principle peaks are actually several megahertz off of their ideal values of  $\omega_0 + \delta\omega$  and  $\omega_0 - \delta\omega$ . We had hoped originally that these three peaks could provide additional frequency linearization information; however, due to this sensitivity to misalignment, the three saturated absorption peaks do not make good candidates for frequency linearization.

# Bibliography

- [1] P. A. Vetter, D. M. Meekhof, P. K. Majumder, S. K. Lamoreaux, and E. N. Fortson, Phys. Rev. Lett. **74**, 2658 (1995).
- [2] D. M. Meekhof, P. Vetter, P. K. Majumder, S. K. Lamoreaux, and E. N. Fortson, Phys. Rev. Lett. **71**, 3442 (1993).
- [3] T. P. Emmons, J. M. Reeves, and E. N. Fortson, Phys. Rev. Lett. **51**, 2089 (1983).
- [4] J. H. Hollister, G. R. Apperson, L. L. Lewis, T. P. Emmons, T. G. Vold, and E. N. Fortson, Phys. Rev. Lett. **46**, 643 (1981).
- [5] M. A. Bouchiat and C. C. Bouchiat, Phys. Lett. **48B**, 111 (1974).
- [6] S. C. Doret, Bachelor's thesis, Williams College (2002).
- [7] J. H. Christenson, J. W. Cronin, V. L. Fitch, and R. Turlay, Phys. Rev. Lett. **13**, 138 (1964).
- [8] A. Abashian, K. Abe, K. Abe, I. Adachi, B. S. Ahn, H. Aihara, M. Akatsu, G. Alimonti, K. Aoki, K. Asai, et al., Phys. Rev. Lett. **86**, 2509 (2001).
- [9] S. M. Barr, International Journal of Modern Physics A **8** (1993).
- [10] B. K. Sahoo, B. P. Das, R. K. Chaudhuri, D. Mukherjee, and E. P. Venugopal, Phys. Rev. A **78**, 010501 (2008).
- [11] B. C. Regan, E. D. Commins, C. J. Schmidt, and D. DeMille, Phys. Rev. Lett. **88**, 071805 (2002).
- [12] W. C. Griffith, M. D. Swallows, T. H. Loftus, M. V. Romalis, B. R. Heckel, and E. N. Fortson, Phys. Rev. Lett. **102**, 101601 (2009).
- [13] B. Klöter, C. Weber, D. Haubrich, D. Meschede, and H. Metcalf, Phys. Rev. A **77**, 033402 (2008).
- [14] B. K. Sahoo, R. Pandey, and B. P. Das, Phys. Rev. A **84**, 030502 (2011).

- [15] U. I. Safronova, M. S. Safronova, and M. G. Kozlov, *Phys. Rev. A* **76**, 022501 (2007).
- [16] J.-P. Uzan, *Rev. Mod. Phys.* **75**, 403 (2003).
- [17] V. A. Dzuba, V. V. Flambaum, M. G. Kozlov, and M. Marchenko, *Phys. Rev. A* **66**, 022501 (2002).
- [18] V. A. Dzuba and V. V. Flambaum, *Canadian Journal of Physics* **87**, 15 (2009).
- [19] J. Berengut and V. Flambaum, *Hyperfine Interactions* **196**, 269 (2010), ISSN 0304-3843.
- [20] J. C. Berengut, V. A. Dzuba, and V. V. Flambaum, *Phys. Rev. A* **84**, 054501 (2011).
- [21] M. G. Kozlov, S. G. Porsev, S. A. Levshakov, D. Reimers, and P. Molaro, *Phys. Rev. A* **77**, 032119 (2008).
- [22] V. V. Flambaum and S. G. Porsev, *Phys. Rev. A* **80**, 064502 (2009).
- [23] V. V. Flambaum and V. A. Dzuba, *Canadian Journal of Physics* **87**, 25 (2009).
- [24] W. M. Haynes, ed., *The Handbook of Chemistry and Physics* (CRC Press, Boca Raton, FL, 2012).
- [25] J. Mitroy, M. S. Safronova, and C. W. Clark, *J. Phys. B* **43**, 202001 (2010).
- [26] L. R. Hunter, D. Krause Jr., S. Murthy, and T. W. Sung, *Phys. Rev. A* **37**, 3283 (1988).
- [27] T. P. Guella, T. M. Miller, B. Bederson, J. A. D. Stockdale, and B. Jaduszliwer, *Phys. Rev. A* **29**, 2977 (1984).
- [28] T. R. Fowler and J. Yellin, *Phys. Rev. A* **1**, 1006 (1970).
- [29] M. S. Safronova, U. I. Safronova, and S. G. Porsev, *Phys. Rev. A* **87**, 032513 (2013).
- [30] G. Ranjit, N. A. Schine, A. T. Lorenzo, A. E. Schneider, and P. K. Majumder, *Phys. Rev. A* **87**, 032506 (2013).
- [31] B. K. Sahoo and B. P. Das, *Phys. Rev. A* **84**, 012501 (2011).
- [32] M. A. Z. Ewiss, C. Snoek, and D. Donszelmann, *Astron. Astrophys.* **121**, 327 (1983).
- [33] T. Andersen and G. Sørensen, *Phys. Rev. A* **5**, 2447 (1972).

- [34] W. Demtröder, *Laser Spectroscopy: Basic Concepts and Instrumentation* (Springer, New York, 1998), 2nd ed., ISBN 354057171X.
- [35] C. J. Foot, *Atomic Physics* (Oxford University Press, Oxford, 2005), ISBN 019850695.
- [36] P. A. Vetter, Ph.D. thesis, University of Washington (1995).
- [37] M. Abramowitz and I. A. Stegun, eds., *Handbook of Mathematical Functions with Formulas, Graphs, and Mathematical Tables* (U.S. Department of Commerce, NIST, 1972).
- [38] C. Chiarella and A. Reichel, *Math. Comp.* **22**, 137 (1968), ISSN 0025-5718.
- [39] J. M. Supplee, E. A. Shittaker, and W. Lenth, *Appl. Optics* **33**, 6294 (1994).
- [40] J. A. Silver, *Appl. Opt.* **31**, 707 (1992).
- [41] G. C. Bjorklund and M. D. Levenson, *Appl. Phys. B.* **32**, 145 (1983).
- [42] C. D. Holmes, Bachelor's thesis, Williams College (2003).
- [43] A. T. Lorenzo, Bachelor's thesis, Williams College (2011).
- [44] A. E. Schneider, Bachelor's thesis, Williams College (2012).
- [45] P. Hess, Bachelor's thesis, Williams College (2008).
- [46] A. Khadjavi, A. Lurio, and W. Happer, *Phys. Rev.* **167**, 128 (1968).
- [47] S. C. Doret, P. D. Friedberg, A. J. Speck, D. S. Richardson, and P. K. Majumder, *Phys. Rev. A* **66**, 052504 (2002).
- [48] M. S. Safronova and P. K. Majumder, *Phys. Rev. A* **87**, 042502 (2013).
- [49] M. Gunawardena, H. Cao, P. W. Hess, and P. K. Majumder, *Phys. Rev. A* **80**, 032519 (2009).
- [50] M. Gunawardena, P. W. Hess, J. Strait, and P. K. Majumder, *Rev. Sci. Instrum.* **79**, 103110 (2008).
- [51] G. R. Janik, C. B. Carlisle, and T. F. Gallagher, *J. Opt. Soc. Am. B* **3**, 1070 (1986).
- [52] Y. Ralchenko, A. E. Kramida, J. Reader, and N. A. S. D. Team, *NIST Atomic Spectra Database (ver. 5.0)* (2012).